INVESTIGATION ON THE SUPERPLASTIC HOT WORKING OF MG-LI ALLOYS FOR FABRICATION OF COMPLEX STRUCTURES

YANG HAOPENG

PhD

The Hong Kong Polytechnic University

2019

The Hong Kong Polytechnic University

Department of Mechanical Engineering

INVESTIGATION ON THE SUPERPLASTIC HOT WORKING OF MG-LI ALLOYS FOR FABRICATION OF COMPLEX STRUCTURES

YANG HAOPENG

A thesis submitted in partial fulfillment of

the requirements for the degree of

Doctor of Philosophy

December 2018

Certificate of originality

I hereby declare that this thesis is my own work and that, to the best of my knowledge and belief, it reproduces no material previously published or written, nor material that has been accepted for the award of any other degree or diploma, except where due acknowledgement has been made in the text.

YANG HAOPENG

Abstract

Mg-Li alloys, as a kind of superlight material, have the enormous promising potential for wide applications in various industries due to their superior stiffness-to-weight ratio, low density, good mechanical properties, and biodegradability, which are greatly favored by the aerospace and military fields, where reducing the product weight is critical and crucial, and the biomedical field, where biodegradability can be well applied. These fields usually require parts with complex shapes and geometries, which are generally formed with large deformation. However, due to existence of the hexagonal-close-packed (HCP) structure of Mg, which has only a few slip systems, the material is relatively hard to be deformed compared to the cubic-centered materials at room temperature.

In order to efficiently fabricate the complex structures by using Mg-Li alloys, the application of superplastic deformation (SPD) of the material can be utilized, by which the material can achieve an extraordinarily large amount of deformation under certain conditions. Researchers have already been attempting to investigate the superplasticity of Mg-Li alloys. However, most of the studies have focused on how to refine the material microstructure to achieve fine-grain superplasticity, while few of them have attempted to attain better superplasticity through optimizing the route of deformation, which could also be a possible way of enhancing the material superplasticity.

An ingenious SPD method, the maximum strain rate sensitivity (*m*) (Max*m*) SPD, was originally introduced for enhancing the superplasticity of Ti alloys. Since the *m* value acts as an indicator for the resistance to necking and a higher *m* value always corresponds to a better state of superplasticity and further the larger overall elongation, the best superplastic state of the material can be retained if the maximum *m* value can be maintained throughout the deformation process. For the conventional SPD methods like constant velocity (Const*v*) SPD and constant strain rate (CSR) SPD, *m* cannot always be kept at its maximum value, so the potential superplasticity of the material might be compromised. The idea of Max*m* SPD was thus proposed to maintain the largest *m* value throughout the SPD process by in situ measurement of the *m* value and dynamic control of the deformation strain rate. However, since the Max*m* SPD method is still relatively new and the deformation process is highly dependent on the capacity of experimental equipment, this innovative idea has only been successfully applied in the SPD of Ti alloys so far, but its potential applications to the SPD of other materials have not been fully explored and exploited.

Inspired by the enhanced superplasticity of Ti alloys by Max*m* SPD, this research is dedicated to exploring the applicability of Max*m* SPD to Mg-Li alloys. In this thesis, the alloy of Mg-9Li-1Al (in wt. %, LA91), which has the duplex phases with HCP and BCC structures, was utilized as the experimental material. By adopting both the traditional and Max*m* SPD, the differences between these methods were compared and discussed, and the characteristics of Max*m* SPD of Mg-Li alloys were identified.

At first, single-step Max*m* SPD of the LA91 alloy was studied. The as-received material and the samples further refined by equal channel angular extrusion (ECAE) were applied. It was found that the optimal SPD temperature of LA91 alloy is 573 K. The maximum elongation in the experiment was 563.7 %, obtained by Max*m* SPD at the temperature of 573 K by using the 8-pass ECAEed samples, and it was found that ECAEed samples are more favored by Max*m* SPD than as-extruded samples owing to the more equiaxed microstructure in the ECAEed samples. Nonetheless, since grain refinement procedures like ECAE are quite complicated and time-consuming, an innovative stepped SPD method was then applied to explore the potential superplasticity of the as-received material in the as-extruded state. Due to dynamic recrystallization, the grains of the as-received alloys can be transformed to be more equiaxed in the first deformation step, which is more favored by the SPD process. The largest elongation of 621.1 % was obtained by CSR-Max*m* SPD with the pre-elongation of 250 %, which is even larger than the result in the single-step Max*m* SPD experiments by using the grain-refined material. The result showed that the stepped SPD method can largely enhance the superplasticity of the material.

Moderate annealing was finally applied to the as-received material and the two-step SPD method was adopted by using the annealed samples. The annealing treatment aimed at producing a more equiaxed grain structure by static recrystallization without severe grain coarsening. However, after the SPD experiments, it was found that the annealed samples exhibited worse superplasticity than the as-received materials. It

was indicated that during the annealing process, static recrystallization occurred and expended the strain energy obtained from extrusion, which provides the energy source for dynamic recrystallization during SPD. The material superplasticity was therefore compromised, and the application of annealing for the sake of obtaining a more equiaxed grain structure could not be feasible for further enhancing the material superplasticity.

This thesis explores the potential superplasticity of Mg-Li alloys by adopting both single-step and two-step SPD processes, and provides an in-depth and epistemological understanding of Max*m* superplasticity of the material. It can be found from this research that Max*m* SPD can be well utilized for the hot working of Mg-Li alloys to enhance the material superplasticity. However, how to realize the Max*m* SPD of Mg-Li alloys in industrial mass production still needs to be further considered and explored in the future research.

Publications during the PhD study period

[1] **H.P. Yang**, M.W. Fu, S. To, G.C. Wang, Investigation on the maximum strain rate sensitivity (*m*) superplastic deformation of Mg-Li based alloy, Materials & Design 112 (2016) 151-159.

[2] **H.P. Yang**, X. Zhang, P. Chen, M.W. Fu, G.C. Wang, and S. To, Investigation on the improved maximum strain rate sensitivity (*m*) superplasticity of Mg-9Li-1Al alloy by a two-step method, to be submitted to an SCI Journal.

[3] M.W. Fu, **H.P. Yang**, P. Chen, X. Zhang, G.C. Wang, Study on the enhanced superplasticity of Mg-Li based alloy by a stepped deformation method, Defect and Diffusion Forum, Trans Tech Publ, 2018, pp. 103-108.

[4] J.Y. Zheng, **H.P. Yang**, M.W. Fu, C. Ng, Study on size effect affected progressive microforming of conical flanged parts directly using sheet metals, Journal of Materials Processing Technology 272 (2019) 72-86.

Acknowledgements

Firstly, I would like to express my special appreciation to my chief supervisor Prof. Mingwang Fu for his invaluable guidance, continuous support, extraordinary patience, and kindness during my PhD study. As an expert in materials forming field, Prof. Fu's deep insight into the relevant knowledge and the good understanding of the research have profoundly enlightened me. It is extraordinarily honorable and lucky for me to have Prof. Fu as the supervisor and mentor for my PhD study.

I also would like to express my sincere gratitude to Prof. Sandy To and the State Key Laboratory of Ultra-precision Machining Technology in the Department of Industrial and Systems Engineering in The Hong Kong Polytechnic University for the funding support during my first two years of PhD study and the deep knowledge of advanced manufacturing technology I learnt from the courses offered by the department.

Meanwhile, I would like to especially thank Prof. Gaochao Wang and his students of Mr. Ling Ding, Mr. Peng Chen and Mr. Xiang Zhang in the Nanchang Hangkong University. Since many of my SPD experiments were conducted in The Nanchang Hangkong University and assisted by Prof. Wang and his students, their guidance and help are absolutely indispensable for me. I could not have accomplished my research without their support and help.

Furthermore, I would like to thank my former and present team members for their assistance and companion during my PhD study. Meanwhile, I also want to thank the administrative and technical staff in the Department of Mechanical Engineering for their zealous and generous help.

Last but not least, this thesis is dedicated to my family including my father, mother, grandfather, grandmother, uncle, and aunt for their love, support, patience and encouragement throughout my life.

Table of contents

List of figures and tables

List of abbreviations and acronyms

Abbreviations	Explanations
BCC	Body-centered-cubic
Const*v*	Constant velocity
CSR	Constant strain rate
DNA	Deoxyribonucleic acid
DRX	Dynamic recrystallization
EBSD	Electron backscatter diffraction
ECAE	Equal channel angular extrusion
FSP	Friction stir processing
FSS	Fine-structure superplasticity
GBS	Grain boundary sliding
HCP	Hexagonal-close-packed
ICP	Inductively coupled plasma optical emission spectrometer
ISS	Internal stress superplasticity
LA91	Mg-9Li-1Al
Max*m*	Maximum strain rate sensitivity
OM	Optical microscopy
RNA	Ribonucleic acid
SEM	Scanning electron microscope
SPD	Superplastic deformation

SRX	Static recrystallization
UTS	Ultimate tensile stress

Chapter 1 Introduction

1.1 Research background

Nowadays, with the growing trend of energy saving and environmentally friendly product design and development, the demand for lightweight materials has increased drastically for making products with light weight but perhaps more complex shapes. Apart from the composite materials which have been a popular research topic for many years, selection of lightweight metallic alloys is also a good choice owing to the low density as well as good mechanical properties. With the addition of the lightest metal of Li into the Mg matrix, Mg-Li alloys become the lightest alloy which has superior stiffness-to-weight ratio, good mechanical and machining properties, superior magnetic screen and shock resistance ability, and biodegradability. These properties are greatly favored by aerospace, military and biomedical fields [1-7].

Because of the hexagonal-close-packed (HCP) structure in Mg, Mg alloys are usually more difficult to be deformed than the cubic-latticed metals such as Cu and Al, owing to the fewer slip systems in the HCP structure. The Mg alloys are therefore typically used in its as-cast state in the industries if a relatively complicated shape is needed, but the as-cast Mg alloys might not possess the high mechanical properties as the wrought alloys. As a result, other techniques of fabricating the Mg alloys products

have been investigated and developed, among which superplastic deformation (SPD) could be an ideal choice for the nearly no-necking deformation with the extreme amount of elongation and low deformation force. Superplasticity is the capability of polycrystalline materials to demonstrate the high elongation to failure of usually more than 400 % in tensile tests [8]. Most research of the SPD of Mg-Li alloys have been focused on how to achieve high superplasticity via refining the grain structure [9-12], but few have discussed how to enhance the superplasticity by optimizing the route of deformation. If a better deformation method can be developed such that the complex and time-consuming material preparation step for inducing grain refinement can be simplified or even eliminated, the SPD process can become more efficient, which makes it easier for the wide application of SPD in industries to form complex shapes with less effort.

Inspired by the maximum strain rate sensitivity (m) (Max$m$) SPD proposed by Wang et al. [13], this research aims at applying the deformation method of Max$m$ SPD to Mg-Li based alloys. During the SPD process, the m value is a critical parameter to indicate the superplastic state, and a larger m value is usually related to a better superplastic state and further the larger final elongation. Traditional SPD methods include constant velocity (Const$v$) SPD, where the deformation velocity is constant, and constant strain rate (CSR) SPD, where the strain rate of deformation is constant. However, in the traditional SPD methods, the m cannot always be maintained at its largest value, while in Max$m$ SPD, by simultaneous and in situ measurement of the m

value and dynamic control of the deformation strain rate, the maximum *m* value can always be maintained throughout the deformation process. Therefore, this method is suitable for enhancing the efficiency of SPD and obtaining the largest elongation theoretically. In recent years, a series of studies of Max*m* SPD by using Ti alloys have been conducted, and Max*m* SPD can substantially enhance the deformation capacity of several Ti alloys [13-17].

The method of Max*m* SPD was initially designed and proposed for fabrication of the parts used in aeronautics and astronautics fields made by Ti alloy. Due to the complex structure of the parts, a large amount of deformation is usually needed. However, a large deformation of Ti alloys usually requires a high force level, which is sometimes difficult or impossible to achieve. The Max*m* SPD process was thus invented to achieve large deformation while using a small force level, which has been proven to be successful for Ti alloys. However, this SPD process has been found inapplicable for other traditional superplastic alloys like Al and Cu. Considering the similar microstructure of the duplex-phase Mg-Li alloy used in this study and Ti alloys used in the prior arts, it may also be potentially applied in inducing the superplasticity of the duplex-structured Mg-Li alloys.

In this study, Max*m* SPD of the grain-refined Mg-Li alloy was studied at the beginning. An innovative stepped SPD method incorporating Max*m* SPD was then investigated by using the as-received material without further grain refinement. It has been found

that the method of Max*m* SPD can be successfully utilized for the deformation of Mg-Li alloys for enhancing its deformation capacity. Meanwhile, the stepped SPD method can improve the material superplasticity by providing a more equiaxed microstructure for Max*m* SPD in the second deformation step, by which the commonly used material preparation step for grain refinement can be eliminated and the efficiency of the whole production process can be improved.

1.2 Objectives and scope of this research

The Max*m* SPD, in which the best state of superplasticity can be maintained by cyclically adjusting the strain rate according to the variation of the simultaneously measured *m* value, has been successfully applied to the SPD of Ti alloys and largely improved the material formability than the conventional SPD methods. Due to the similar duplex-phase structure of Mg-Li and Ti alloys, Max*m* SPD can also be potentially applied in the deformation of Mg-Li alloys. This research is thus mainly focused on the investigation of superplasticity of the selected Mg-Li alloy by adopting the conventional and Max*m* SPD processes. Through investigating deformation behavior, microstructure evolution and fracture mechanisms, the difference between Max*m* and conventional SPD methods can be identified, which is beneficial to further research and wide application of the Max*m* SPD process.

Since Max*m* SPD is relatively new and requires unique and specialized experimental equipment, there is no other exploration of this SPD method in addition to Wang's group who proposed and implemented Max*m* SPD, and only Ti alloys have been studied before this research. The setting of process parameters for both traditional and Max*m* SPD of Mg-Li alloys such as deformation temperature and initial velocity need to be confirmed at the beginning of the research. This was realized by the preliminary experiments in each chapter, including the search for the optimal temperature in Chapter 3 and the confirmation of the optimum velocity or strain rate in Const*v* or CSR SPD in Chapter 4 and 5. In this way, the SPD experiments can be simplified and more efficient.

After conducting the SPD experiments by using the optimal parameters, tensile test data were collected during the deformation process and the fractured specimens were collected. The tensile test data represent the deformation behavior of material throughout the SPD process, and the *m* value can be calculated, which indicates the superplastic state during the deformation process. Meanwhile, stress-strain and *m* value variation curves are analyzed to explore the deformation behavior.

Microstructure of materials is closely associated with mechanical properties and deformation behavior of the material, so analysis of material microstructure before, during, and after SPD experiments is required. The microstructure of materials before SPD can be obtained from the undeformed specimens, and the microstructure after the

deformation can be obtained from the fractured region of the deformed specimens after SPD. Meanwhile, the material microstructure during the deformation can be acquired from the deformed samples which is collected from the interrupted SPD process when a certain amount of pre-elongation is reached. Through analyzing microstructure evolution of the material, the deformation and fracture mechanisms can also be explored.

By combining the analysis of microstructure evolution and deformation behavior, the deformation process can be fully explored and exploited. In this way, the differences between the single-step and two-step SPD can also be investigated. Therefore, the objectives and scope of this research can be summarized as follows.

(a) Apply the Max*m* SPD method to Mg-Li alloys for enhancing the material superplasticity.

(b) Search for and confirm the optimal process parameters in different SPD methods.

(c) Analyze the deformation behavior during the deformation process by using different SPD methods.

(d) Investigate the microstructure evolution in the SPD process by using different SPD methods.

(e) Establish the relationship between microstructure evolution and deformation behavior for an in-depth understanding of the SPD process.

(f) Study the fracture mechanisms of the SPD process and the method for preventing

premature fracture.

1.3 Organization of this thesis

This thesis is composed of 6 chapters and 1 reference list. It can be mainly divided into 3 parts. The first part includes a general introduction and a literature review, which are Chapters 1 and 2. The second part is Chapter 3, which covers the application of Max*m* SPD to the Mg-Li alloy with the grain structure refined by equal channel angular extrusion (ECAE). The third part consists of Chapters 4 and 5, where the enhanced Max*m* SPD by a stepped SPD method applied to deformation of the Mg-Li alloy is described.

Details of each chapter are shown as follows.

Chapter 1 provides a brief introduction of this thesis, including research background, objectives and organization of this research.

Chapter 2 gives a brief literature review of Mg-Li alloys, issues in material superplasticity, recent research progress of the SPD of Mg-Li alloys, and theory of Max*m* SPD.

Chapter 3 describes the application of single-step Max*m* SPD to deformation of the Mg-Li alloy. ECAE was introduced to refine the microstructure and the distinction between the as-received and ECAEed material in microstructure evolution and

deformation behavior in SPD processes are discussed.

Chapter 4 presents the two-step deformation method for the SPD of Mg-Li alloys by using conventional SPD as the first step and Max*m* SPD as the second step, and a discussion of the influence of different parameters and process routes on the SPD of Mg-Li alloys is provided.

Chapter 5 articulates the employment of the annealed alloys in the same stepped SPD method presented in Chapter 4. The intention of this chapter is to explore the effect of annealing on the material superplasticity. The influence of different process routes and parameters on the SPD of the annealed material is also discussed.

Chapter 6 gives the conclusion of this research and summarizes the present outcome. Meanwhile, the future work to be accomplished after this study is delineated.

Chapter 2 Literature Review

2.1 Material selection for Mg-Li alloys

Coronary artery diseases, including atherosclerosis, have become more and more common all over the world. These diseases are harmful to the continuity of human blood flow and are the leading cause of death in US [18, 19]. Drug administration, coronary artery bypass grafting and stenting are the common treatment methods of the diseases, among which the method of stenting is currently widely used for treatment of patients with less complicated coronary artery diseases. The stenting method is commonly used in combination with the balloon angioplasty to expand the stenosed area and maintain blood flow [18].

Vascular stents can be manufactured from a variety of materials. Traditionally, the stents are made of corrosion-resistant or inert materials such that the stents can permanently exist in the treated vessels even after recovery. The material used in this category of stents includes stainless steel, tantalum (annealed), Cp-Ti alloys nitinol and cobalt-chromium alloy [20-22]. However, the permanent existence of the stents in blood vessels may cause clinical problems such as in-stent restenosis and thrombosis [4, 5]. A secondary surgery to remove the stent might be necessary, which could cause health risks and economic burden of the patients. Drug-eluting stents, which can continuously provide medicine inside the vessel after the surgery for a certain period

to alleviate the symptoms, are therefore recently introduced, but it still cannot remove the long-term risks of the abovementioned symptoms. For the sake of eliminating the risks of secondary surgery, the biodegradable stents may be an ideal choice to tackle the problems, which can temporarily open the stenosed vessel until vessel remodeling and then be gradually absorbed, consumed or excreted in human body, and a secondary surgery to remove the implants may not be needed after healing. Therefore, the biodegradable stents can be expected as a less-invasive choice for stenting [23].

There are basically two categories of materials that can achieve the biodegrading function: biodegradable polymers and biodegradable metal. The biodegradable polymers are mainly made from lactic acid, glycolic and caprolactone families. However, mechanical strength of the polymers may be unsatisfactory, which is unsuitable for a stent which stays in the vessel and deforms with the vessel. For a vessel stent, several requirements should be met, as shown in the following points [24].

(a) Biodegradability: the device should have a working duration of 3-6 months and the full-degradation time of 12-24 months.

(b) Biocompability: the stent should have no toxicity, no inflammatory response, and no release of harmful materials.

(c) Tensile yield strength > 200 MPa.

(d) Ultimate tensile strength > 300 MPa.

(e) Elongation > 15-18 %.

For the requirements of mechanical properties, the polymer candidates for biodegradable stent material might fail to achieve. Therefore, biodegradable metal could be a suitable choice. Among the metallic materials, Fe and Mg can be considered as appropriate candidates, and they can both be corroded in human body and cause no harmful effects [25]. Fe is a necessary element for human body, especially for the formation of red blood cells. Pure Fe has been applied as a stent material in rabbit aortas and the stents were held for 18 months, during which damage has been reported to vessel media and internal elastic membrane [26]. However, the corrosion of Fe is too slow for the application of a biodegradable stent. Mg is also essential in human body due to its importance in human metabolism, and Mg^{2+} is the fourth most abundant cation in human body. Meanwhile, Mg is a co-factor for many important enzymes, and it can stabilize deoxyribonucleic acid (DNA) and ribonucleic acid (RNA) structures [27]. Mg is a superiorly lightweight material with a density of 1.74 g/cm^3, which is much less dense than Al and steel [28, 29]. Moreover, daily intake of Mg for a normal adult is 300-400 mg, and redundant Mg^{2+} cations can be harmlessly and efficiently excreted in the urine [28]. However, the corrosion rate of Mg is too rapid in chloride-containing solutions, which is the same environment as human body fluid or blood plasma [30].

The fast corrosion of Mg may lead to generation of hydrogen and alkalization of the solution [28]. In human body, hydrogen is accumulated in the form of gas pockets near the plant, which delays the healing of surgery region and could lead to necrosis of

tissues, because separation of tissues and tissue layers may be caused by the gas pockets [31]. When the bubbles are generated in a large amount, they will block the bloodstream and cause possible death of the patient. In addition, local alkalization may affect the pH-dependent physiological reactions near the stent unfavorably, which might cause a poisoning effect caused by alkalization when the local in vivo pH value becomes larger than 7.8. It is therefore necessary to control the degradation rate such that human body can gradually adjust the hydrogen and alkalization level. The tolerated hydrogen evolution rate is suggested as 0.01 ml/cm^2/day, and it is therefore necessary to contain the rate of hydrogen generation under this level [32].

There are several suggested ways to reduce the biodegradation rate of Mg alloy: (1) purification, (2) alloying and (3) surface coating [32]. Surface coating by corrosion resistant material can reduce the rate of corrosion by temporarily separating the material and the surroundings, while purification can reduce the level of impurities and reduce the corrosion rate. However, stripping of the surface coating could be a potential risk, and the corrosion rate of pure Mg is still relatively high. Nevertheless, for the alloying method, it can significantly change the corrosion resistance inherently, and the alloying content is therefore widely used for containing the rate of degradation of Mg alloys. In addition, it is necessary to increase the deformability of Mg alloys for wide application of the biodegradable stents, because it has the highly HCP structure, which has only a few slip systems and compromises the material formability.

For the alloying method, there are several choices for Mg to alloy with. Al is a common alloying element with Mg, and it can reduce the hydrogen evolution rate because Al can generate an aluminum oxide layer on the reaction layer [33]. Nevertheless, Al can easily combine with inorganic phosphates, which may cause shortage of phosphate in human body and induce dementia [34], so the large amount of Al used in human body is harmful to human health. For other choices of alloying elements, alkaline elements such as K, Na, Ca can be tolerated in human body, but their influence on reducing the corrosion of Mg element is not significant [32]. If alloyed with heavy metals, the Mg alloys may have an accelerated corrosion rate in turn. Moreover, heavy metals are detrimental to human health, so heavy metals are not suitable for making biomedical stents.

If Li is selected as the alloying element, the formability of Mg alloys at room temperature can be substantially increased. As shown in the phase diagram of Mg-Li alloy in **Fig. 2.1**, the addition of Li improves the ductility of Mg by gradually transforming the original HCP structure into the body-centered-cubic (BCC) structure and reducing the axial ratio of the HCP lattice in Mg [35]. As the content of Li is below 5.7 wt %, the alloy is the α phase solid solution of Li in Mg, which has an HCP structure. While the content of Li increases from 5.7 to 10.3 wt %, the alloy becomes a duplex structure containing both α and β phase, and the β phase is the solid solution of Mg in Li with a BCC structure. When the Li concentration is more than 10.3 wt %, the material is totally in the β phase and has a BCC structure [36]. Therefore, the

ductility of Mg alloy is effectively improved as Li content increases, but the mechanical strength might be compromised with the added Li element. Meanwhile, it was found that the addition of Al and rare earth elements can improve the tensile strength by solid solution strengthening, grain refinement, as well as dispersion. The composition of Mg-Li-Al-(RE) alloy was found to be a suitable choice for biodegradable stent applications because it possesses an acceptable corrosion rate and mechanical strength [33, 37]. Through short-term evaluation for determining the Li effect on primary cells and cell lines, it was found that Li does not negatively influence the cell viability [38]. However, the rare earth elements may be toxic to human health [39, 40]. Therefore, the alloy composition of Mg-Li-Al can be suitable for the biodegradable stent application with nearly no harmful effect. After comparison, considering the minimization of toxic elements and optimization of mechanical property and corrosion resistance, the alloy composition of Mg-9Li-1Al (in wt %, LA91) was selected as the material for biomedical applications, and this thesis is focused on how to efficiently enhance the formability of the biodegradable LA91 alloy.

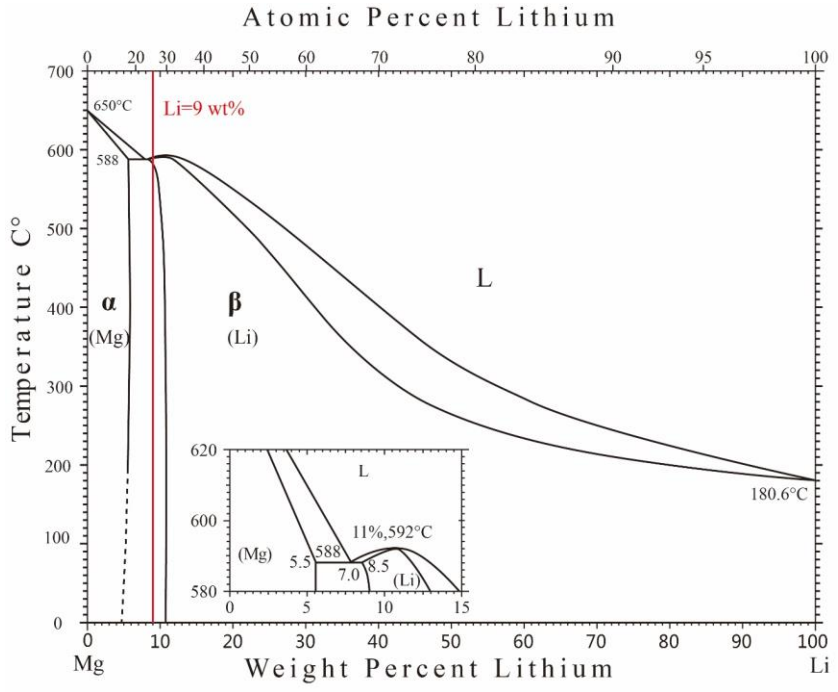

Fig. 2.1 Phase diagram of Mg-Li alloys [41].

2.2 Superplasticity of Mg-Li alloys

2.2.1 General introduction to material superplasticity

Superplasticity of materials is the capability of certain polycrystalline materials to demonstrate an extensively large amount of plastic elongation during tensile tests, where the phenomenon of necking does not occur before failure. Meanwhile, the superior formability can also be observed in the superplastic materials in torsion, compression and indentation hardness testing [42]. The tensile elongation induced by superplasticity is usually larger than 400 % and can even be as large as several thousand percent of the original length [8, 43], e.g. a Cu-10wt%Al based alloy can exhibit the largest final tensile elongation of 5500 % [44], and some Pb-Sn based

alloys can even demonstrate the deformation amount of 7550 % [45].

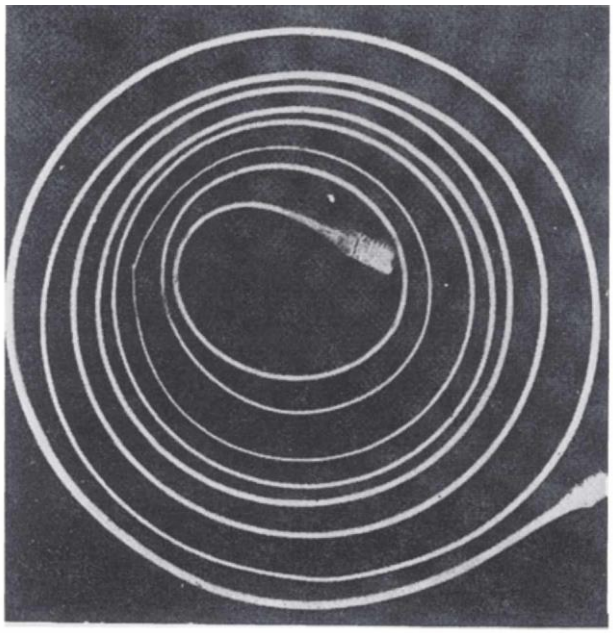

Fig. 2.2 Pearson's famous photo of a Bi-Sn alloy with 1950 % elongation in the year of 1934 [46].

Generally, the following requirements are necessary for achieving SPD: (1) fine grain structure with small grain sizes in the material (usually smaller than 10 μm); (2) deformation temperature near or over 0.5 T_m (T_m is the melting temperature) [47, 48]; and (3) the strain rate usually between 1×10^{-5} and 1×10^{0} /s [49-51]. The research of superplasticity is important in manufacturing industries owing to the capacity of inducing an extensive amount of deformation and the low force to maintain the steady state material flow. In such a case, a complicated product shape which is difficult or impossible to be manufactured by the traditional fabrication methods could be achieved by inducing the superplasticity of the material with less effort.

2.2.2 Two main types of superplasticity

Generally, there are two kinds of superplasticity, with the first one known as fine-structure superplasticity (FSS) and the second one known as internal stress superplasticity (ISS) [52]. The phenomenon of FSS is widely studied by researchers, and usually occurs with the prerequisite of the existence of micrograin structure, while ISS is relevant to the development of internal stress in certain types of materials before the SPD process [53].

The FSS materials can exhibit a high *m* value during the SPD process and typically *m* is larger than 0.33 [53]. It has also been reported that the highest elongation occurs when *m* is around 0.5 [54]. In FSS deformation, the fine grain structure is one of the major requirements. The average size of grains in the material should be typically in the order of 1 to 5 μm [52]. Although the microscopic deformation mechanisms of FSS is still not thoroughly established and understood, it is widely recognized that grain boundary sliding (GBS) is involved [55-57]. The process of GBS is usually modeled with the assumption that sliding usually occurs with the movement of extrinsic dislocations on grain boundaries, which can be used to explain the observation that the variable sliding amount of dislocations along the grain boundaries [58]. When the grain size in the material is decreased, the slidable grains and area of grain boundaries on a unit area is increased, which facilitates the GBS mechanism and can enhance the superplasticity. In addition, for the sake of avoiding extensive cavity

nucleation, which provides the source of fracture during SPD, GBS also requires the aid of accommodation mechanisms, which may include grain boundary migration, recrystallization, diffusional flow or slip [59]. The accommodation mechanisms, which are considered to be sensitive to the strain rate, are utilized to ensure the rearrangement of grains during GBS to realize strain compatibility and relieve the stress concentration caused by GBS [53]. Another important characteristic of FSS is that due to the fine grain structure in the material, the flow stress also decreases with the size of grains [52], which is because of the enhanced GBS mechanism caused by the fine grain size. In addition, the lower applied force can make the forming process much easier and reduce the manufacturing costs in the industries.

For the materials which can exhibit FSS, the presence of a second phase is usually required [52]. It is very rare that single phase materials can exhibit superplasticity, because the grain coarsening effect is usually too fast at the high temperatures where GBS can occur. To keep the small grain size in the material during SPD, the existence of a second phase is therefore usually needed. The growth of grains is often better inhibited with the increase of the portion of second phase. Meanwhile, it has been reported that many Al and Cu based alloys with fine grain sizes are very susceptible to cavitation when the matrix phase is soft and the second phase is relatively hard, while no cavitation is found for the Ti-4Al-4V with fine grain sizes and hypereutectoid Fe-Fe_3C alloys before fracture. Therefore, the strength difference between the second phase and the matrix should not be too large. Nonetheless, if the matrix phase is much

softer than the second phase, the second phase needs to be in the form of fine particles distributed in the matrix uniformly such that the material superplasticity can be guaranteed.

The grains of the FSS materials need to be equiaxed such that grain boundaries can experience shear stress and GBS can be induced. If the material consists of elongated cylindrical grains, the tensile tests in the longitudinal direction of the elongated grains can lead to superplastic behavior, while the material will not exhibit a very large elongation if tested in the transverse direction of the grains. This is because the occurrence of GBS along the longitudinal direction of the grains is easier than that in the transverse direction if elongated grains exist in the microstructure [52]. Meanwhile, high-angle grain boundaries are favored by superplastic flow, because the low-angle grain boundaries, which is often obtained in warm working, cannot easily slide with the shearing stresses. The materials with low-angle boundaries are usually not superplastic, but it can achieve superplasticity when the low-angle boundaries are transformed into high-angle ones through proper thermal or thermomechanical treatments [60, 61]. In the superplastic materials, another requirement of the grain boundaries is that the boundaries should be mobile. During the GBS process, the phenomenon of stress concentration and other obstructions can be induced at triple junction points where the grain boundaries congregates. The mobility and the capability of migration of the grain boundaries during GBS can facilitate the reduction of the stress concentrations, which maintains the continuation of the GBS process. For

the fine-grained ceramic polycrystals deformed at high temperatures, however, the limited ductility and absence of superplasticity could be attributed to the immobile grain boundaries even though the *m* value is high, which is because the incapability of grain migration may cause high stress concentration at the triple junction points on the grain boundaries during GBS and lead to nucleation of cracks and early fracture [52].

Except for the FSS type of superplasticity, another major kind of superplasticity is the ISS. During the ISS deformation, the internal stress inside the material can be developed and the strain rate sensitivity exponent *m* can approach 1, which means that the flow is an ideal Newtonian-viscous behavior. These materials are believed to be deformed by a slip mechanism [52]. Many ways can be used to induce the internal stress in ISS, which include thermal cycling of composite materials in which different thermal expansion coefficients are possessed by the different constituents [62, 63], thermal cycling of single-phase alloys and polycrystalline pure metals which possess anisotropic thermal expansion coefficients [64], and thermal cycling by the phase change during the deformation process [65-68]. As a matter of fact, the pressure-induced phase changes have been recognized as one of the sources of superplastic flow in geological materials. For instance, in the earth's upper mantle, the orthorhombic olivine is gradually transformed into spinel phase at a depth of about 400 km below the surface of the earth due to pressure. It is recognized that the ISS due to transformation stresses by cycling of pressure can induce low effective viscosity in a mixed phase region [52, 69].

2.2.3 Other types of superplasticity

Apart from the FSS and ISS, there are some other types of superplasticity which could have different deformation mechanisms from FSS and ISS, including the superplasticity in the coarse-grained materials and the high strain rate superplasticity. These two types of superplasticity may not need the requirements of fine grain sizes or low strain rates, which are the common requirements in typical superplasticity of FSS and ISS [49-51], and therefore may improve the efficiency in manufacturing.

The coarse-grained superplasticity usually occur in Class I solid solutions, which are a type of dilute alloys in which the glide segment of the glide/climb dislocations creep is a rate-controlled process, owing to the impeded dislocation motion by the solute atoms [70-72]. This type of material can develop true Newtonian flow and induce FSS, but with coarse-grained structure, class I alloys can also induce superplasticity, because the glide-controlled creep mechanism may lead to high strain rate sensitivity and exhibit quasi-superplastic elongation of over 200 % [73-75]. The superplasticity in coarse-grained alloys indicates that the complex preparation step for grain refinement such as thermomechanical process may not be necessary for the Class I solid solutions due to the intrinsic high strain rate sensitivity.

The high strain rate superplasticity is delineated as the occurrence of superplastic flow as the deformation strain rate is equal to or greater than 10^{-2} /s [54, 76]. The strain rates

in commercial applications are usually between 10^{-2} and 10^{-1} /s, so the realization of high strain rate superplasticity is therefore beneficial to the wide application of SPD in commercial use [53]. The high strain rate superplasticity could be realized by enhancing the GBS mechanisms through the reduction of grain sizes or by engineering the nature of the interfaces to facilitate the sliding on the interface [76]. It has been proposed that both GBS and interfacial sliding could be the deformation mechanisms of high strain rate superplasticity. Meanwhile, an accommodation mechanism should also work during the deformation process to avoid cavitation at the high strain rates, but the nature of the accommodation mechanism to enable the mobility of boundaries and interfaces is still unknown [53]. The high strain rate superplasticity has been found in metal-matrix composites, mechanically alloyed materials, conventional alloys which experience continuous dynamic recrystallization (DRX), and alloys processed by power consolidation, physical vapor deposition, and intense plastic straining methods including ECAE, high-pressure torsion and friction stir processing (FSP) [53, 77-79]. There are several features of the material demonstrating high strain rate superplasticity, which could be distinct from the typical SPD processes and are listed as follows [80].

(1) The deformation temperature of the high strain rate superplasticity are usually very high, some may be even a little higher than the incipient melting point for the metal-matrix composites.

(2) The strain rate sensitivity exponent value is usually from 0.1 to 0.3, and the lower *m* value is achieved when the strain rate is low.

(3) High apparent activation energy value for superplasticity is usually required, and the activation energy value at lower strain rates are usually higher than that at higher strain rates.

2.2.4 Recrystallization during SPD

As has been discussed in the previous text, the recrystallization is a critical accommodation mechanism during SPD, because the recrystallized small grains increase the slidable grains and grain boundaries and facilitate GBS, which helps to accommodate the metal and reduce the deformation stress. Energy is stored mainly in the form of dislocations during the deformation process, which needs to be released by the accommodation mechanisms of recovery, recrystallization, and grain growth. Recovery includes all the mechanisms which releases the stored energy while the movement of high angle grain boundaries is not necessary. Typical recovery processes are involved with the rearrangement of dislocations for the sake of lowering the energy, which includes the formation of low angle grain boundaries and annihilation of dislocation line length in the subgrain interior [53]. Recrystallization is defined as the formation and migration of the high angle boundaries driven by the stored energy in the material [81]. Meanwhile, the grain growth process is the process of the growth of average grain size, which is driven by the decrease in the grain boundaries and always occurs after the recrystallization process [53].

Recrystallization can be typically classified into two types: static and dynamic recrystallization. By definition, the static recrystallization (SRX) is the one occurs when the material is not deformed and there is no induced plasticity. The most common example of SRX is the mechanism during the heat treatment of cold-worked metal materials. For the DRX process, it usually occurs with the concomitant plasticity and during a deformation process [81]. The DRX is a critical mechanism during the deformation at high temperatures and is usually related to the softening of materials. As shown in **Fig. 2.3**, at first, the hardening effect is dominant, and the material is softened after the peak stress is reached. The softening effect is greatly related to the nucleation of the growth of new recrystallized grains which can annihilate dislocations with the emergence of the new grains. In the meantime, DRX can occur before the occurrence of the peak stress, which can be proved by the decreasing hardening rate θ with the function of flow stress, which is accelerated by the DRX softening effect [53, 82]. Sometimes the single peak in stress in the stress-strain curve cannot be found, which is substituted by the multi-peaks of stress followed by the steady state region, as shown in **Fig. 2.3**. It has been suggested that the cyclic behavior is induced by the combined effect caused by coarsening and refinement of grains [83].

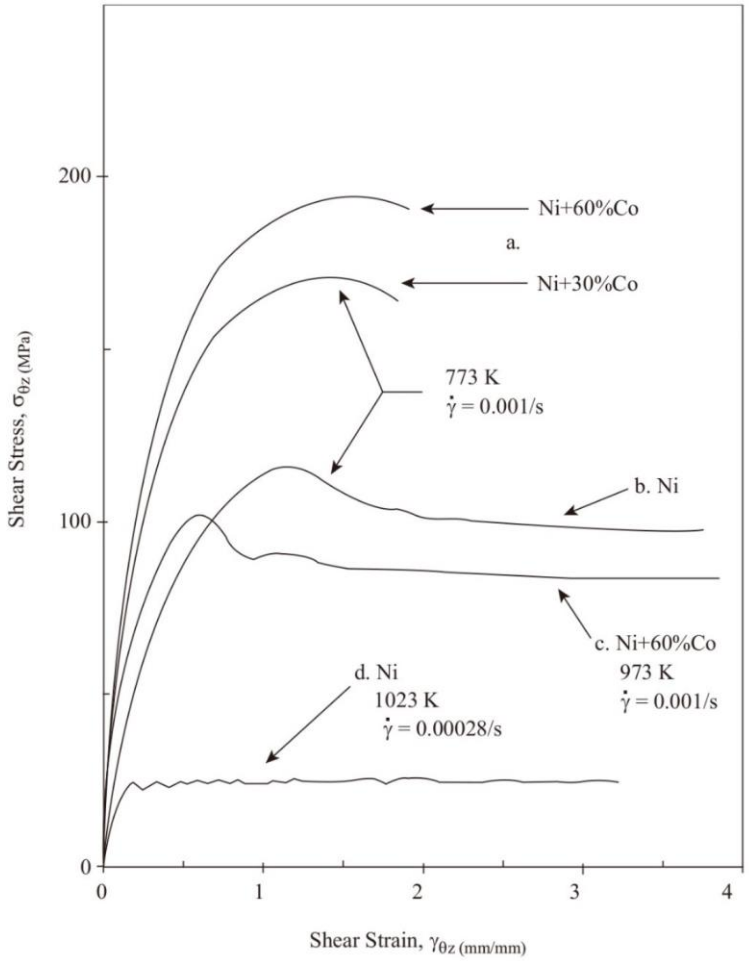

Fig. 2.3 Dynamic recrystallization in Ni and Ni-Co alloys in torsion [82].

2.2.5 Superplasticity of Mg-Li alloys

The Mg alloys are very important in engineering fields due to the low density and high specific strength and stiffness. Mass production of Mg alloys is largely demanded in the applications in small electronic devices, lightweight automotive components and other fields where the need of reducing the weight of products is critical [84]. However, the main method of production of the Mg alloys is die casting, and over 90 % of the Mg alloys are fabricated by the casting process [85]. Although the casting procedure

may be a cost-effective method and the requirements of the current applications can be satisfied, the low mechanical strength of the as-cast materials and the inevitable casting defects may compromise the wide application of Mg alloys. The application of forging processes can lead to better mechanical properties of the deformed alloys, but because of the inherent limitations of Mg alloys caused by the HCP structure, the production of wrought Mg alloys is more difficult than other alloys.

Unlike other materials like Cu and Al, Mg alloys inherently exhibit lower formability at room temperatures. The limitations in formability is induced by the small number of slip systems of the alloys during deformation. According to the von-Mises yield criterion, at least 5 independent slip systems should be active such that the uniform deformation can occur [86]. For the HCP lattice in Mg, it contains 3 types of slip systems: basal, prismatic, and pyramidal, as illustrated in **Fig. 2.4**. However, only the basal slip system can be activated at room temperatures in the HCP structure in Mg. The critical resolved shear stress for the basal slip is about 100 times less than the other slip systems with prismatic and pyramidal planes in Mg. Therefore, basal slip is the primary mechanism when the movement of dislocations is the dominant deformation mechanism [84]. Furthermore, the two independent basal slip systems cannot meet the uniform yielding criterion. Other deformation mechanisms like non-basal dislocation slip, GBS as well as dislocation twinning can also be related to the deformation, which depends on the characteristics of the material microstructure [87]. In the materials with fine grain structure, the GBS mechanism and the c-axis

deformation may be activated. In coarser grained materials, the non-basal slip is only confined to the grain boundaries nearby, and the twinning may occur to compensate for the preferential slip on the basal plane [88]. When the Mg alloys are tested at high temperatures, the DRX can also occur and facilitate the GBS mechanism during deformation [89].

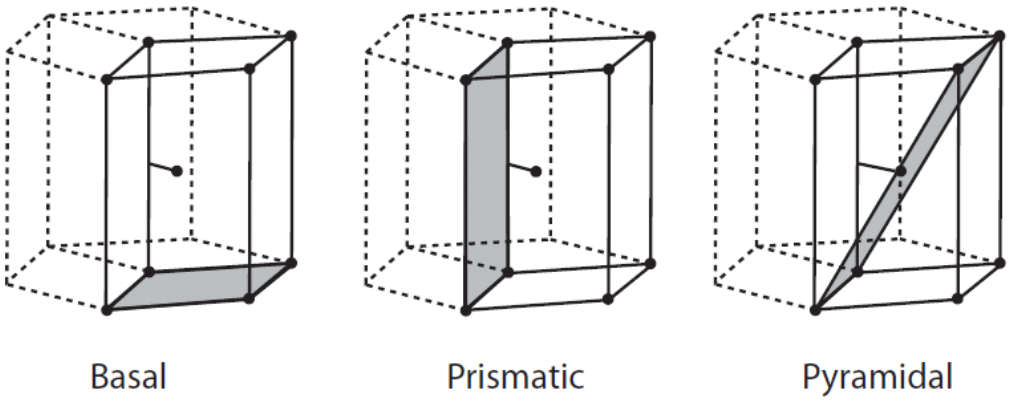

Fig. 2.4 3 types of slip systems in the HCP structure [84].

For the Mg alloys, the deformation method utilizing the superplasticity of the material is a feasible way to induce large amount of deformation with less effort. It has been discovered that for the Mg-Li alloys, which is selected as the target material in this research, can exhibit superplasticity at high temperatures, which has drawn much attention from researchers to investigate the SPD of Mg-Li alloys. If the superplasticity of the alloys can be realized in the industry, the potential wide applications of Mg-Li alloys might be achieved. In this section, recent investigations on the superplasticity of Mg-Li alloys are reviewed. There are several ways of enhancing the superplasticity

of materials, including the FSS and ISS described in the former text, but the main research focus of the SPD of Mg-Li alloys nowadays is to investigate how to refine the alloy grain structure to achieve FSS. FSS of Mg-Li alloys have greatly attracted the attention of researchers because the small grain size can increase the number of slidable grains and density of grain boundaries, which is favored by GBS [90].

Some researchers focused on refining the microstructure by the process of ECAE. Furui et al. [9] explored the superplasticity of Mg-8Li alloy using the combination of rolling and two-pass ECAE and reported to obtain ~970 % elongation at the temperature of 473 K with the initial strain rate of 1×10^{-4} /s, which is an exceptionally high elongation for the superplasticity of Mg alloys. Yoshida et al. [10] utilized the ECAE process to treat the Mg-10Li-1Zn alloy to explore the superplasticity of the alloy, and obtained the elongation of 391 % with the initial strain rate of 1×10^{-3} /s at 423 K.

Apart from the ECAE process, it has also been indicated that the process of high ratio extrusion can also be used for grain refinement for attaining a higher level of superplasticity. Dong et al. [12] investigated the application of high ratio extrusion to Mg-8Li-1Zn and Mg-8Li-3Zn alloy and found that this process is effective in inducing DRX which leads to the grain refinement in the extruded samples. The results showed that Mg-8.5Li-1Zn can demonstrate the elongation of 400 % at 623 K and 1.1×10^{-2} /s and Mg-8.5Li-3Zn can achieve the largest elongation of more than 540 % at the

temperature of 623 K with the strain rate of 1.18×10^{-2} /s.

The process of FSP is another efficient way to effectively refining the alloy grain structure. Liu et al. [11] used submerged FSP and water flow quenching to refine the microstructure of a dual-phase Mg-9.93Li-3.06Al-1.49Zn alloy. This treatment can produce a mixed alloy structure with fine, equiaxed, and recrystallized grains with high angle grain boundaries, which is favored by the SPD process. The result showed that the alloy after FSP can exhibit low-temperature superplasticity with the elongation of 330 % at the temperature of 473 K and high strain rate superplasticity with the elongation over 400 % at the temperature of 498-573 K. The maximum elongation was 630 %, obtained at the temperature of 473 K with the strain rate of 1×10^{-3} /s. By analyzing the activation energy of the SPD process, it was revealed that the dominant deformation mechanism is GBS controlled by grain boundary diffusion of β phase.

Traditionally, the SPD can be induced at high temperatures and with the grain sizes as small as possible. However, several researchers investigated how to realize high strain rate superplasticity and coarse-grained superplasticity. They can improve the forming efficiency of the deformation process, which can facilitate the wide applications of the materials in the industrial fields.

Liu, et al. [91] studied the high strain rate SPD of the Mg-8Li-2Zn alloy. The SPD experiments were conducted at 473-593 K using the Const*v* SPD method with the

initial strain rate from 1×10^{-2} to 1×10^{-1} /s, and the largest elongation of 279 % was obtained with the initial strain rate of 1×10^{-2} /s. It was indicated that GBS controlled by grain boundary diffusion is the main deformation mechanism for this alloy. Meanwhile, it was found in this research that cavitation is the critical fracture mechanism, and the fracture of the material is caused by the nucleation and coalescence of cavities. In addition, with relatively lower initial strain rate and higher temperature, the cavities near the grain boundaries have sufficient time for diffusion, which is favored by the large elongation of the material.

Some of the researchers studied the superplasticity of Mg-Li alloys with coarse grains. Lin, et al [92] conducted superplastic tensile testing experiments on Mg-10.73Li-4.49Al-0.52Y alloy at 473-623 K with the initial strain rates from 5×10^{-4} to 1×10^{-2} /s. The experimental material was treated by the 8-pass ECAE process from the as-cast state, and the average grain size after ECAE is 154.6 μm which is very large. The largest elongation of 512 % was obtained at the temperature of 523 K with the initial strain rate of 5×10^{-4} /s. The coarse-grained superplasticity of the Mg-Li alloy can be attained because of the introduction of the ECAE process to the as-cast alloy. ECAE can induce high densities of dislocation and internal elastic strains which is favored by recrystallization during SPD [93, 94]. In this study, the researchers also explored the effect of preheating on the alloy microstructure with the annealing process for 600 s at 473-623 K and found that the grains are refined at 573 K but coarsened at 623 K. The grain refinement is caused by partial recrystallization. After the deformation, it

was noticed that the grain structure is further refined in the gauge part, especially at 523 and 573 K. The recrystallization process is thermally activated, which can be enhanced by increasing either the deformation temperature or the strain. It was inferred that with the addition of Li, the stacking fault energy of Mg is increased, and due to the relatively high diffusion coefficient of Li, recovery is more easily to occur than recrystallization [95, 96]. However, due to the high density of elastic strain introduced by ECAE, there are abundant sites of nucleation for recrystallization which becomes the dominant process and causes grain refinement.

2.3 The theory of Maximum *m* superplasticity

As is discussed in the previous text, the common types of superplasticity can be divided into the FSS, in which fine grains are prepared, and ISS, in which the internal stress of the material is developed. However, these methods are more focused on transforming the material into a microstructure which is more beneficial for the occurrence of superplasticity. For the sake of enhancing superplasticity, apart from changing the material into a more suitable microstructure state, another possible route could be the adoption of a more suitable deformation method. In this thesis, the method of Max*m* SPD is applied for the SPD of Mg-Li based alloy. This innovative method can maintain the optimal deformation state of the alloy during SPD by continuously monitoring the *m* value and adjusting the deformation parameters.

The theory of Max*m* SPD was proposed by Wang et al. [13] to enhance the superplasticity of Ti alloys. It is known that the Ti alloys have wide applications in various industries but is very hard to deform, especially at room temperatures, and it usually requires a large force for the deformation of Ti alloys, which raises the requirements of the capacity of manufacturing equipment and the production cost. If the superplasticity of Ti alloys can be utilized, the deformation of Ti alloys can be much easier due to the lower force level and superior formability of the alloy during the SPD process. For the SPD processes, the strain rate sensitivity exponent *m* value is a critical parameter, which can indicate the material capability of resistance to necking and the state of superplasticity during SPD. In addition, a larger *m* value always corresponds to a better superplasticity state and further a larger attainable elongation in SPD tensile tests [97-100]. Meanwhile, the *m* value usually fluctuates as the deformation continues in the deformation process [73]. Therefore, if *m* can be retained at its maximum value throughout the SPD process, the best SPD state could also be maintained and the greater superplasticity might be achieved. The theory of Max*m* SPD was thus proposed in order to keep the maximum *m* value during SPD by simultaneous measurement of *m* value and dynamic control of the deformation strain rate, by which both the optimal strain rate and the maximum *m* value during the deformation process can be found and controlled during SPD.

It is widely recognized that the rheological behaviors of the superplastic materials can be delineated by the Backofen equation as shown in equation 2-1 [13]:

$$\sigma = K\dot{\varepsilon}^m \tag{2-1}$$

where σ is the true flow stress, K is a material constant, $\dot{\varepsilon}$ is the true strain rate, and m is the strain rate sensitivity exponent. For ideal or Newtonian-viscous flow behavior, the m value can be 1. Most metal material demonstrates $m < 0.2$, while for alloys during SPD, the m value can be larger than 0.4 [52]. The m value indicates the material resistance to necking, and a larger m value usually corresponds to the higher resistance to necking and the better state of superplasticity [13]. From equation 2-1, the following equation regarding the m value at a specific deformation time t can be obtained.

$$m = \frac{d(\ln \sigma_t)}{d(\ln \dot{\varepsilon}_t)} \tag{2-2}$$

Therefore, m is the slope of the $\ln \sigma_t - \ln \dot{\varepsilon}_t$ curve. Several methods of measuring the m value have been developed, but all of them are related to a variation of m value with $\dot{\varepsilon}$, as shown in **Fig. 2.5**, which indicates that there is an optimum $\dot{\varepsilon}$ corresponding to the largest m value. The methods for measuring the m value are stated as follows [42, 101].

(1) Determining m value by sudden change of strain rate

Changing the strain rate during the deformation process is the most widely used method. As shown in **Fig. 2.6 (a)**, in a constant speed tensile test, by suddenly changing the crosshead speed, the strain rate is changed and there will also be a sudden change of force. If the changed strain rate is maintained for a few percent to relieve transient effects, the load can be compared. The following equation relates the

measurement of *m* value to the force and velocity before and after the sudden change of strain rate, if *m* is hypothesized as almost independent of the strain rate during the sudden change.

$$m = \frac{d(\ln \sigma_t)}{d(\ln \dot{\varepsilon}_t)} = \frac{\Delta \ln \sigma_t}{\Delta \ln \dot{\varepsilon}_t} = \frac{\ln \sigma_2 - \ln \sigma_1}{\ln \dot{\varepsilon}_2 - \ln \dot{\varepsilon}_1} = \frac{\ln(\sigma_2 / \sigma_1)}{\ln(\dot{\varepsilon}_2 / \dot{\varepsilon}_1)} = \frac{\ln(P_2 / P_1)}{\ln(v_2 / v_1)} \qquad (2\text{-}3)$$

where *P* and *v* are the load and velocity of the corresponding points in **Fig. 2.6 (a)**.

(2) Conducting tensile testing experiments with different strain rates

By conducting several tensile tests with various velocities or strain rates, the $\ln \sigma_\varepsilon - \ln \dot{\varepsilon}_\varepsilon$ curves can be plotted for a certain strain value, as shown in **Fig. 2.6 (b)**. By means of curve-fitting, the slope of the $\ln \sigma_\varepsilon - \ln \dot{\varepsilon}_\varepsilon$ curve can be calculated. However, the disadvantage of this method lies in the increased number of experiments, which is not as convenient as the first method.

(3) Conducting stress-relaxation tests

The stress relaxation experiment is widely applied to investigate the time-dependent plastic flow of crystalline solids. The stress-relaxation test can be illustrated in **Fig. 2.7**. The experiment was started by conducting the tensile testing until a certain stress level, and then the movement of crosshead is stopped. The decrease in stress level is then observed as a function of time. When analyzing the stress relaxation tests, three approaches can be used to measure the *m* value, which are listed as follows. Among the three methods, the first method of equation 2-4 is mostly applied.

(i) A relation which is similar to equation 2-1 with the *m* value independent of the

strain rate over the relaxation rate was proposed [102], and in this case,

$$\ln \sigma_t = C + \frac{m}{m-1} \ln(t + D) \tag{2-4}$$

where C and D are constants. Therefore, the curve of $\ln \sigma_t - \ln t$ has a slope of $m/(m-1)$ when t >> D.

(ii) From another method [103] which share the same assumption as the last approach, the following equation can be obtained

$$\frac{1}{m} = \frac{d(\ln(-\dot{\sigma}_t)}{d(\ln \sigma_t)} \tag{2-5}$$

where $\dot{\sigma}_t$ is the stress rate of stress relaxation. In this case, *m* can be obtained from the slope of $\ln(-\dot{\sigma}_t) - \ln t$ graph, and the assumption of a constant *m* value is not required.

(iii) In this method, the assumption of the existence of an internal stress is used for the equation as follows [104, 105]

$$\sigma^* = \sigma_t - \sigma_i = K^* \dot{\varepsilon}^{m*} \tag{2-6}$$

Then the m^* can be derived as the slope of $((d \ln(-\dot{\sigma}_t)) / d\sigma_t)^{-1} - \sigma^*$ graph, and the relationship between *m* and m^* can be expressed as [104]

$$m = m^*(1 - (\sigma_i / \sigma_t)) \tag{2-7}$$

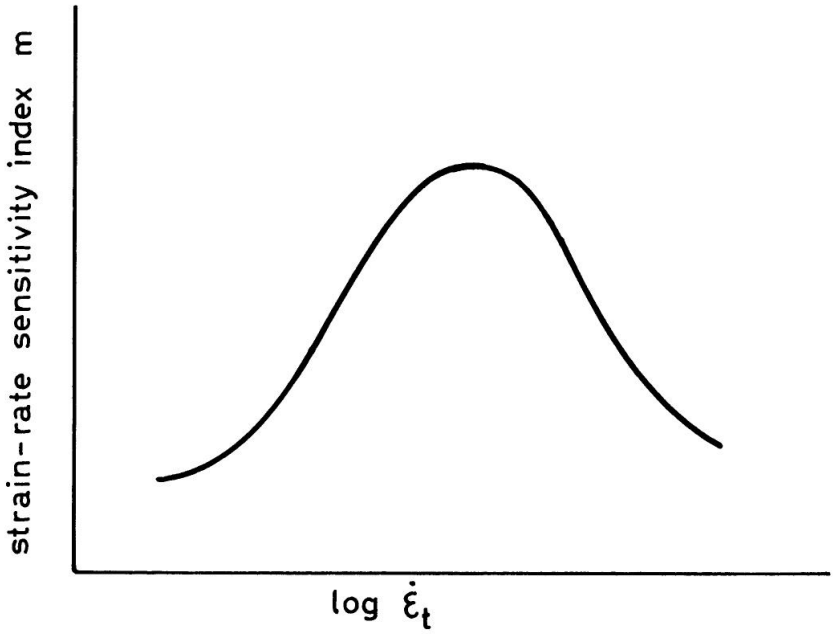

Fig. 2.5 Variation of *m* value with $\dot{\varepsilon}$ [42].

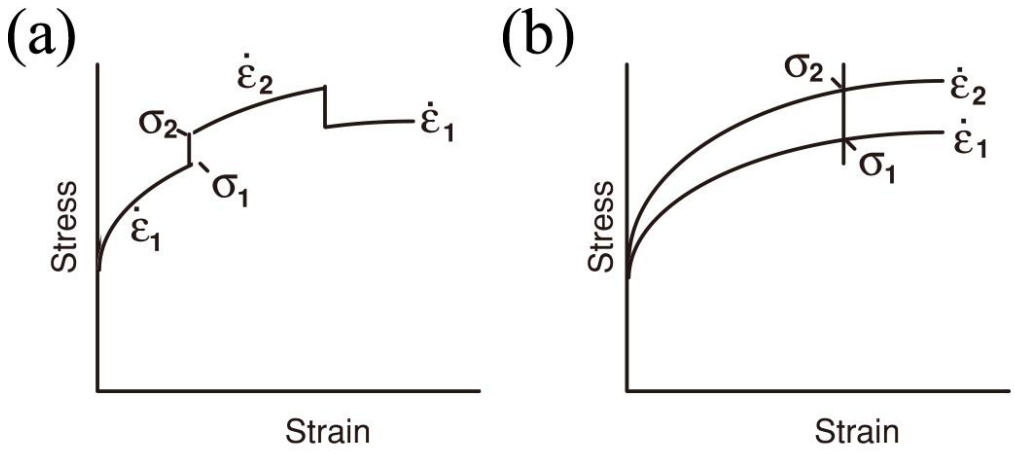

Fig. 2.6 *m* value measurement through (a) changing strain rate and (b) conducting tensile tests with different strain rates [101].

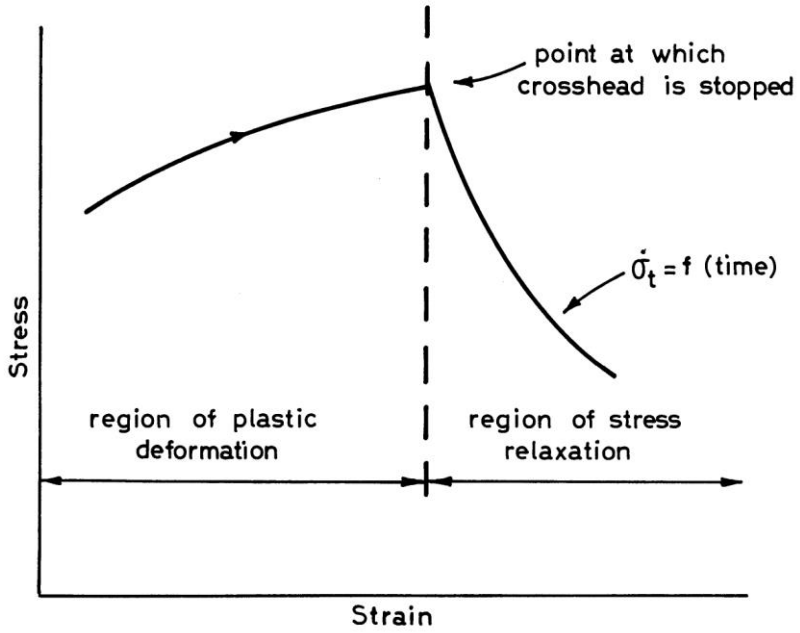

Fig. 2.7 Illustration of the stress relaxation experiment [42].

Since *m* is largely depended on the strain rate value, the maximum *m* value always corresponds to an optimum strain rate during SPD, according to **Fig. 2.5**. However, in the traditional deformation processes of Const*v* and CSR SPD, the *m* value cannot always be maintained as the maximum value, because *m* shifts dynamically if constant velocity or strain rate is applied. Therefore, in order to better control the *m* value, the deformation strain rate should also be changed dynamically to search for the maximum *m* value and the corresponding optimal strain rate. By simultaneously measuring the *m* value from the deformation process, the change of *m* value can be identified, which in turn provides feedback for further control of the strain rate. By cyclically controlling the strain rate, the loading-time curve can be obtained, as shown in **Fig. 2.8**. The change of strain rate during the deformation process is similar to the *m* value measuring method of suddenly changing the velocity, so the equation 2-3 can be

applied. Therefore, in the case of Max*m* SPD, the calculation of *m* value can be realized from the following equations,

$$m = \log(P_B / P_A) / \log(v_2 / v_1), \text{ for the increasing strain rate scenario,} \quad (2\text{-}8)$$

$$m = \log(P_B / P_C) / \log(v_2 / v_1), \text{ for the decreasing strain rate scenario,} \quad (2\text{-}9)$$

where P_A, P_B, and P_C are the loading force at point A, B, and C, and v_1 and v_2 represent the speed during the neighboring time increments.

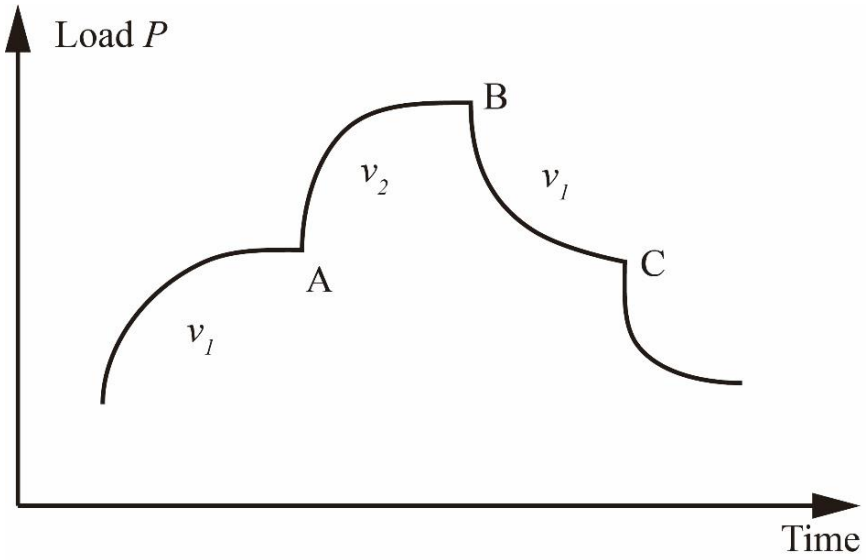

Fig. 2.8 Loading-time curve for measurement of *m* value [15].

The method of Max*m* SPD can largely enhance the superplasticity of Ti alloys. An elongation of 641 % was obtained for Ti-6Al-4V at the temperature of 900 °C, which is almost two times of the elongation in the conventional SPD process [13]. The elongation of 2300 % was obtained for Ti-6.5Al-3.5Mo-1.5Zr-0.3Si alloy, which is much larger than the best elongation of 1100 % for Const*v* SPD and 1260 % for CSR

SPD [15]. However, the single-step Max*m* SPD process usually requires the process of grain refinement during material preparation. If the grain refinement process can be simplified or even eliminated, the whole production process can be more efficient and beneficial to industrial applications.

The stepped SPD method was thus proposed to help the material reach the better superplasticity with no or less pre-processing steps and has been well applied to the SPD of Ti alloys [14, 16, 17]. The idea of stepped SPD is to divide the deformation process into two SPD steps and a clearance stage is applied between them. The rationale of the two-step SPD is illustrated in **Fig. 2.9**. In the first step, the material is deformed to a pre-planned strain by certain deformation methods, which is usually the traditional SPD methods including Const*v* and CSR SPD. In the clearance stage, the force exerted on the specimen is loosened and the material is held inside the furnace for a pre-planned time. This stage aims to act as the heat treatment process and refine the material microstructure by recrystallization and improve the deformability. In the second stage, the method of Max*m* SPD is usually applied, which is because the Max*m* SPD can maintain the best superplastic state of the material until fracture. This two-step deformation method has been well applied to the Ti alloys to further enhance the superplasticity. In addition, because of the existence of the first deformation step and the clearance stage, which can refine the grain structure, less or even no grain refinement processes are required, which saves much time and is more favored by the industrial applications. The maximum elongation of 1456 % was obtained for the Ti–

6.5Al–2Zr–1Mo–1V alloy by the Const*v*-Max*m* SPD process, which is much larger than the result obtained by the single-step Max*m* SPD deformation [16]. In another investigation, the best superplasticity with the elongation of 2053 % was obtained by Const*v*-Max*m* SPD, compared to the largest elongation of 1347 % by Max*m* SPD and 753.9 % by Const*v* SPD [16]. The promising and potential applications of Max*m* SPD in other alloys except Ti alloys have not been extensively explored before this research. Therefore, in this research, it is worthy to employ this innovative and useful deformation method for the SPD of Mg-Li based alloys to explore the potential applicability of Max*m* SPD.

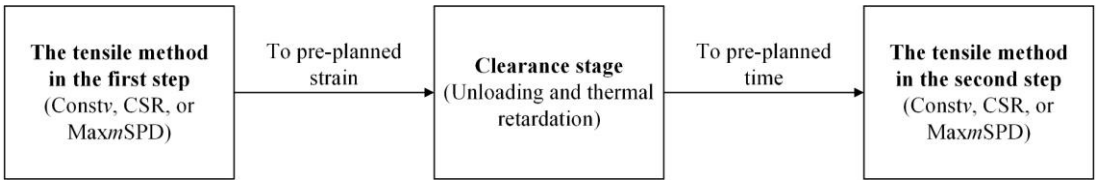

Fig. 2.9 Process of the two-step SPD method [16].

Chapter 3 Single-step Max*m* SPD of grain-refined Mg-Li based alloy

3.1 Introduction

The Mg-Li alloys have great potentials in various industries including military, engineering and biomedical clusters, which can be attributed to the combined material characteristics of lightweight, high stiffness-to-weight ratio and biocompability. The wide application of Mg-Li alloys can be achieved only if proper manufacturing processes of the material are developed. The main problem of Mg alloys in terms of manufacturing and production is the compromised formability caused by the existence of the HCP structure of Mg, which has fewer slip systems than the cubic-centered structure and thus exhibits poor ductility at room temperature. Due to this drawback, Mg alloys are mainly manufactured by casting processes. However, compared to the wrought materials, the as-cast products have inherent disadvantages like poor mechanical properties and surface quality, which limit the use of the material. The deformation process utilizing the material superplasticity could be a feasible way for manufacturing Mg alloys, because the material can exhibit extensively large elongation with low force level. For Mg-Li alloys, if they are used with the duplex phase structures, where HCP and BCC structures coexist, the existence of the second phase in the microstructure can be beneficial to superplasticity owing to the effect of inhibition of grain growth caused by the second phase. There have been a number of

attempts exploring the superplasticity of Mg-Li alloys, but most of them were intended to achieve FSS through various material treatment methods such as ECAE and FSP. Nevertheless, other possible means for enhancing the material superplasticity also needs to be investigated, among which optimizing the deformation route could be a feasible way. The deformation method of Max*m* SPD was therefore proposed for enhancing the superplasticity of Mg-Li alloys.

Max*m* SPD is a unique deformation method which can maintain the maximum *m* value of the specimen during the SPD process and maximize the deformation capacity of the material. The process can be realized by a tailor-made tensile testing machine with a computer control system embedded with the Max*m* SPD program. From the industrial application point of view, the variation of strain rate in the forming process can be accomplished by application of a servo-control system in the forming equipment. So far, the Max*m* SPD has only been successfully applied to the SPD of Ti alloys and significantly enhanced the superplasticity of Ti alloys compared to the conventional SPD methods [13, 15], but its promising and potential application in other alloys has not been extensively explored yet.

In this chapter, motivated by the potential application of Max*m* SPD in the deformation of Mg-Li alloys to achieve enhanced superplasticity, the aim of this investigation is to explore the best hot working process for fabricating micro-scaled bio-medical microparts or implants such as cardiovascular stents. The LA91 alloy was selected for

this research, which has the duplex α-HCP and β-BCC structures. The materials used for experiments are as-extruded samples which were extruded from the as-cast material, and the samples further processed by 4- or 8-pass ECAE after extrusion. Max*m* and CSR SPD experiments were conducted using the as-extruded, 4- and 8-pass ECAEed LA91 alloy samples at the temperature of 548, 573, and 598 K. It was found that Max*m* SPD demonstrated more promising superplastic potentials with the ECAEed samples than the as-extruded ones. The maximum elongation obtained was 563.7 %, by Max*m* SPD at the temperature of 573 K using 8-pass ECAEed material. The deformation behavior was studied and explored for better realization of SPD and identification of the optimal hot working process of the alloy in the future.

3.2 Experimental procedures

3.2.1 Material preparation

The material used in this research is LA91, which was originally cast from pure Mg, Li, and Al with argon protection. The cast ingot was then extruded into rods with the diameter of 10 mm at the temperature of 563 K and with the extrusion ratio of 25. In order to determine the composition of the alloy, the technique of inductively coupled plasma optical emission spectrometer (ICP) was employed. The testing result showed that the material contains 8.981 % Li and 0.9969 % Al (in wt. %), which is fairly close to the theoretical composition of LA91.

In order to refine the microstructure and grain size of the Mg-Li alloy, the method of ECAE was adopted for further processing the as-extruded material. The degree of grain refinement in the ECAE process is mainly determined by two factors: the intersection angle of the two channels 2Φ and the fillet angle 2ψ in the die, as illustrated in **Fig. 3.1**. Experiments have shown that when 2Φ is very close to 90° and 2ψ is as small as possible, the ultrafine grain structure with equiaxed grains can be achieved with the greatest efficiency [106-108], which is favored by the SPD process. In addition, the route of multi-pass ECAE is also crucial to the plastic deformation imparted to the billet. There are several possible routes for the ECAE process, as shown in **Fig. 3.2**. There is no rotation between each pass in route A, while 90° or 180° rotation is conducted between each pass in route B and C, respectively. The route B can be further divided into route B_A and B_C, where route B_A follows the alternating rotation of $\pm 90°$ between each pass and route B_C means to rotate the billet by 90° in the same direction after each pass [109]. As the evolution of microstructure by route B_c is the most efficient and rapid compared to the other routes [107], route B_c was selected for grain refinement in this research. With route B_C, the shape of a cubic element inside the billet can be restored after every 4-pass of ECAE processing [110]. Therefore, for the sake of effectively refining the grain size, 2Φ was set to be 90° and 2ψ was made as small as possible in the die design, and the route B_c with 4 and 8 passes was selected for the ECAE processing.

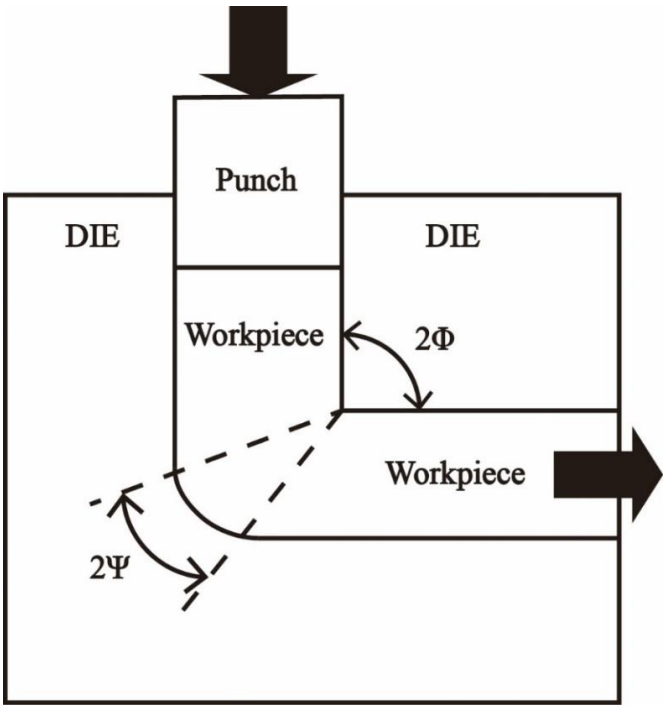

Fig. 3.1 Illustration of the ECAE process [106].

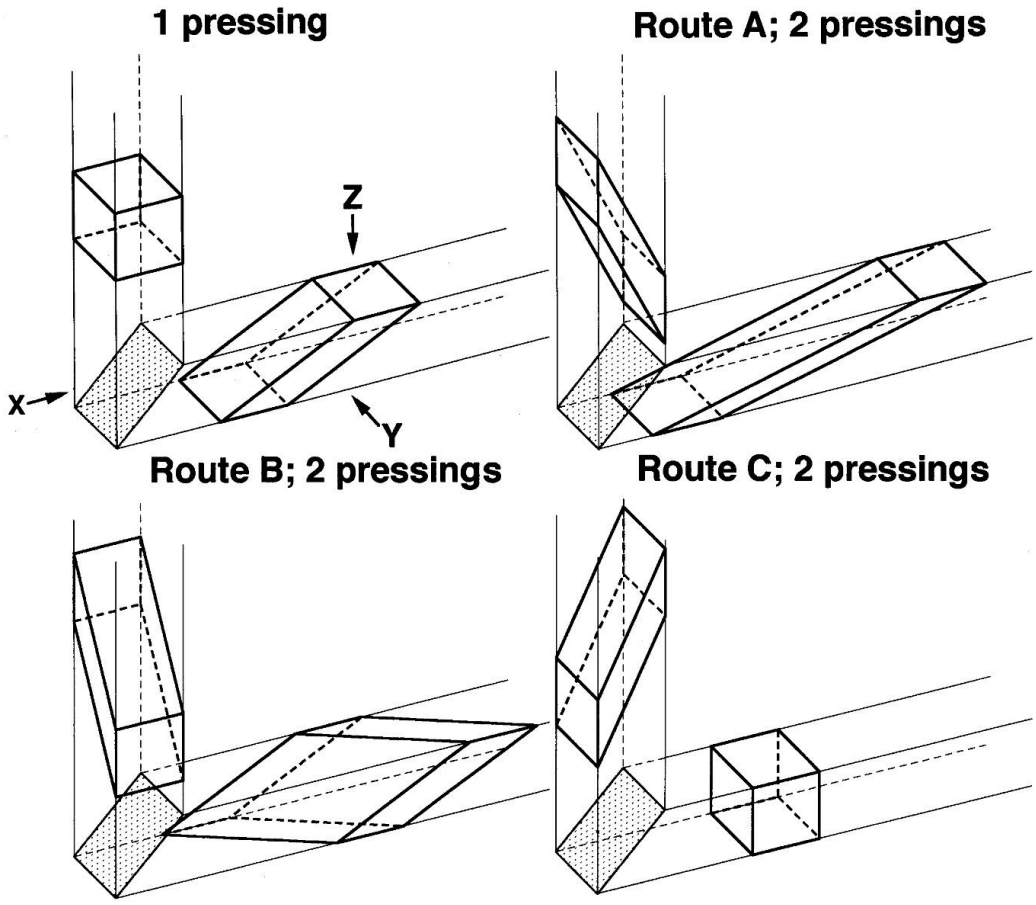

Fig. 3.2 Different routes of ECAE processes [109].

A forging equipment with a resistance furnace was utilized for the ECAE process, and a second thermocouple was inserted into the ECAE die with the distance of 11 mm away from the wall of the vertical channel for monitoring the temperature inside the die. The temperature of the ECAE process was 448 K. The ECAE process started after the temperature measured by the thermocouple reached the target temperature. During the experiment, billets were placed into the die after lubrication and then extruded by a punch with the pressing speed of 0.6 mm/s. After each pass, the billets were quenched with water immediately to keep the microstructure and avoid grain growth, and then they were put back into the channel again with lubrication after the rotation of 90° for the next pass of ECAE. In this way, the 4- and 8-pass ECAEed samples were prepared.

3.2.2 SPD tensile tests

The equipment used for SPD experiments was a CMT4104 electronic tensile tester with a computer controlling system, as shown in **Fig. 3.3**, which enables realization of experiments with both CSR and Max*m* SPD. The programmed software in the computer can continuously change the strain rates during the deformation process, which makes this device the only equipment which can achieve Max*m* SPD so far. The SPD specimens were machined parallel to the extrusion or ECAE direction with the gauge length of 15 mm and the gauge diameter of 3 mm. A preliminary experiment for narrowing down the experimental temperature range was conducted by CSR SPD

tensile tests using as-extruded specimens at the temperature from 473 to 623 K with the temperature interval of 25 K and the strain rate of 1×10^{-4} /s. By comparison of the elongation to failure, it was found that at the temperature of 548, 573 and 598 K, the specimens exhibited longer elongation, which could be the optimum SPD temperature of the alloy. The CSR and Max*m* SPD tensile tests were then conducted at the temperature of 548, 573 and 598 K by using the as-extruded, 4- and 8-pass ECAEed specimens. In CSR SPD, the strain rate is maintained to be constant, while in Max*m* SPD, the strain rate is changed dynamically by adjusting the deformation velocity to ensure the *m* value to be the maximum. In the Max*m* SPD process, three parameters in the process need to be determined, viz., initial velocity v_0, velocity increment Δv, and time increment Δt. For a certain time increment, the deformation speed is kept constant; after that, the velocity is either increased or decreased by Δv in order to retain a maximum *m* value. For easy comparison, the initial velocity v_0 = 0.07 mm/s was used in both CSR and Max*m* SPD. The other two parameters for Max*m* SPD were set as Δv = 0.03 mm/s and Δt = 6 s. The strain rate of CSR SPD was set as 1×10^{-4} /s. After the fracture, the specimens were quenched with water immediately to keep the microstructure and avoid grain growth.

Fig. 3.3 The tailor-made tensile testing system.

3.3 Results and discussion

3.3.1 Microstructures of as-extruded and ECAEed Specimens

The metallographic microstructure of the material was observed by optical microscopy (OM, Nikon Epiphot 200). The specimens were ground and polished along the required directions to the mirror surface and etched by 3 % HNO_3 water solution for 6 s to reveal different phases and grain boundaries. The longitudinal section of extruded samples or the half plane of ECAEed samples, and the cross-section of both the as-extruded and ECAEed material were observed and compared, because the samples tend to exhibit anisotropy. From **Fig. 3.4**, it can be found that the LA91 alloy has two phases, which is identical to the phase diagram of Mg-Li alloy, as shown in

Fig. 2.1. The two phases are presented by different colors under OM, in which the α phase tends to be whiter and the β phase is darker. The evolution of grain sizes of as-extruded and ECAEed samples is illustrated in **Fig. 3.5**. As there exist two phases in the alloy, it is more appropriate to illustrate the grain size of the material by separately describing the two phases. For the α phase, the grain size was measured by the average width of the α phase strips, while the grain size of the β phase was determined using the linear interception method according to the standard of ASTM-E112.

Upon extrusion, it is apparent that the α phase is elongated and tends to be aligned along the extrusion direction in the longitudinal section, which shows that the extrusion has created strong deformation texture in which the basal plane tends to be aligned [111]. After ECAE, the α phase strips are broken into small pieces, and it can be observed that there exist some α phase grains whose lengthwise direction is even perpendicular to the ECAE direction in 8-pass ECAEed samples. As shear deformation is the main deformation mechanism in ECAE and the grain refinement is realized in all the XYZ planes in the B_c route, the grains therefore tend to be more equiaxed. However, owing to the original elongated shape of α phase grains, the change of α phase grains could lie in segmentation of the α phase strips by breaking down the lengths and distortion of the grain shape. From the comparison of grain sizes between various samples as shown in **Fig. 3.5**, it is noted that the grain refinement effect is gradually reduced from the preliminary extrusion to 4- and 8-pass ECAE. The main reason could be that after the 4-pass ECAE process, the grain size of the alloy is

already fine enough, and a large fraction of the material is occupied by grain boundaries. From 4- to 8-pass ECAE, the GBS mechanism under shear stress could be very efficient and become the dominant deformation mechanism. On the other hand, when the grains are refined to a certain scale, much more energy is needed to further refine them [106]. Therefore, the grain sizes would not be further reduced when the limit is reached after 4 passes of ECAE.

In the cross section of the specimens, the α phase is in the shape of cracked long strips dispersed in the β phase. It is clear that the grain size of α phase in the cross-section tends to remain almost the same after ECAE processing, while the size of β phase is gradually refined with ECAE. The reason could be that the cross section of the billet is circumferentially compressed during extrusion while the longitudinal section is only compressed in the transverse direction. The grain refinement in the cross section is consequently much more severe and uniform than that in the longitudinal section. Moreover, the α phase shows more anisotropy than the β phase, which is because the α phase has long-strip shape while β phase grains tend to be more equiaxed. Thus, grain refinement of the α phase is distinct in the two sections and the α phase in the cross section may reach the above-mentioned limit of grain refinement earlier than that in the longitudinal section. Meanwhile, the grain refinement of the β phase tends to be more identical in both sections, which explains why the grain size of the β phase is similar in the two sections at each material processing stage.

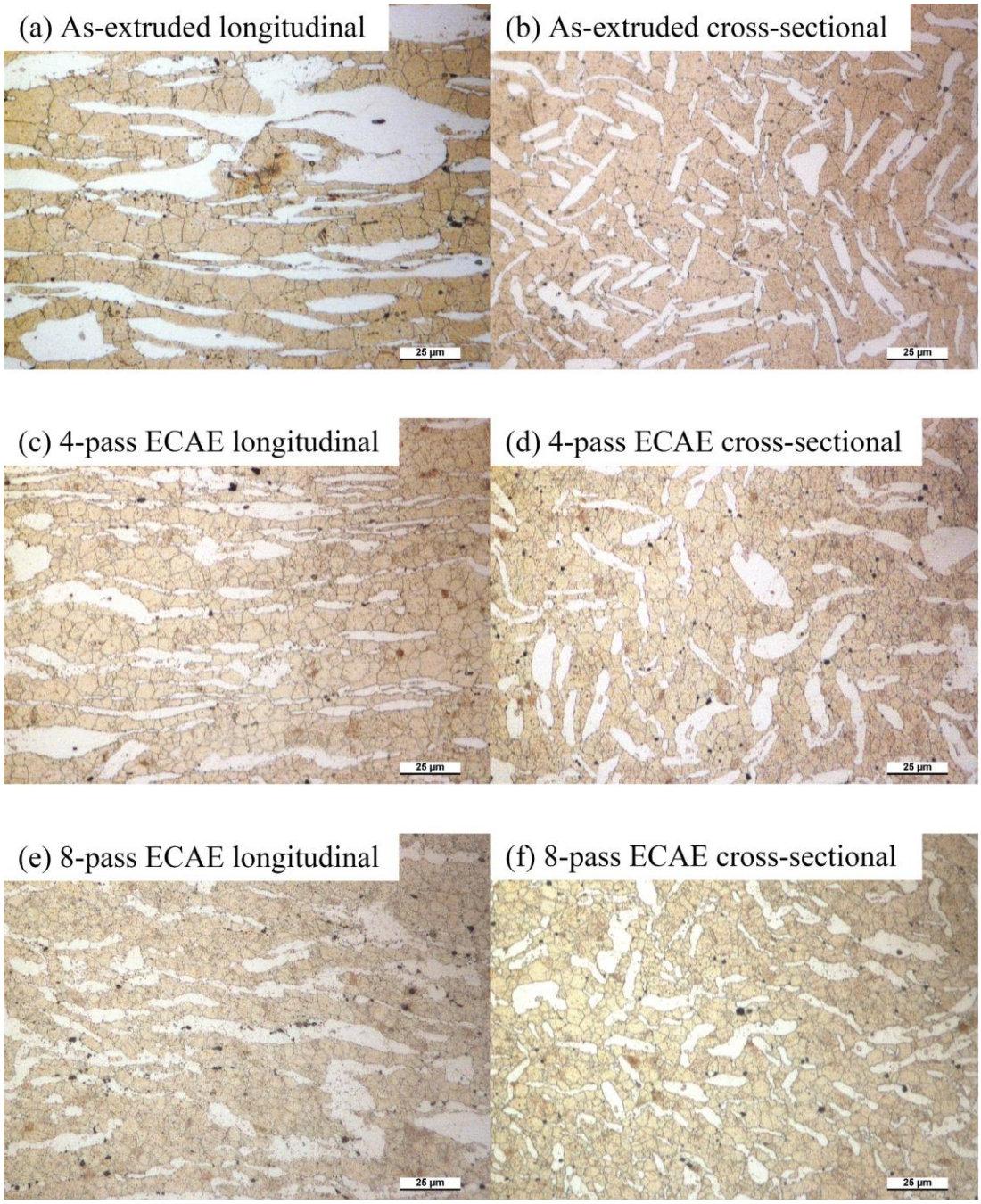

Fig. 3.4 Microstructure of the as-extruded and ECAEed materials: (a) as-extruded longitudinal, (b) as-extruded cross-sectional, (c) 4-pass ECAEed longitudinal, (d) 4-pass ECAEed cross-sectional, (e) 8-pass ECAEed longitudinal, and (f) 8-pass ECAEed cross-sectional.

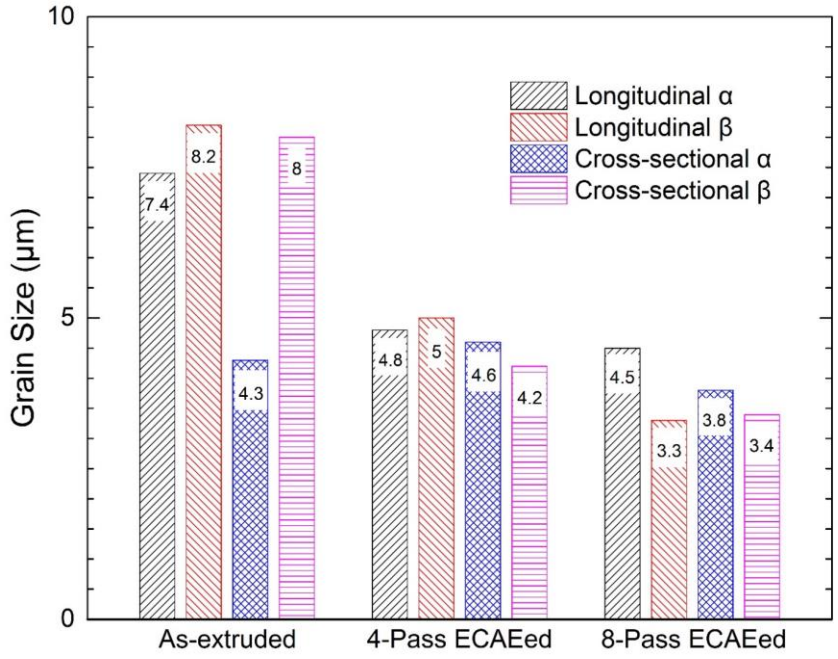

Fig. 3.5 Grain sizes of the samples after each stage of material processing.

3.3.2 Superplastic behavior

The optimum SPD temperature range was explored to narrow down the temperature selection for the subsequent SPD experiments, and the result is shown in **Fig. 3.6**. With the increase of temperature from 473 K, the elongation to failure in SPD tensile tests gradually increases and reaches the maximum at 573 K, and then decreases a little bit at 598 K. Meanwhile, the true ultimate tensile stress (UTS) during the SPD process decreases with the increase of experimental temperature. At higher temperature, the material is activated greatly and the atoms inside the material have a higher average kinetic energy. As a result, a lower critical shear stress is needed for GBS in SPD. The flow stress is thus lower at a higher temperature. The comparison of elongation to failure at different temperatures indicates that the as-extruded specimen can exhibit

better superplasticity at 548, 573, and 598 K, with 573 K being the optimum temperature. However, the optimum SPD temperature of as-extruded material may not be the same for the ECAEed samples. The temperatures of 548, 573 and 598 K were thus chosen as the SPD temperature for the subsequent SPD experiments using 4- and 8-pass ECAEed samples via the deformation approaches of Max*m* and CSR SPD.

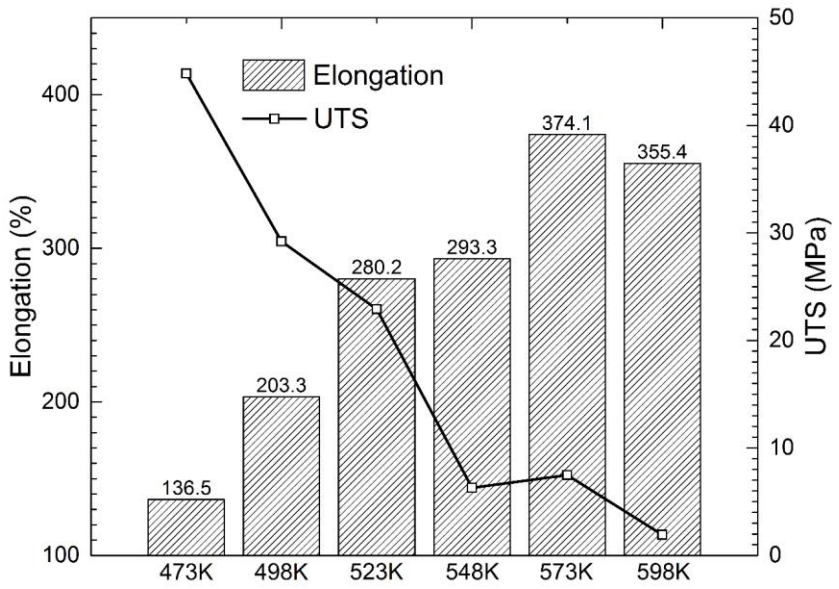

Fig. 3.6 Results of exploration of the optimal SPD temperature by using CSR SPD.

The specimens after SPD are presented in **Fig. 3.7**, in which the maximum elongation of 563.7 % was achieved at the deformation temperature of 573 K by Max*m* SPD. It can be observed that diffusional necking occurred within the whole gauge length. The detailed results of the SPD experiments are summarized in **Fig. 3.8**. In general, the experiments conducted at the temperature of 573 K showed the best superplasticity among the three temperatures of 548, 573 and 598 K. Meanwhile, the samples after ECAE processing exhibited the better superplasticity and greater elongation was

achieved when the number of passes of ECAE increased. When the grain size is small, the slidable grain boundaries and the rotatable grains on a unit cross section during the SPD process are more than the material with larger grain sizes, and there is more space for small grains to grow. As a result, small grains can lead to better superplasticity.

In spite of the advantages of Max*m* SPD for retaining the optimum superplastic state, Max*m* SPD can achieve the better superplasticity than CSR SPD only at certain experimental conditions. Generally, for the ECAEed specimens deformed at the temperature of 573 K, the induced superplasticity by Max*m* SPD is much better than that by CSR SPD. However, at other deformation temperatures, the situation is not always the same. Meanwhile, for the as-extruded samples, Max*m* SPD does not show better superplasticity than CSR SPD, which could be caused by the difference in grain refinement in extrusion and ECAE processes. The grain refinement of extrusion process tends to be more anisotropic, while the ECAE process can refine the grain structure more uniformly by the B_c route where all the XYZ planes can be refined. Such a result indicates the Max*m* SPD is more effective than CSR SPD for the ECAEed samples deformed at 573 K. Furthermore, the tested samples deformed at 598 K appear to suffer from severe oxidization than those deformed at a lower temperature. Therefore, the temperature of 598 K could be unsuitable for the SPD of Mg-Li alloys.

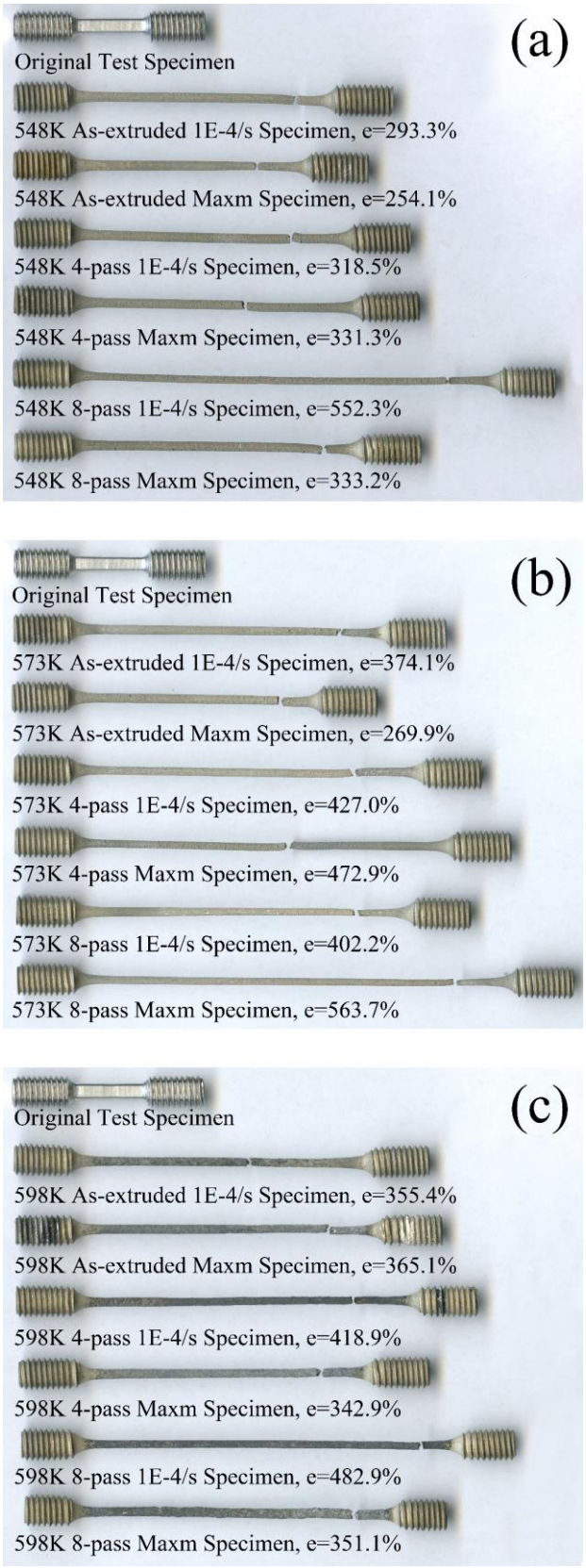

Fig. 3.7 Comparison of the samples deformed by Max*m* and CSR SPD at the temperature of (a) 548, (b) 573, and (c) 598 K.

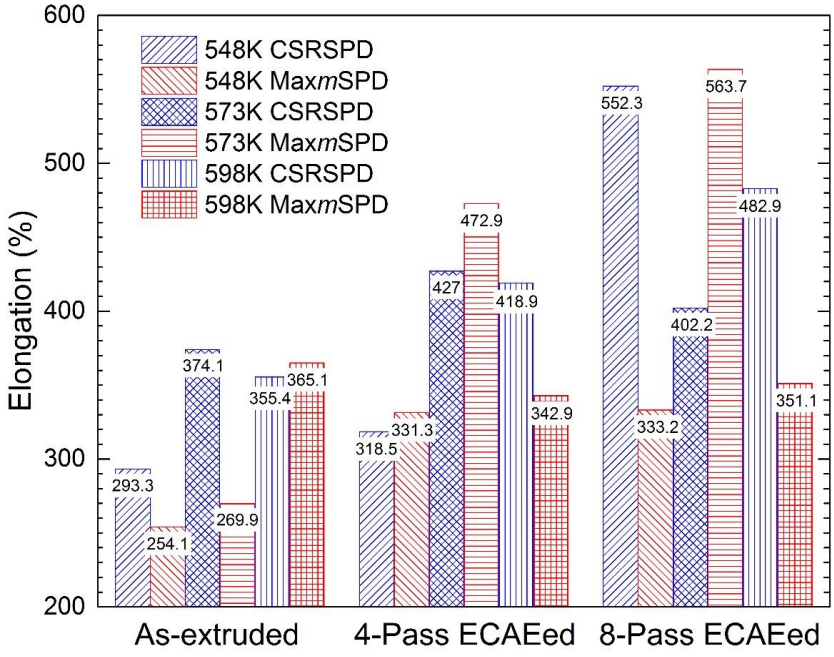

Fig. 3.8 Summary of SPD tensile test results.

The true stress-strain curves of the SPD tensile tests are presented in **Fig. 3.9**, in which the SPD processes conducted at the different temperatures are grouped in different figures for comparison. In general, the UTS during deformation decreases with the increase of deformation temperature. The variation of the curves could be considered as a result of the competition between hardening and softening effect [112]. For the process of CSR SPD, the overshoots and then drops rapidly at first. After a lower point is reached, the flow stress rises again slowly until fracture, as shown in **Fig. 3.9 (a), (c), and (e)**. At the beginning of SPD, strain hardening occurs as a result of movement and generation of dislocations [29], which leads to the overshoot of flow stress. As the deformation continues, the strain energy reaches the energy needed for DRX, the recrystallization process can then occur, which facilitates GBS and softens the material.

However, since the strain rate of deformation is low, the rearrangement or elimination of the generated dislocations cannot continuously provide sufficient driving force for DRX [113], so the softening effect cannot cancel out the hardening effect. Meanwhile, the grains grow at high temperature over time, and the rotatable grains and slidable grain boundaries on a unit area decrease, which hinders GBS and hardens the material. As a result, after the softening period during deformation, the material hardens, and the flow stress gradually increases when the hardening effect becomes stronger than the softening effect. However, it can be observed that there exists a second lower point on each of the stress-strain curve of CSR SPD, which indicates that the softening effect again becomes dominant. At the end of the process, the alloy is hardened until fracture when hardening becomes dominant. The second lower point in flow stress could be induced when enough driving force for DRX is accumulated for the softening mechanism during the deformation. Nevertheless, due to the enlarged grain size, the GBS mechanism is weakened, and the flow stress quickly changes into an increasing tendency afterwards. For the Max*m* SPD process, in the beginning, the true stress-strain curve exhibits hardening followed by softening, which is similar to CSR SPD. After that, the stress fluctuates at a low level as a result of the dynamic control of the deformation strain rate. The overall pattern of Max*m* SPD curves is similar to CSR SPD curves, in which stress increases after reaching a second lower peak in the course of deformation, but the phenomenon is more obvious in CSR SPD.

The variation of *m* value in the Max*m* SPD process is shown in **Fig. 3.10**. The *m* value was calculated based on the equations 2-8 and 2-9 with the parameters shown in **Fig. 2.8**. The strain rate sensitivity *m* value can represent the superplastic state of the material in SPD processes, and a larger *m* value usually indicates the better superplasticity. Since the *m* value fluctuates dramatically in Max*m* SPD processes, an average of every 20 data points was used to plot the curves as shown in **Fig. 3.10**. For easy comparison between different Max*m* SPD processes, the percentage of the true strain of SPD was used as the horizontal axis. At 548 and 573 K, the *m* value of the 8-pass ECAEed samples is always the largest, indicating the best superplastic state, followed by the 4-pass ECAE and the as-extruded samples. Meanwhile, the *m* value fluctuates severely at 598 K, while the variation of *m* value is steadier at the temperature of 548 and 573 K. Due to the unsteady superplastic flow, the temperature of 598 K may not be feasible for the realization of Max*m* SPD of LA91 alloy. The average *m* value during Max*m* SPD at various temperatures is summarized in Table 1. The result indicates that $m \geq 0.3$ is the necessary condition for the LA91 alloy to enter the superplastic state, and the *m* value increases with the number of ECAE passes.

The microstructures of the specimens after SPD at 573 K were examined by OM (Nikon Epiphot 200), which is shown in **Fig. 3.11**. Since all the microstructures are similar, only the 8-pass ECAEed specimens are presented. The grain size of the α phase was measured, and the result shows that the α phase sizes of both the specimens in **Fig. 3.11** are ~15 μm, which indicates that the grain size of all types of samples has

grown and become almost the same. Meanwhile, the α phase grains have become more equiaxed, compared to the elongated shape before deformation, which shows that there exists DRX during SPD. In addition, it can be found that there are more recrystallized grains in the 8-pass ECAEed samples after Max*m* than CSR SPD, which results in a smaller average α phase size as well as the largest elongation by 8-pass ECAEed samples deformed by Max*m* SPD. While for the as-extruded samples, there are more new grains in the CSR SPD processed samples, leading to a longer elongation than Max*m* SPD. For the 4-pass ECAEed samples, the distinction between the two SPD processes is not obvious, which corresponds to a smaller difference in the final elongation. From the comparison, it can be concluded that the Max*m* SPD process is more favored by the ECAEed samples than the as-extruded samples, which could be explained by the previous discussion that the ECAEed samples exhibit more isotropy than the as-extruded samples, and the material containing equiaxed grains might be a necessary condition for Max*m* SPD to demonstrate its capability.

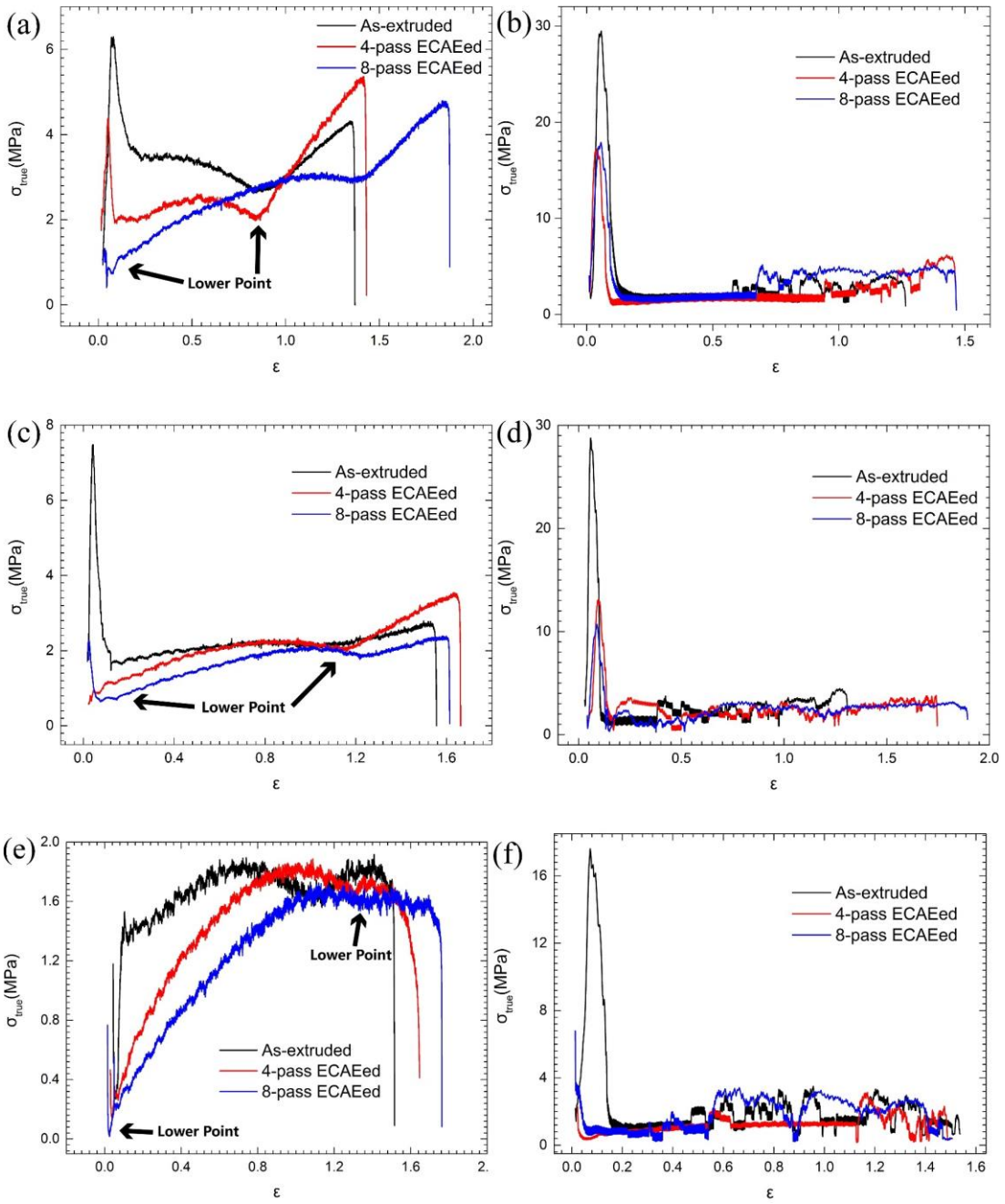

Fig. 3.9 True stress-strain curves of SPD tests at different conditions: (a) 548 K, CSR SPD; (b) 548 K, Max*m* SPD; (c) 573 K, CSR SPD; (d) 573 K, Max*m* SPD; (e) 598 K, CSR SPD; and (f) 598 K, Max*m* SPD.

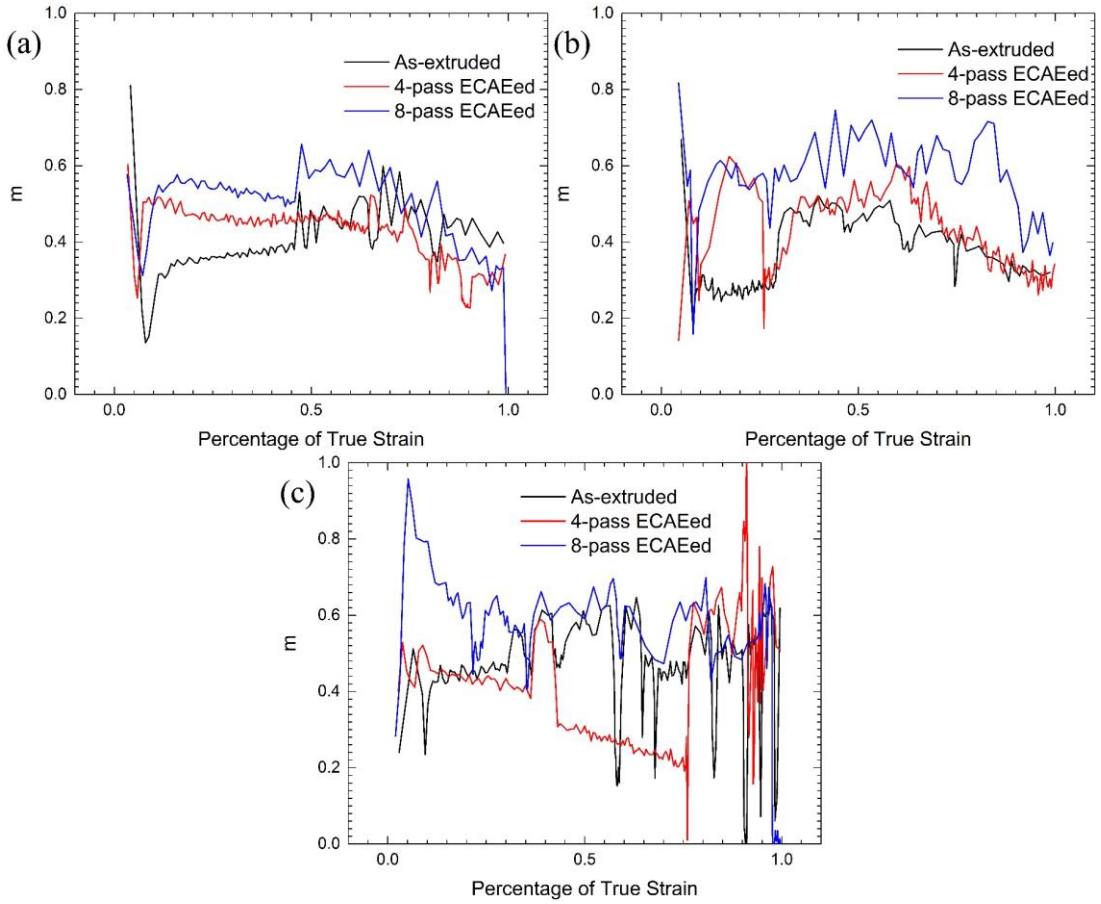

Fig. 3.10 *m* value variation during Max*m* SPD conducted at the temperature of (a) 548, (b) 573, and (c) 598 K.

Table 1 Comparison of the average *m* value in Max*m* SPD.

Average *m* value	548K	573K	598K
As-extruded	0.4	0.35	0.45
4-pass ECAEed	0.43	0.42	0.4
8-pass ECAEed	0.5	0.57	0.53

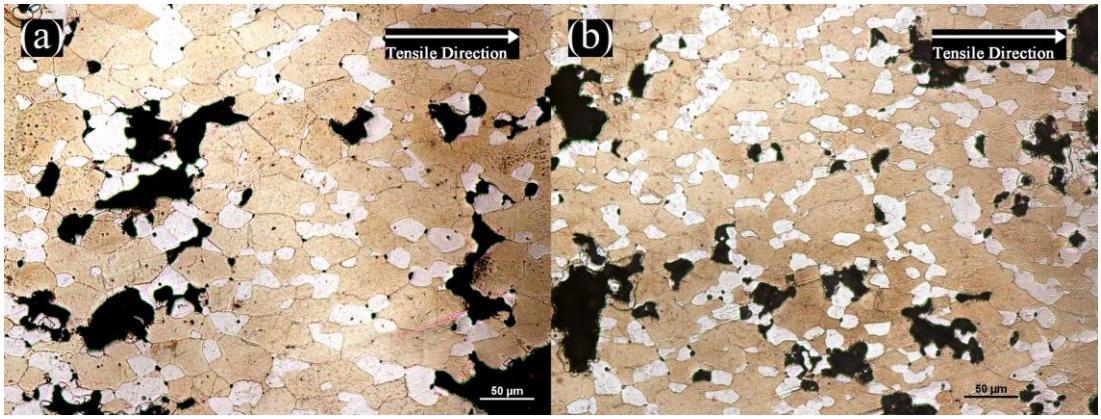

Fig. 3.11 Microstructure after SPD: (a) 8-Pass ECAEed samples, CSR SPD at 573 K, 1E-4 /s; (b) 8-Pass ECAEed samples, Max*m* SPD at 573 K.

3.3.3 Fracture mechanisms

Since the microstructure near the fracture region of all types of the samples is almost the same, the 4-pass ECAEed specimens deformed at 573 K are presented and discussed. The longitudinal section of the 4-pass ECAEed specimens observed by OM (Nikon Epiphot 200) is shown in **Fig. 3.12**, and the fracture morphology for 4-Pass ECAEed samples observed by a scanning electron microscope (SEM, JEOL/Nikon JCM 6000) is presented in **Fig. 3.13**. From **Fig. 3.12**, it can be observed that the grains of both α and β phases have grown after the SPD process. Before the occurrence of fracture, there were many voids (the black area inside the material) formed near the fracture region, and the final fracture is as a consequence of the coalescence of those fractured voids. It can also be noticed that near the fracture region, the percentage of α phase has increased much compared to the specimens before the SPD and fracture

occurred either inside the α phase or at the boundary between α and β phases. In the fracture morphology shown in **Fig. 3.13**, both the intergranular and transgranular fractures can be observed. There exist some holes on the fracture surface, in which the interior of the aforementioned voids can be observed. The fracture behavior indicates that GBS controlled by diffusion is the main mechanism in the SPD process. As for the increase of α phase percentage, there perhaps exists stress-induced phase change in which a portion of β phase is transformed into α phase due to the high stress level near the fractured region, because it can be found from the phase diagram shown in **Fig. 2.1** that there is no temperature-induced phase change at the temperature of 573 K. The detailed fracture mechanism of the Mg-Li alloy in the SPD process needs further exploration in the future. Severe oxidization was observed on the fracture surface, as the experiment was carried out in the air and the fracture surface was quickly oxidized after the specimen was broken at high temperatures.

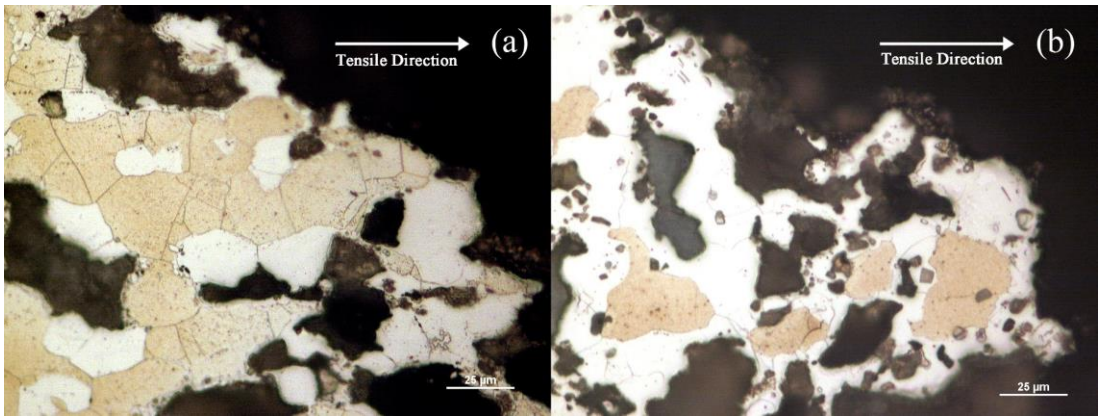

Fig. 3.12 The microstructure of the specimens deformed at the temperature of 573 K near fracture region: (a) 4-Pass ECAEed samples, CSR SPD; (b) 4-pass ECAEed samples, Max*m* SPD.

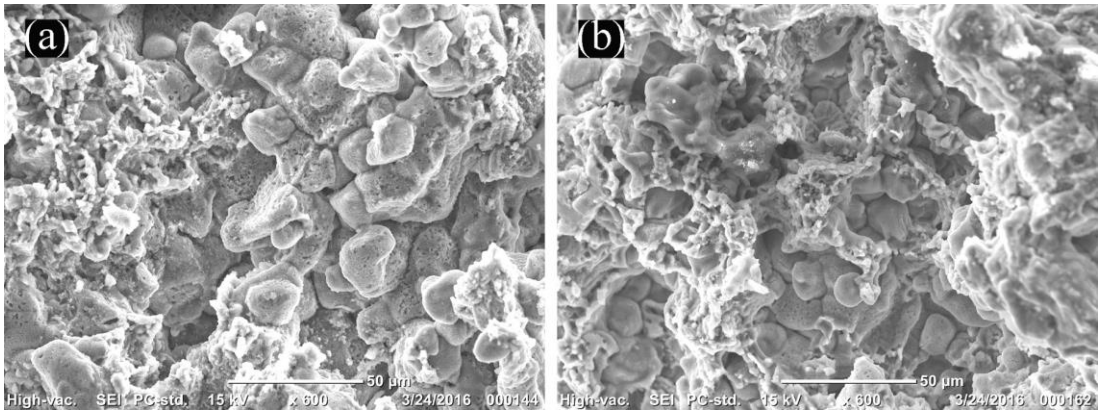

Fig. 3.13 Fracture morphology observed by SEM: (a) 4-pass ECAEed samples, CSR SPD at 573 K; (b) 4-pass ECAEed samples, Max*m* SPD at 573 K.

3.4 Conclusions

The applicability of Max*m* SPD to Mg-Li based alloys was investigated by conducting both Max*m* and CSR SPD at the temperature of 548, 573 and 598 K using the duplex phase LA91 alloy with different grain sizes for easy comparison. The following findings have been obtained through this investigation.

(1) Experiments conducted at 573 K induced the best superplasticity among the above-mentioned three temperatures, and the greatest elongation of 563.7 % was obtained at 573 K by 8-pass ECAEed samples by Max*m* SPD. Meanwhile, the greatest elongation induced by CSR SPD was 552.3 %, obtained by the 8-pass ECAEed sample at 548 K. The temperature of 598 K is unsuitable for SPD due to the unsteady superplastic state and severe oxidization.

(2) Under the same deformation conditions, the 8-pass ECAEed samples lead to better

superplasticity than 4-pass ECAEed samples, and the 4-pass ECAEed samples can induce better superplasticity than the as-extruded samples. Meanwhile, more passes of ECAE corresponds with a larger *m* value, viz., a better superplastic state throughout the deformation process.

(3) Max*m* SPD is more applicable to the samples processed by the combination of extrusion and ECAE than the material processed only by extrusion, owing to the more isotropic grain structure produced by ECAE.

(4) Both intergranular and transgranular fractures were observed on the fracture surface of the alloy. An increased portion of the α phase occurred near the fracture region, and cavities were formed either inside the α phase or at the boundary of the two phases.

Chapter 4 Enhanced Max*m* SPD of Mg-Li based alloy by a two-step SPD method

4.1 Introduction

In Chapter 3, the Max*m* SPD was explored for enhancing the superplasticity of Mg-Li alloys, and the ductility of the material has been significantly increased. It has been proved that the Max*m* SPD is more favored by the material which is processed by the combination of extrusion and ECAE than the as-received material which is processed only by extrusion because the grain structure of the latter material tends to be more anisotropic. However, the grain refinement process like ECAE is quite complex and time-consuming, which is not very feasible for industrial applications, and new methods which can be tangibly and easily implemented need to be developed to help achieve high superplasticity.

The stepped SPD method was thus considered to be applied to the as-extruded LA91 alloy in this research. This method was developed to help the material reach the better superplasticity with no or less pre-processing steps and has been well applied to the SPD of Ti alloys [14, 16, 17]. The idea of stepped SPD is to divide the deformation process into two SPD steps and a clearance stage applied in between in order to act as the heat treatment process and improve the property of the material and further the deformability. The stepped SPD process is illustrated in **Fig. 2.9**. In the studies of

applying the stepped SPD method to Ti alloys, Const*v* and Max*m* SPD were selected for the first and second steps, respectively [14, 16, 17]. However, in this study, in order to fully exploit the characteristics of stepped SPD, both Const*v* and CSR SPD were used in the first step and the Max*m* SPD was adopted in the second step. For the sake of confirming the optimal parameters for each SPD method and the suitable amount of pre-elongation for the LA91 alloy, single-step SPD tests by Const*v*, CSR and Max*m* SPD were conducted at first. The stepped SPD tests were then conducted by Const*v*-Max*m* and CSR-Max*m* SPD with the pre-elongation from 50 to 250 % in the first step. The largest elongation of 621.1 % was obtained by CSR-Max*m* SPD with the pre-elongation of 250 %, which is even larger than the result of 563.7 % in Chapter 3 where grain-refined materials were applied by single-step Max*m* SPD. The deformation and fracture mechanisms of the two-step SPD with LA91 alloy were studied in such a way to better exploit the maximum *m* superplasticity of the alloy.

4.2 Experimental procedures

4.2.1 Material preparation

The as-extruded LA91 alloy was selected and applied in this research. The alloy was firstly cast from powders of pure Mg, Li and Al in an argon atmosphere, and the cast ingot was then extruded into rods with the extrusion ratio of 25 at 563 K. The technique of ICP was used to test the material composition, which shows that the alloy is composed of 8.829 % Li and 1.063 % Al (in wt %) , which is very close to the

theoretical value.

The rod materials were machined into dog-bone shape specimens for the SPD tensile tests. The gauge length of the specimen is 15 mm, and the gauge diameter is 3 mm. The length direction of the specimen is parallel to the extrusion direction of the rod.

4.2.2 Single-step and two-step SPD Tensile Tests

It has been confirmed in the previous chapter that the optimal SPD temperature for LA91 alloy is 573 K, which was also adopted for the SPD tests in this research.

Single-step SPD tensile tests by using Const*v*, CSR and Max*m* SPD methods were first conducted to confirm the optimal parameters during the deformation process, and these selected parameters were then used in the two-step SPD tests. For the Const*v* SPD processes, the initial strain rates of 0.00025, 0.0005, and 0.001 /s, viz., the corresponding velocities of 0.195, 0.39, and 0.78 mm/min were chosen as the potential parameters. For the CSR SPD process, the strain rates of 0.00025, 0.0005, and 0.001 /s were selected to search for the optimum strain rate. Meanwhile, the same parameters in the Max*m* SPD tests used in chapter 3 were applied. The SPD tensile tests were conducted after the holding time of 10 min at 573 K in the furnace, and the samples were quenched after the completion of SPD tests to preserve their microstructures at the working temperature. After comparing the final elongation obtained in the SPD

processes, the optimal speed of 0.39 mm/min for Const*v* SPD and the optimal strain rate of 0.0005 /s for CSR SPD were selected as the optimal parameters for two-step SPD tests.

The two-step SPD method was then explored. The process of the two-step tests can be described as follows. In the beginning, the testing specimen was placed onto the gripper in the furnace and held for 10 min at 573 K. The first step of deformation was to realize Const*v* (with the speed of 0.39 mm/min) and CSR SPD (with the strain rate of 0.0005 /s), and the pre-elongation from 50 to 250 % was achieved. After a clearance stage of 10 min, the specimen was further deformed by Max*m* SPD until fracture. The fractured specimens were finally quenched to preserve the microstructures at high temperature. Max*m* SPD was applied in the second stage because it can maintain the best superplastic state of the material, such that the best state of superplasticity can be attained. To research on the microstructural evolution after the first deformation step, some of the specimens were quenched and collected after the first step with the pre-elongation from 50 to 250 % to observe their microstructures.

4.2.3 Preparation of microstructures of specimens

The metallurgical microstructure of the specimens was prepared by the same method used in Chapter 3.

4.3 Results and discussion

4.3.1 Single-step SPD experiments

Single-step SPD tensile tests using Const*v*, CSR and Max*m* SPD were conducted at the beginning of this research to determine the optimum parameters as well as providing a reference for comparison between the single-step and two-step SPD tests. The velocities of 0.195, 0.39 and 0.78 mm/min and the strain rates of 0.00025, 0.0005 and 0.001 /s were adopted for Const*v* and CSR SPD, respectively. Meanwhile, the parameters of initial velocity v_0 = 0.07 mm/min, velocity increment Δv = 0.03 mm/min and time increment t = 6 s were utilized for Max*m* SPD.

The elongation obtained by different SPD methods with different process parameters are summarized in **Fig. 4.1**. In general, the lowest two velocities and strain rates in Const*v* and CSR SPD can induce the largest elongation among the same SPD method, which is because the high velocity or strain rate cannot provide enough time for DRX to occur, such that the fracture may happen at an earlier stage. It can also be observed that Const*v* SPD can achieve larger elongation than CSR SPD when the initial strain rate of Const*v* SPD is the same as the strain rate in CSR SPD, which is because the speed is constant in Const*v* SPD but keeps increasing in CSR SPD to maintain the constant strain rate during deformation, and a higher average speed might not guarantee enough degree of DRX through the SPD process.

Since the lowest two velocities and strain rates in Const*v* and CSR SPD led to similar elongation results among the same SPD method, considering the forming efficiency, the velocity of 0.39 mm/min and the strain rate of 0.0005 /s were selected as the optimal parameters for Const*v* and CSR SPD in the two-step SPD experiments.

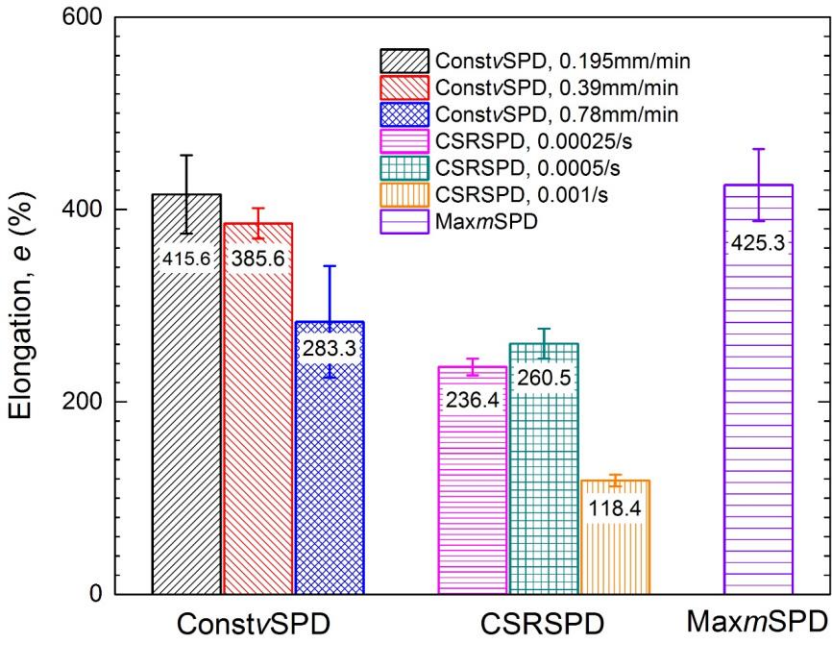

Fig. 4.1 Results of single-step SPD experiments.

The fractured specimens after tensile tests by the three SPD methods with the optimal parameters are presented in **Fig. 4.2**, and the corresponding true stress-strain curves are plotted in **Fig. 4.3**. The elongation to failure of Max*m* SPD is the largest among the three SPD methods, but Max*m* SPD cannot induce much better superplasticity than the other two conventional SPD methods, which indicates that the Max*m* SPD is not much more efficient than the conventional methods if the as-extruded alloy is used. It can be observed that the tendency of the curves of Const*v* and CSR SPD are quite

similar, in which the stress quickly drops after a peak value is achieved, but the stress ceases to decrease and rises gradually until the fracture. In the beginning, the rise of stress results from strain hardening, which is caused by the movement and generation of dislocations [114]. As the deformation continues, DRX occurs, and the material is gradually softened. The softening mechanism becomes dominant while the strain energy is accumulated, and the true stress is decreased fast from its peak value, after which the material enters the superplastic state. In the superplastic state, the main deformation mechanism is GBS. After a certain amount of elongation, due to long-time exposure of the workpiece in the high-temperature environment, grain growth in the alloy becomes severe, which decreases the number of grains and slidable grain boundaries on a unit area and is harmful to GBS. The hardening effect therefore becomes dominant again, and the stress is increased until the end of the deformation process as the grains grow further. Compared to the smoother curves of Const*v* and CSR SPD, the curve of Max*m* SPD is more undulatory. According to the rationale of Max*m* SPD, the optimal strain rate is always searched throughout the forming process to look for the highest *m* value, leading to the fluctuation of flow stress and the wavilness in the true stress-strain curve.

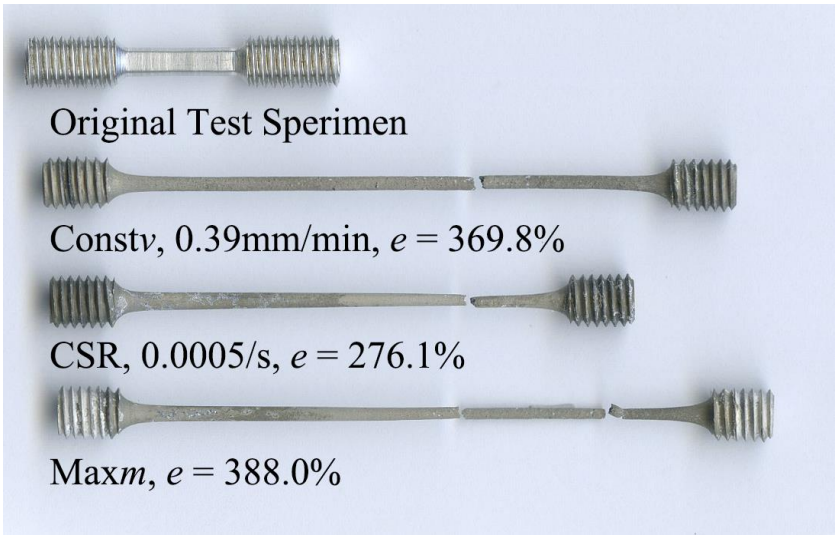

Fig. 4.2 Fractured specimens after single-step tensile tests by different SPD methods.

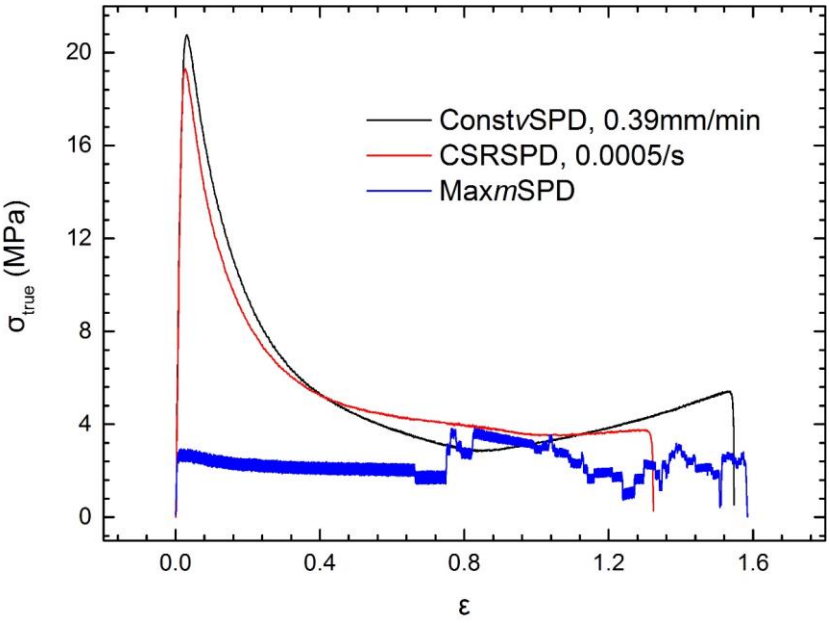

Fig. 4.3 True stress-strain curves of single-step SPD tests by different SPD methods.

4.3.2 Two-step SPD experiments

The two-step SPD tensile tests were conducted by using Const*v*-Max*m* and CSR-Max*m* SPD methods. The velocity of 0.39 mm/min and the strain rate of 0.0005 /s, which had been confirmed as the optimal parameters by the single-step SPD experiments, were employed in the first step of deformation by using Const*v* and CSR SPD, respectively. For the second step, the initial velocity v_0 = 0.07 mm/min, velocity increment Δv = 0.03 mm/min and time increment t = 6 s were used for Max*m* SPD. The samples after the two-step SPD tests are shown in **Fig. 4.4**, in which diffusional necking can be found throughout the whole gauge length. It can be noted that the two-step deformation method can largely extend the deformation limit of the material. The largest elongation obtained by the single-step SPD is 425.3 % by Max*m* SPD, while the largest elongation for the two-step deformation method is 621.1 % which was obtained by the CSR-Max*m* SPD with the pre-elongation of 250 %. This result is even better than the largest elongation of 563.7 % in the previous chapter by single-step Max*m* SPD with the specimen processed by 8-pass ECAE. This indicates that the two-step deformation method can effectively improve the superplastic capacity of the LA91 alloy than the single-step Max*m* SPD.

From **Fig.4.4**, for SPD tensile tests by using Const*v*-Max*m* SPD, the final elongation after fracture is increased with the pre-elongation from 50 to 200 % but shows a decreasing tendency when the pre-elongation is greater than 200 %. The largest

elongation for Const*v*-Max*m* SPD is 570.7 % when the pre-elongation is 200 %. However, the final elongation by using CSR-Max*m* SPD is generally increased with the pre-elongation from 50 to 250 %, and the largest elongation of 621.1 % was achieved when the pre-elongation in the first step is 250 %.

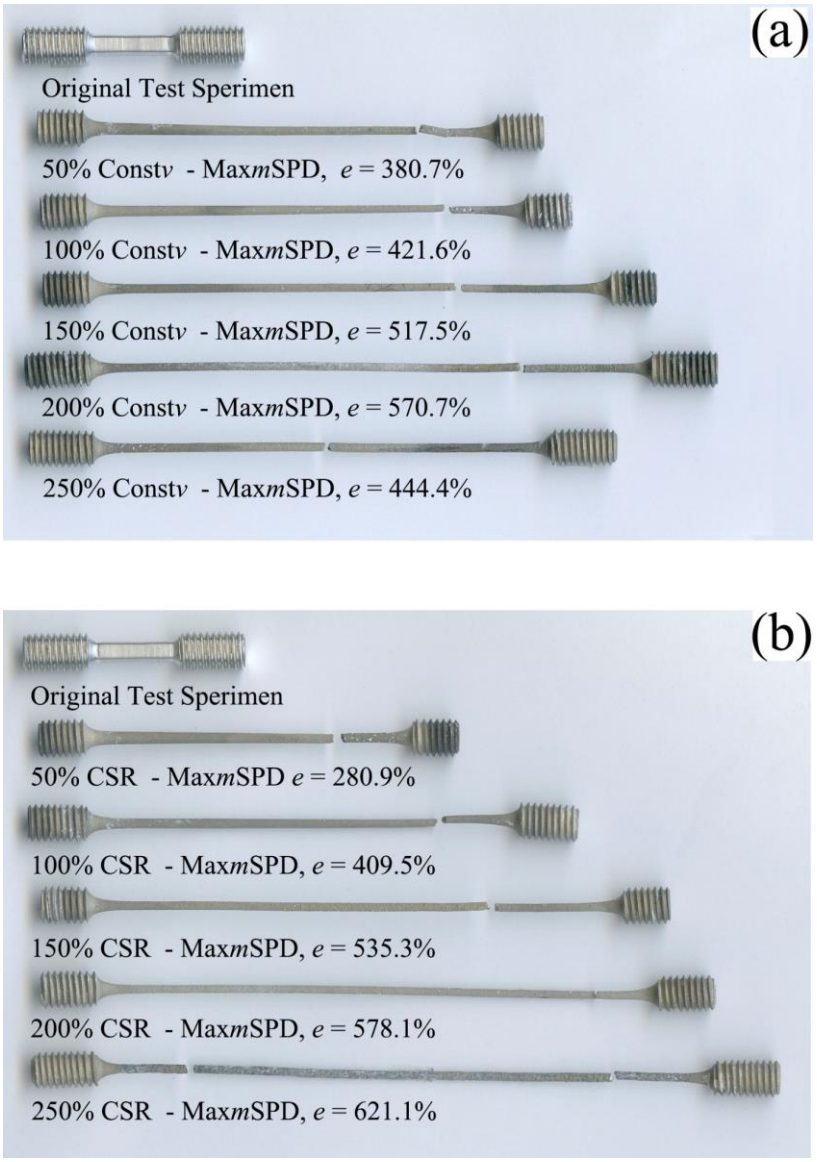

Fig. 4.4 Samples deformed by two-step SPD methods of (a) Const*v*-Max*m* SPD and (b) CSR-Max*m* SPD with different pre-elongation.

The true stress-strain curves of the two-step SPD tests are shown in **Fig. 4.5**. The curves are the combination of single-step curves of Const*v* or CSR SPD as the first part and Max*m* SPD as the second part. When the pre-elongation is accomplished, the stress becomes zero because the specimen is unloaded. The clearance stage of 10 min was then applied to improve the material property, after which the Max*m* SPD was applied until fracture of the specimen. For the pre-elongation smaller than 150 %, the curves of the second step of Max*m* SPD is generally steadier or rises only a bit, which is similar to the curve of single-step Max*m* SPD in **Fig. 4.3**. However, when the pre-elongation is larger than or equal to 150 %, the trend for the Max*m* SPD becomes increasing until the fracture. This phenomenon could be explained as follows. For single-step Max*m* or two-step SPD methods with smaller pre-elongation, the grains in the material are still relatively small, and the average grain size can be maintained by introducing newly-formed small grains by DRX, so the capability of Max*m* SPD to dynamically change the strain rate and maintain the maximum *m* value is still effective. However, for the two-step methods with larger pre-elongation, due to a long time of exposure at the high temperature, the grains have already grown relatively large in the first deformation step. Even by introducing more newly-formed small grains by DRX, the average grain size is still large enough to cause hardening of the material, which can cause the stress to rise until fracture.

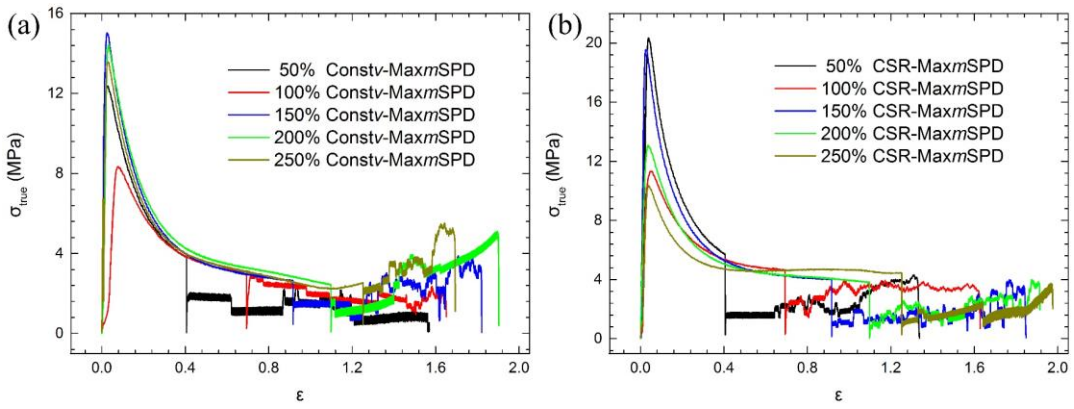

Fig. 4.5 True stress-strain curves of two-step SPD tests by (a) Const*v*-Max*m* SPD and (b) CSR-Max*m* SPD.

Some of the specimens were quenched and collected to observe their microstructures after the first deformation step. Microstructures after the pre-elongation in two-step SPD are shown in **Figs. 4.6 and 4.7**, and the microstructure of the as-extruded material is also included in the figures for comparison. For the as-extruded samples, whose microstructure is shown in **Figs. 4.6 (a) and 4.7 (a)**, it can be observed that there are two phases existing in the alloy: the white portion in the shape of strips of the α phase which is the solid solution of Li in Mg with the HCP structure, and the background matrix of the β phase which is the solid solution of Mg in Li with the BCC structure [36]. The α phase is strip-like and elongated owing to the severe deformation during the extrusion process. The widths of the α phase strips in the as-extruded material are uneven, and the strips are tremendously long. This kind of microstructure of the as-extruded material has been previously found to be not favored by Max*m* SPD.

The microstructures of the specimens after the pre-elongation of stepped SPD by

Const*v* and CSR SPD are summarized in **Figs. 4.6 and 4.7**, respectively. It can be observed that after the first step of deformation, the strips of the α phase gradually disappear and are replaced by finer and equiaxed grains. It has been discussed in Chapter 3 that an equiaxed grain structure is more favored by Max*m* SPD compared to the elongated grains in the as-extruded samples. In the first deformation step by either Const*v* or CSR SPD, strain energy is induced during deformation, which is the source for DRX and transforms the original as-extruded microstructure into a more homogenized and equiaxed grain structure. Therefore, the capacity of the pre-elongation step to break down the elongated grains can lead to a better result in terms of the final elongation. Meanwhile, it can be noticed that the grains in the microstructure become larger as the pre-elongation is increased. As the amount of pre-elongation is increased from 50 to 250 %, the corresponding forming time in the first step is also increased, which in turn enhances the grain coarsening effect.

For the microstructure evolution in the first step of CSR-Max*m* SPD, the α phase grains are gradually transformed to be more equiaxed and the growth of grains is steady with the increase of pre-elongation. In addition, it can be observed that after the pre-elongation of 250 % in CSR-Max*m* SPD, the overall α phase grains are still generally equiaxed, and many newly-emerged little α phase grains can be observed, which is similar to the microstructure after the pre-elongation of 200 % by the same deformation method. However, the evolution of microstructure in the pre-elongation step in Const*v*-Max*m* SPD tends to be different. The α phase grains after the pre-

elongation of 250 % appear to be linked and integrated together, but the grains are more separated when the pre-elongation is 200 %. Meanwhile, for the same pre-elongation of 250 %, the newly-emerged α phase grains by Const*v* SPD is not as much as those by CSR SPD. The reason could be explained as follows. The velocity remains constant in Const*v* SPD but increases in CSR SPD, so CSR SPD has a higher average velocity and shorter forming time is required for forming the same amount of pre-elongation. Therefore, grain growth by CSR SPD is less than that by Const*v* SPD after the same amount of deformation, and CSR SPD is able to prepare finer and more homogenized grain structure for Max*m* SPD in the second deformation step. This phenomenon becomes more obvious when the pre-elongation is larger, because the difference between the average speed of Const*v* and CSR SPD is also more significant. For Const*v*-Max*m* SPD, the largest elongation occurred when the pre-elongation is 200 %, and the pre-elongation of 250 % induced less final elongation. Nonetheless, for CSR-Max*m* SPD, the best result was obtained when the pre-elongation is 250 %. This could be because of the severer grain growth for the pre-elongation of 250 % than 200 % owing to the longer time exposed in the high-temperature environment in Const*v* SPD. Meanwhile, the difference between the forming time of 200 and 250 % pre-elongation in CSR-Max*m* SPD is smaller, so the microstructure can remain equiaxed for CSR-Max*m* SPD with the elongation of 250 %, and a better SPD result can still be attained for the largest pre-elongation of 250 %.

The elongation in the second step of SPD with different amount of pre-elongation and

deformation methods is summarized in **Fig. 4.8**. For Const*v*-Max*m* SPD, the elongation in the second step generally increases as the pre-elongation is increased from 50 to 150 % and remains steady from 150 to 200 % but decreases dramatically as the pre-elongation is larger than 200 %. However, for CSR-Max*m* SPD, the elongation in the second step increases when the pre-elongation is increased from 50 to 150 % but almost remains steady when pre-elongation is larger than 150 %. For the pre-elongation from 50 to 150 %, the second-step elongation of both methods increase, which is in accordance with the grain refinement in **Figs. 4.6 and 4.7**. When the pre-elongation is between 150 and 200 %, it can be observed that the microstructure becomes more equiaxed, while the grains after the first step have grown and more cavities have been formed, which makes the elongation in the second step remain almost the same. However, when the pre-elongation is increased from 200 to 250 %, the microstructure of CSR-Max*m* SPD remains almost the same, while more cavities and linkage of α phase grains can be found in the microstructure after Const*v*-Max*m* SPD, which leads to differences in the trend of the second-step deformation by CSR-Max*m* and Const*v*-Max*m* SPD. It can also be noticed in **Fig. 4.5** that for Const*v*-Max*m* SPD, the stress at the beginning of the second step deformation with 250 % pre-elongation is larger than that with 200 % pre-elongation. Since GBS is the main deformation mechanism for SPD, the larger and more integrated grains in the 250 % pre-elongated sample may hinder the deformation and lead to higher deformation stress and further the smaller final elongation. Nonetheless, the difference between the microstructure of samples with 200 and 250 % pre-elongation by CSR-Max*m* SPD is

not obvious, so the beginning stress of the second step is of almost the same level, which leads to almost the same final elongation in the second deformation step.

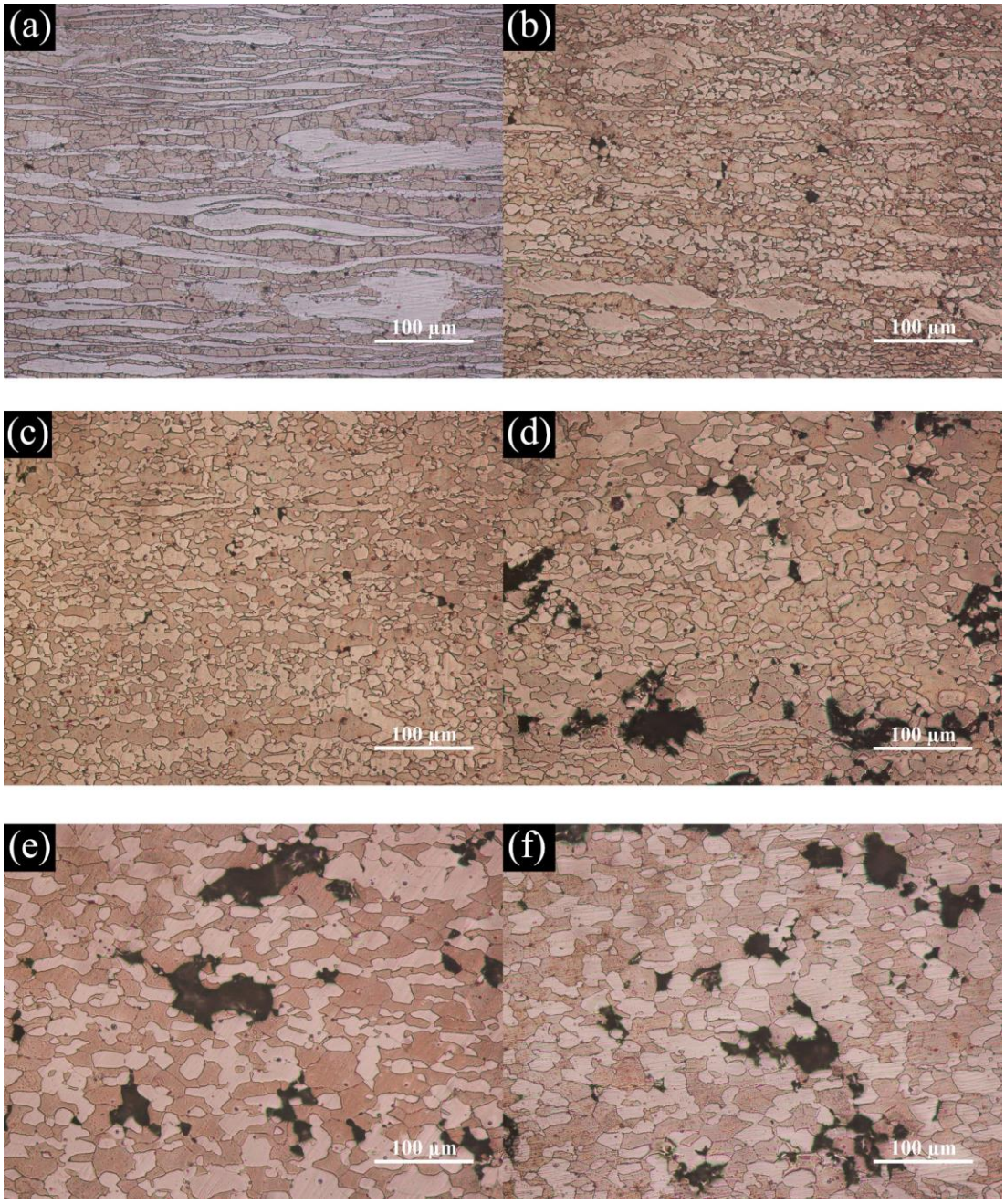

Fig. 4.6 Microstructures of the LA91 specimens with the material states of (a) as-extruded and deformed after the pre-elongation of (b) 50 %, (c) 100 %, (d) 150 %, (e) 200 %, and (f) 250 % in Const*v*-Max*m* SPD.

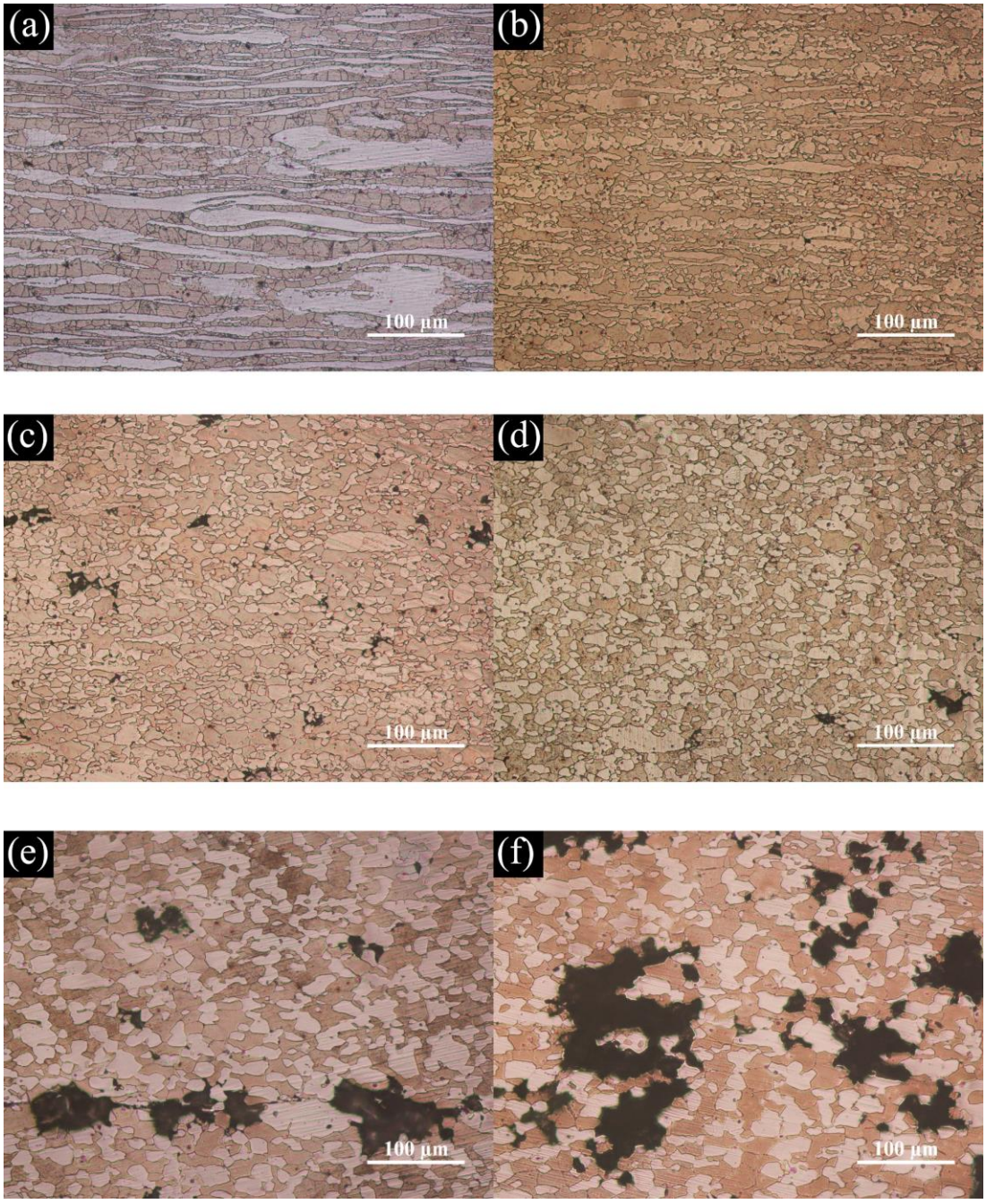

Fig. 4.7 Microstructures of the LA91 specimens with the material states of (a) as-extruded and deformed after the pre-elongation of (b) 50 %, (c) 100 %, (d) 150 %, (e) 200 %, and (f) 250 % in CSR-Max*m* SPD.

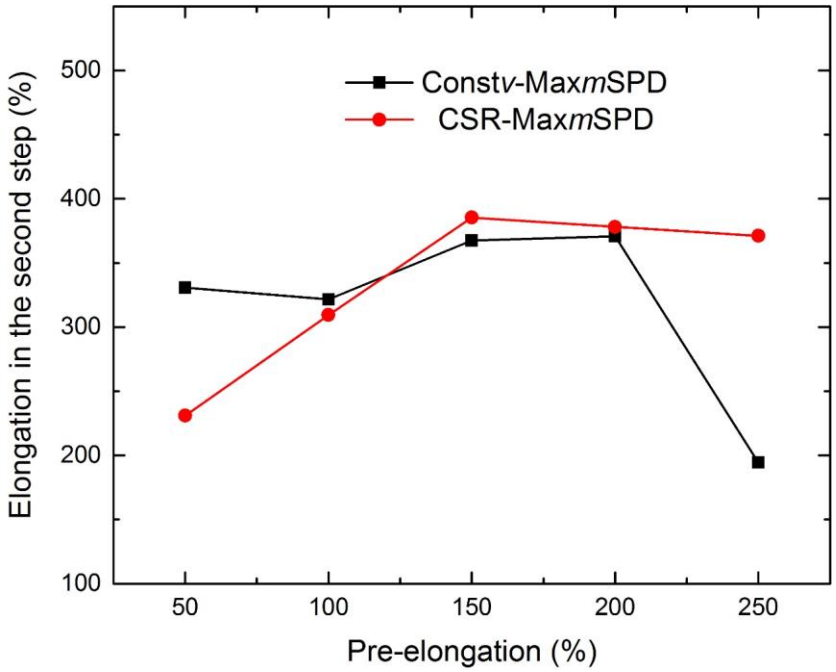

Fig. 4.8 Summary of elongation in the second step by different deformation methods with different pre-elongation.

The technique of electron back scatter diffraction (EBSD) were applied to the as-extruded specimen and specimens deformed after the pre-elongation of 50 and 250 % Const*v* SPD and 50 and 250 % CSR SPD, and the graphs are shown in **Fig. 4.9**. It can be observed that the connected grains of α phase can be clearly distinguished, which is impossible if optical microscopy is applied. However, the β phase is in black color, which indicates that Kikuchi pattern could hardly be indexed in the β phase region due to poor degree of lattice perfection. It was explained by Liu et al. [115] that the low degree of lattice perfection of β phase could be caused by high dislocation density. The deformation is mainly concentrated in the β phase, because the β phase is somehow softer than the α phase. When the amount of pre-elongation is increased from 50 to 250 % for both of the Const*v* and CSR SPD methods, the grain sizes have increased

much. The measured grain sizes in **Fig. 4.9 (b)-(e)** are 6.5, 10.9, 5 and 5.6 μm respectively. The grains in the Const*v* SPD process has increased much, however, the grain size remains almost the same during the CSR SPD process. Meanwhile, misorientation angles of the grain boundaries were also calculated and summarized, as shown in **Fig. 4.9**. It can be observed that the high angle grain boundaries (HAGBs) is decreased with the increase of pre-elongation by Const*v* SPD but is greatly increased with the CSR SPD process. This result only shows the grain boundaries between the α phase, but it can still indicate that the CSR SPD process can induce much more HAGBs, which is more beneficial for dynamic recrystallization in the second step deformation by Max*m* SPD.

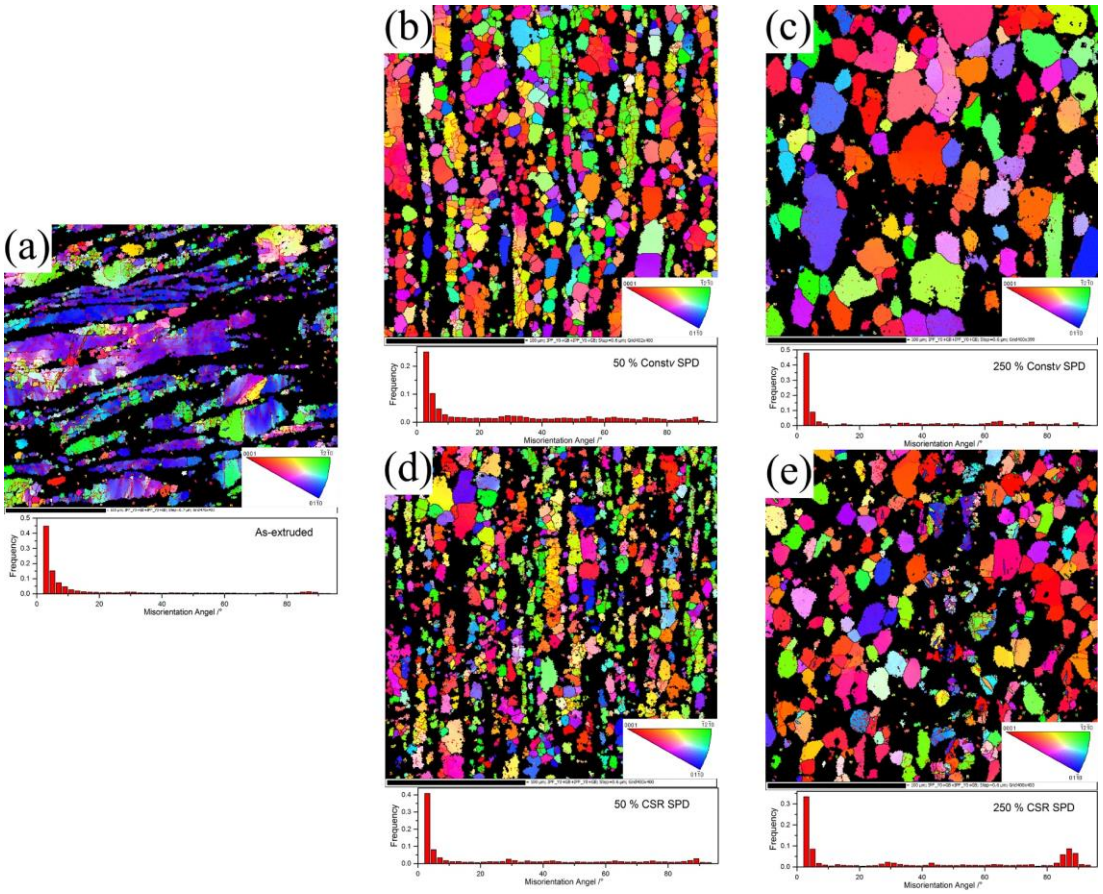

Fig. 4.9 EBSD graph of the specimens with the material states of (a) as-extruded, and deformed after (b) 50 % Const*v* SPD, (c) 250 % Const*v* SPD, (d) 50 % CSR SPD, and (e) 250 % CSR-SPD.

4.3.3 *m* value variation analysis

The strain rate sensitivity (*m* value) is a critical indicator for the SPD state, and in general, a higher *m* value usually indicates a better SPD state. It has been indicated that for the LA91 alloy, the material enters a superplastic state when $m \geq 0.3$ in the previous chapter. In this study, in order to investigate the variation of *m* value during the second step of deformation in Max*m* SPD, the *m* value - true strain curves of the

deformation processes in various conditions are plotted in **Fig. 4.10**. The *m* value is derived by the equations 2-8 and 2-9 with the parameters as shown in **Fig. 2.8**, and an average of every 20 recorded *m* values is used to plot the graph to smoothen the curves. The starting strain of the different curves in **Fig. 4.10** is different because the curves only exhibit the *m* value variation during Max*m* SPD deformation in the second SPD step.

It can be observed that for lower pre-elongation of 50 and 100 %, the fluctuation of *m* value is relatively more stable during the deformation process. However, the curves for the larger pre-elongation of 150, 200 and 250 % show a decreasing tendency, and for the SPD tests which achieved the largest elongation by both Const*v*-Max*m* and CSR-Max*m* SPD, the *m* values at the end of the deformation are also the lowest among experiments with different pre-elongation by the same SPD method. The declining trend of *m* value during the experiments with the pre-elongation larger than 150 % indicates that the best superplastic state is achieved at the beginning of the second SPD step, and the SPD state gradually deteriorates as the material is elongated. This is because when the pre-elongation is larger than 150 %, grains have already grown to be relatively large and some cavities have been formed in the alloy. As the deformation continues, grain growth and cavity formation become severer, so GBS during the SPD process is more hindered which leads to a worse SPD state and further a smaller *m* value. For material which achieved the largest elongation, the time for the material to be held in the high-temperature environment is also the longest, and due to the severest

grain growth and cavity formation, the *m* value is the lowest at the final deformation stage compared to the other amount of pre-elongation. However, for the experiments with less pre-elongation of 50 and 100 %, the *m* value variation trend is steadier in the second step of deformation, which is very similar to that in the single-step Max*m* SPD, as shown in **Fig. 4.10 (c)**. This indicates that lower pre-elongation of 50 and 100 % do not change the material state much in terms of the variation of *m* value, while for larger pre-elongation from 150 to 250 %, the material state becomes worse than the original state and leads to the decrease of *m* value. From **Fig. 4.8**, it can be obtained that the elongation in the second step of deformation generally increases for the pre-elongation from 50 to 150 % but decreases or remains almost the same for the pre-elongation from 150 to 250 % for Const*v*-Max*m* and CSR-Max*m* SPD. By analyzing the *m* value variation, it can be further inferred that owing to the microstructure change for the pre-elongation which is larger than 150 %, the *m* value variation changes from a relatively steady tendency to a decreasing tendency. This is also the reason why the increasing trend for the elongation in the second step is terminated since the pre-elongation of 150 %.

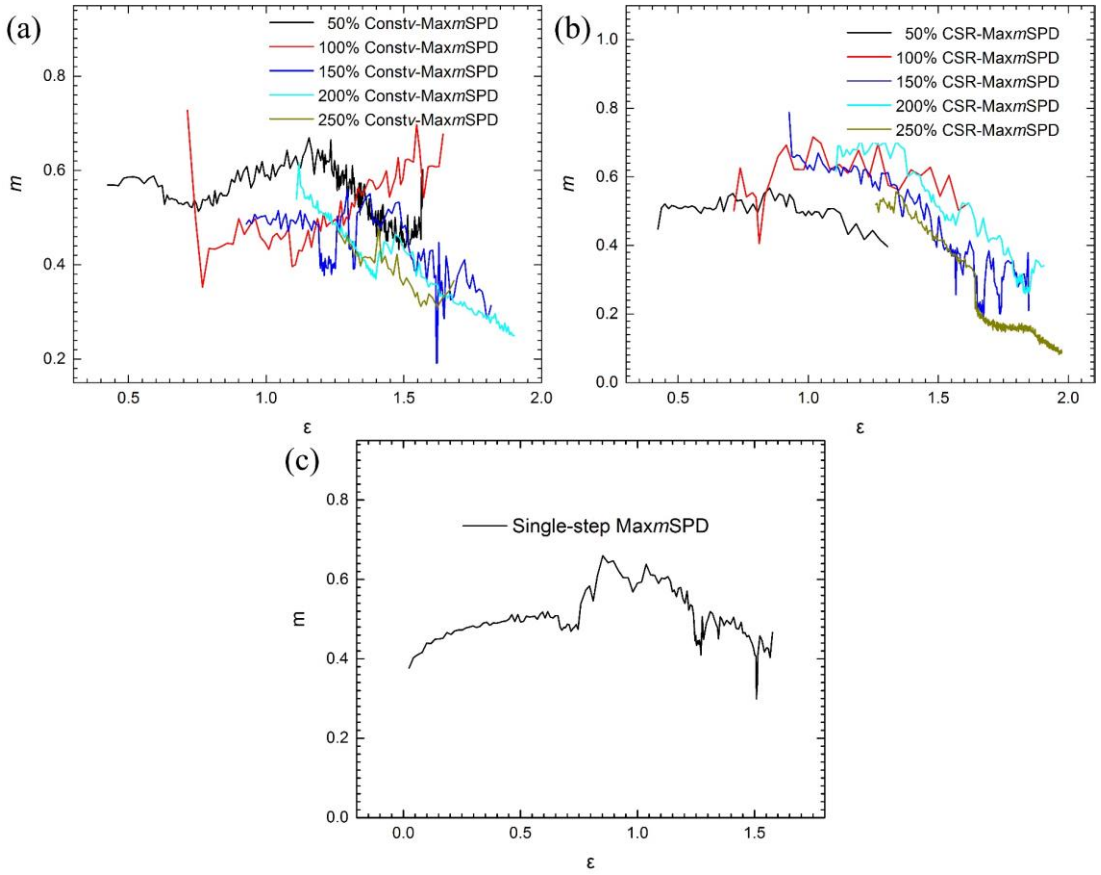

Fig. 4.10 *m* value variation in (a) the second step of Const*v*-Max*m* SPD, (b) the second step of CSR-Max*m* SPD, and (c) single-step Max*m* SPD.

4.3.4 Fracture Mechanisms

The microstructures of the region which is about 6 mm away from the fractured region of specimens after the two-step SPD with the pre-elongation of 50, 200 and 250 % in both Const*v*-Max*m* and CSR-Max*m* SPD are summarized and shown in **Fig. 4.11**. The elongation of 50, 200 and 250 % were selected because they indicated the smallest and largest elongation in the two-step SPD tests. It can be noticed that the microstructure after the second step of SPD is completely different from that after the pre-elongation, and both the α and β phase grains have grown much and more cavities are formed

inside the material. As shown in **Fig. 4.11 (a) and (d)**, for the 50 % pre-elongated specimen which has the smallest final elongation by Const*v*-Max*m* and CSR-Max*m* SPD, the α and β phases are relatively uniformly distributed. However, for the specimens with the pre-elongation of 200 and 250 % which led to the largest two elongation within the same deformation method, the α phase tends to merge and an increased proportion of the α phase can be observed. Meanwhile, for the material which obtained the largest elongation by the same deformation method, viz. 200 % for Const*v*-Max*m* SPD and 250 % for CSR-Max*m* SPD, the proportion of the α phase in the alloy is higher than that in the material which achieved the second largest elongation, viz. 250 % Const*v*-Max*m* SPD and 200 % CSR-Max*m* SPD.

The microstructure of the fracture regions of samples with the largest two final elongation by Const*v*-Max*m* and CSR-Max*m* SPD are shown in **Fig. 4.12**. It can be observed that compared to the microstructure which is 6 mm from the fracture region, the proportion of the α phase in the alloy has risen. Moreover, the proportion of the α phase is still higher for the samples which achieved the largest final elongation among the same deformation method, i.e. 200 % Const*v*-Max*m* SPD and 250 % CSR-Max*m* SPD. It has been found that for the LA91 alloy, stress-induced transformation in which the β phase is transformed into the α phase could occur near the fracture region, because of a higher level of stress suffered near the fracture region. It can therefore be further inferred in this study that when the final elongation is the larger, a higher proportion of the α phase in the alloy can be generated and induced. In addition, it can

be observed in **Figs. 4.11 and 4.12** that the fracture is caused by the coalescence of cavities formed inside the alloy during the SPD process, and the cavities are formed inside the α phase. The α phase which has the HCP structure is more difficult for GBS and easier to fracture than the β phase which has BCC structure, so the β phase tends to be transformed into the α phase such that fractures may occur inside the α phase. More β phase can be transformed into the α phase as larger elongation is obtained, and the final elongation largely depends on how the deformation method can prevent the α phase from cavitation and fracture.

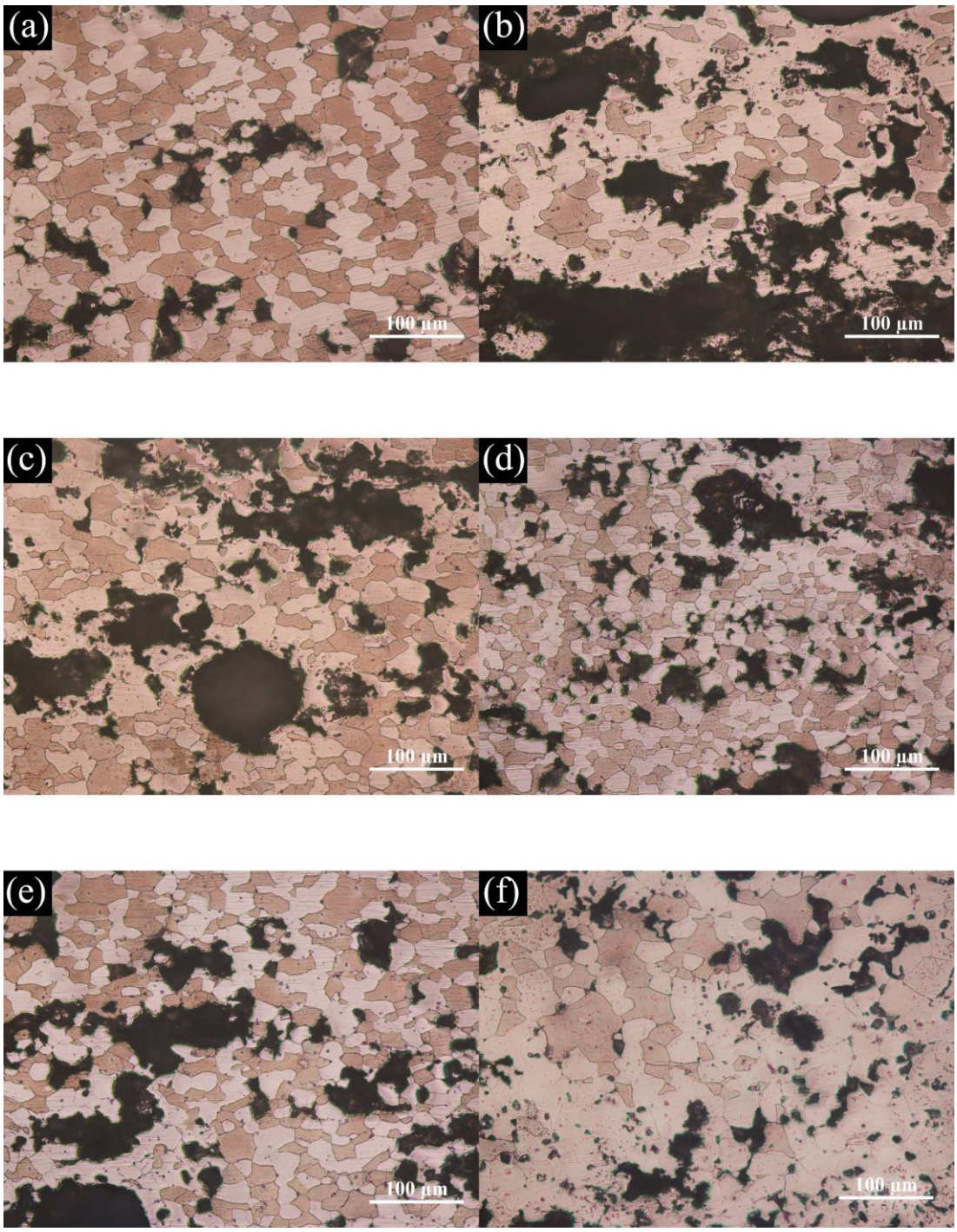

Fig. 4.11 Microstructures which are about 6 mm from the fracture regions of specimens after SPD tensile tests by methods of (a) 50 % Const*v*-Max*m* SPD, (b) 200 % Const*v*-Max*m* SPD, (c) 250 % Const*v*-Max*m* SPD, (d) 50 % CSR-Max*m* SPD, (e) 200 % CSR-Max*m* SPD, and (f) 250 % CSR-Max*m* SPD.

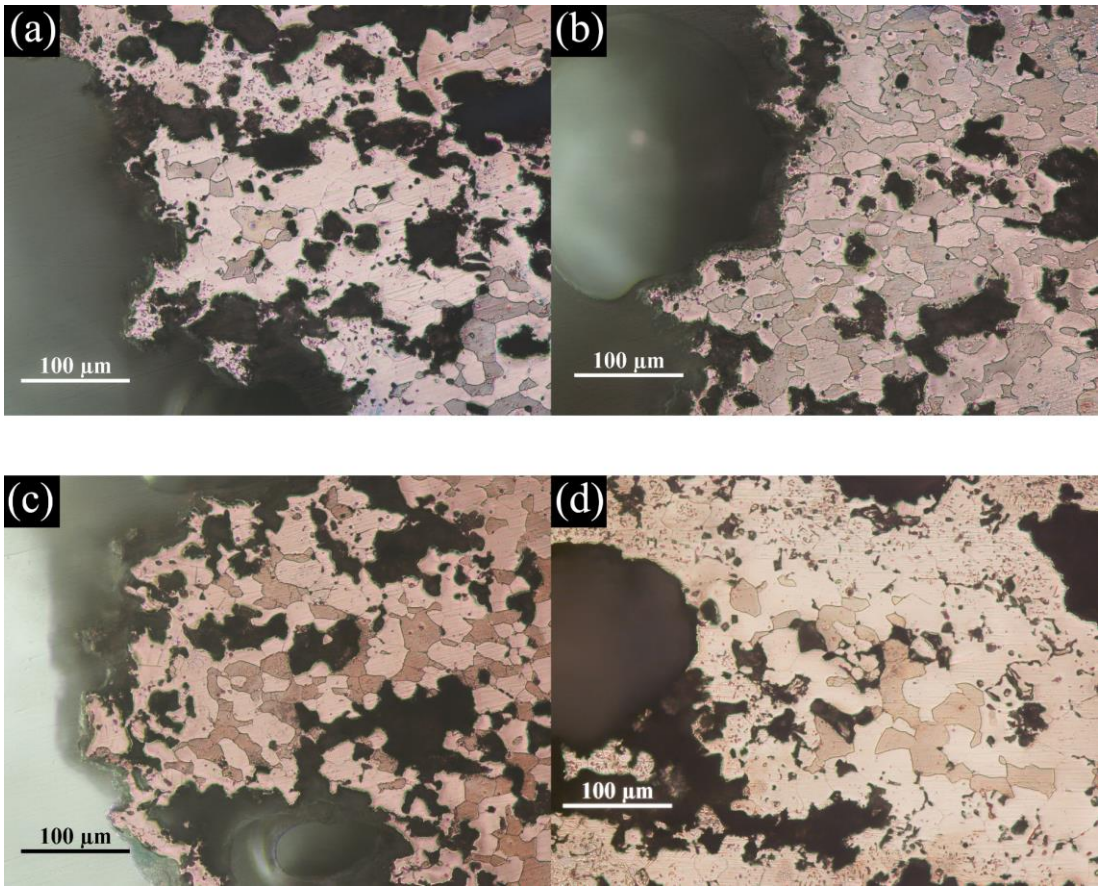

Fig. 4.12 Microstructures of fracture regions of the specimens after SPD tensile tests by methods of (a) 200 % Const*v*-Max*m* SPD, (b) 250 % Const*v*-Max*m* SPD, (c) 200 % CSR-Max*m* SPD, and (d) 250 % CSR-Max*m* SPD.

Fig. 4.13 shows the overall material microstructure which is 6 mm away from the fracture region, and the overall distribution of cavities can be wholly observed. Noticing that proportions of the cavities in different specimens could be different, the porosity in the microstructure was measured. Iimage analyzing software was utilized to count the pixels of cavities and the region of the alloy in the pictures. By dividing these two numbers, the porosity in the area was calculated. The result of the calculated porosity for different specimens is summarized in **Fig. 4.14**. For the formation and

cavity growth during SPD, stress-assisted vacancy diffusion, superplastic diffusion growth, plastic deformation around the cavities and cavity linkage are the main mechanisms [116]. From **Figs. 4.13 and 4.14**, it can be observed that for the specimens which achieved the largest elongation, long and coalesced cavities and the largest holes exist in the microstructure, and the level of porosity is also the highest. In the discussion of *m* value variation, it was found that the *m* value at the end of the SPD which achieved the largest elongation is generally the lowest in the deformation process. The high level of porosity could be one of the reasons for the lowest *m* value because cavities formed in the metal can hinder the GBS and deteriorate the superplasticity. However, the largest elongation can still be achieved when the level *m* value is low. This could be because in the pre-elongation step of the two-step method, the material can be efficiently deformed with relatively high speed and more strain energy can be generated which can facilitate DRX. Although the increased pre-elongation from 150 to 250 % does not further increase the elongation in the second step due to grain growth and cavity formation, the overall elongation has been increased. To sum up, the two-step SPD method can reach a larger elongation because it can postpone the fracture of the material by efficiently obtaining the pre-elongation and providing a better microstructure for the Max*m* SPD in the second step.

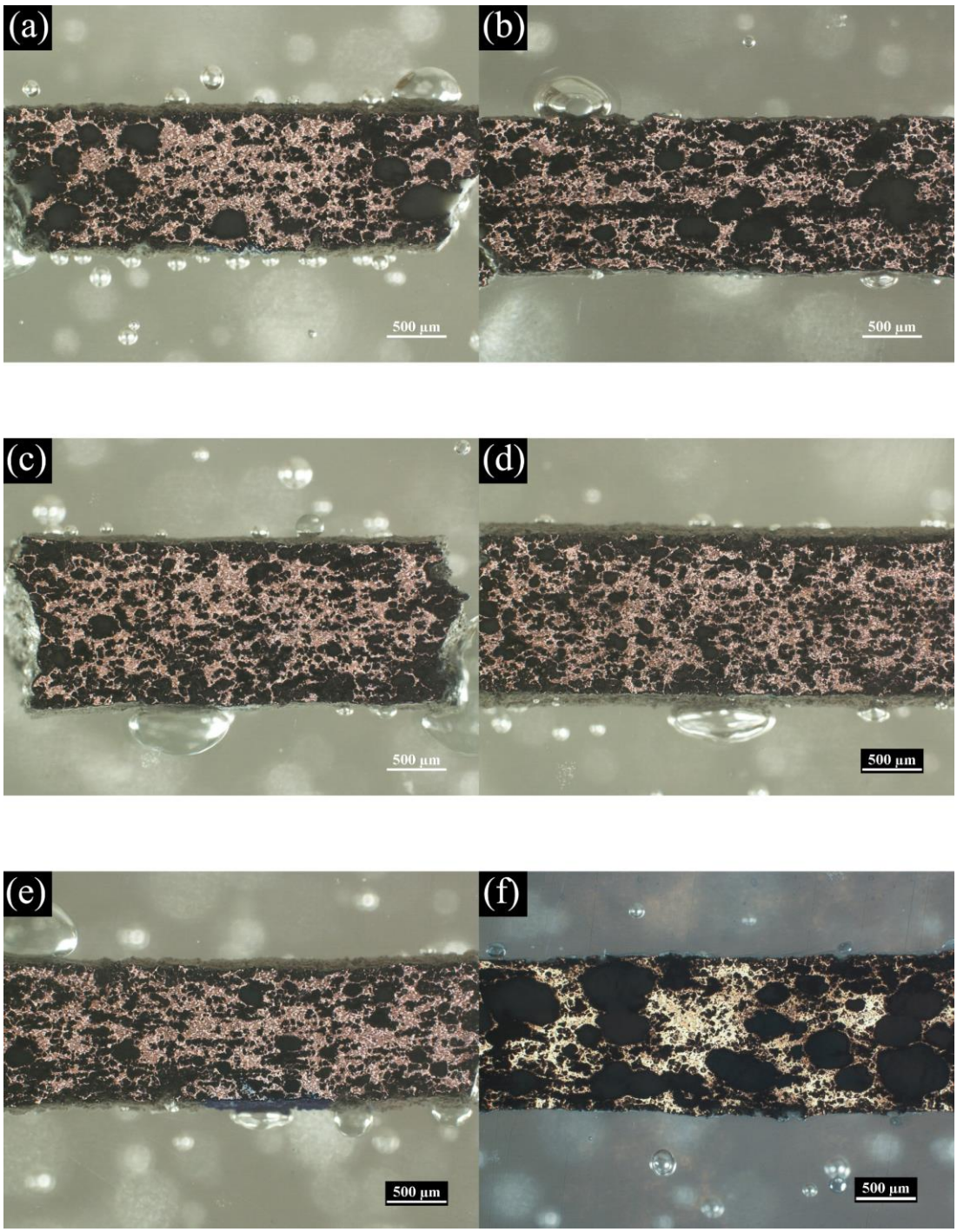

Fig. 4.13 Overall microstructures which are 6 mm from the fracture regions of specimens after SPD tensile tests by methods of (a) 50 % Const*v*-Max*m* SPD, (b) 200 % Const*v*-Max*m* SPD, (c) 250 % Const*v*-Max*m* SPD, (d) 50 % CSR-Max*m* SPD, (e) 200 % CSR-Max*m* SPD, and (f) 250 % CSR-Max*m* SPD.

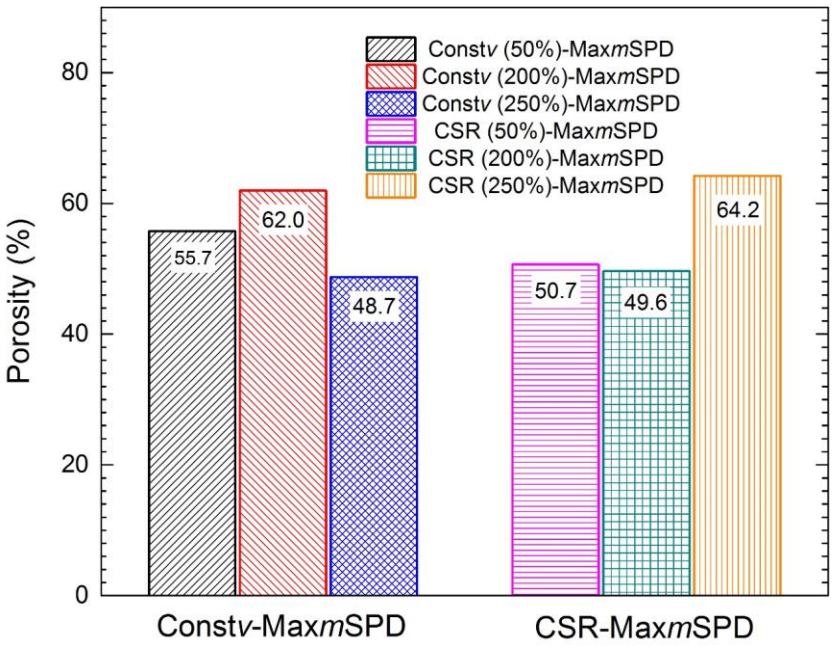

Fig. 4.14 Porosity of the samples in **Fig. 4.13**.

4.4 Conclusions

The two-step SPD approach was applied to the LA91 alloy to investigate its applicability in the hot working of Mg-Li alloys for making complex and integral structures. For this approach, the single-step SPD by Const*v*, CSR and Max*m* SPD were conducted at first to search for the optimum parameters and suitable pre-elongation. The two-step SPD in Const*v*-Max*m* and CSR-Max*m* SPD were then explored. From this research, the following conclusions can be drawn and summarized

.

(1) The largest elongation of 621.1 % was obtained by the as-extruded material in CSR-Max*m* SPD with the pre-elongation of 250 %, which is even larger than the best

result of 563.7 % in the previous research where the further grain-refined material was applied for single-step Max*m* SPD.

(2) The pre-elongation step in the two-step method can gradually change the long α phase grains into a more equiaxed grain structure, and the optimized structure can lead to larger overall elongation.

(3) Generally, CSR SPD is better than Const*v* SPD when used in the pre-elongation step, because of higher average velocity and the lower level of grain growth in the microstructure.

(4) When the pre-elongation is greater than 150 %, the elongation in the second step by Max*m* SPD is not further increased, and the *m* value becomes decreased throughout the second process, which is because the long α phase grains have already been fully transformed into equiaxed grains by DRX, and grain growth becomes dominant when larger pre-elongation is obtained.

(5) For the largest final elongation, the highest proportion of α phase and porosity level can be found in the microstructure of the material. In addition, cavities are mostly generated within the α phase, because the α phase in the HCP structure tends to hinder GBS and be fractured much easier.

Chapter 5 Max*m* SPD of annealed Mg-Li based alloy by a stepped deformation method

5.1 Introduction

In Chapter 4, the stepped SPD method in which the combination of traditional deformation methods of Const*v* or CSR SPD as the first deformation step and Max*m* SPD as the second step was applied to the as-received Mg-Li alloy in the as-extruded state. After the first deformation step, the long strips of α phase grains in the as-extruded material gradually become more equiaxed due to DRX during the SPD process. The equiaxed microstructure is more favored by the Max*m* SPD in the second SPD step such that larger elongation can finally be obtained. Nonetheless, if the material used in SPD has already become more equiaxed without significantly changing the grain sizes in the microstructure by certain means of material treatment, whether the results of single-step or two-step SPD can lead to a larger elongation becomes uncertain, which deserves further investigation.

In this research, for optimizing the grain structure of the LA91 alloy without severely changing the grain sizes, the method of SRX was applied. The SRX can be realized by annealing the specimens at a relatively moderate temperature for a relatively short period. In this way, SRX can occur while grain growth can be controlled. However,

since the annealing process can facilitate recrystallization as well as expending the strain energy accumulated in the alloy during the preparation process of the material, how the annealing process can affect the final SPD results is uncertain. To explore the optimal temperature for annealing, a series of experiments in which specimens were annealed at the temperature from 523 to 623 K for 1 h. The parameters of the annealing temperature of 573 K for 1 h were then selected and applied to all the specimens used in the subsequent SPD experiments. Single-step SPD tests by Const*v*, CSR, and Max*m* SPD were conducted to search for the optimum parameters and deformation limit for the SPD process. The obtained optimal parameters were then applied in the two-step SPD. The longest elongation of 549.3 % occurred by Const*v*-Max*m* SPD with the pre-elongation of 50 %, and it has been be indicated that the annealing process is not feasible for enhancing the stepped superplasticity. The microstructure evolution, deformation behavior, and fracture mechanisms of the stepped SPD with annealed LA91 alloy are studied and compared with the results obtained by the as-received materials in Chapter 4.

5.2 Experimental procedures

5.2.1 Material Preparation

The as-received material in this study is the LA91 alloy in the as-extruded state, which is the same as the as-received state in Chapters 3 and 4. ICP was employed and confirmed that the alloy contains 8.829 % Li and 1.063 % Al (in wt %), which is nearly

identical to the theoretical alloy composition.

In this research, the annealed alloy was utilized in the SPD tests. The optimum annealing temperature was explored by conducting a series of heat treatment experiments at the temperatures from 523 to 623 K for 1 h and identifying the optimal microstructure obtained from different temperatures. The temperature of 573 K and holding time of 1 h were then selected as the optimal heat treatment process parameters, and the as-received materials were annealed with such parameters. The specimens for SPD tensile tests were then fabricated by machining the alloy rods into the dog-bone shape with the gauge length of 15 mm and gauge diameter of 3 mm, and the length direction is parallel to the extrusion direction.

5.2.2 SPD tensile tests

In this research, the innovative stepped SPD was adopted. The specimens were initially installed onto the tensile tester in the furnace at 573 K and held for 10 min. In the first step, the specimens were deformed via Const*v* and CSR SPD with the pre-elongation from 50 to 150 %. A clearance stage of 10 min was then applied, after which the second deformation step started, and the specimens were deformed by Max*m* SPD until fracture. The samples were quenched at the end of the tests to keep the microstructure at the working temperature. The Max*m* SPD was adopted in the second deformation step because it can facilitate the material to maintain the optimal

superplastic state until fracture, and better results can thus be obtained.

Single-step SPD tensile tests were conducted to explore the optimal parameters in different methods. For the Const*v* SPD, the velocities of 0.195, 0.39, and 0.78 mm/s (the corresponding initial strain rates are 0.00025, 0.0005, and 0.001 /s) were selected to search for the optimal speed. For the CSR SPD, the strain rates of 0.00025, 0.0005, and 0.001 /s were chosen as the potential parameters. For the Max*m* SPD, the initial velocity v_0 = 0.07 mm/min and velocity increment Δv = 0.03 mm/min were selected, which is identical to the parameters of Max*m* SPD in the previous chapter. After comparing the single-step SPD results, it was concluded that the velocity of 0.39 mm/s for Const*v* SPD and the strain rate of 0.00025 /s for CSR SPD are the optimum parameters for the first step deformation.

In order to study the microstructure evolution during the first deformation step, a series of experiments were conducted by interrupting the experiments and collecting the specimens after the first step with the pre-elongation of 50 to 150 %. The microstructures of the specimens were then prepared.

5.2.3 Preparation of microstructure of specimens

The microstructures of the specimens were prepared and observed by the same method used in Chapter 3.

5.3 Results and discussion

5.3.1 Exploration of optimal annealing parameters

The optimum temperature for annealing the alloy was confirmed before the implementation of the SPD tests. The α phase in the as-received material is in the shape of strips as shown in **Fig. 5.1 (a)**. It has been proved in the previous chapter that such a structure is not favored by Max*m* SPD, and the microstructure which tends to be more equiaxed is more preferable. The purpose of annealing in this study is to induce SRX to the material such that the α phase strips can be transformed into more equiaxed grains and further facilitating GBS during SPD. Meanwhile, the grain size of the material cannot grow too much, because smaller grains are favored by SPD. Therefore, the annealing temperature should be moderately higher than the recrystallization temperature of the alloy. The starting temperature of recrystallization can be estimated as 0.4-0.5 T_m, and the T_m of 588 °C can be obtained from the alloy phase diagram in **Fig. 2.1**. The estimated starting temperature of recrystallization is around 430 K, and the temperature should be higher than this value. The proposed annealing temperature were thus selected as 523, 573 and 623 K with the annealing time of 1 h.

The microstructures of the as-received and annealed materials are shown in **Fig. 5.1**. Since LA91 alloy consists of two phases, the sizes of the phases were measured separately. The α phase is in the shape of strips and was measured by the α strip width.

The β phase size was determined using the linear interception method with the standard of ASTM-E112. From **Fig. 5.1**, it can be learnt that the grain sizes of alloy annealed at 523 and 573 K are nearly the same as those in the as-extruded state, while the grain sizes of the 623 K-annealed material are enlarged by over 50 % compared to the as-extruded state. Meanwhile, for the 573 K-annealed alloy, it can be observed that the strip-shaped α phase is broken down into shorter strips and more equiaxed grains due to recrystallization at a high temperature can be observed. Such a phenomenon is more obvious in the microstructure of the 623 K-annealed alloy due to the higher temperature. However, owing to the overlarge grain size of 623 K annealed alloy, its superplasticity may be compromised. Therefore, the 573 K annealing temperature and the holding time of 1 h were selected as the heat treatment parameters for the as-received material.

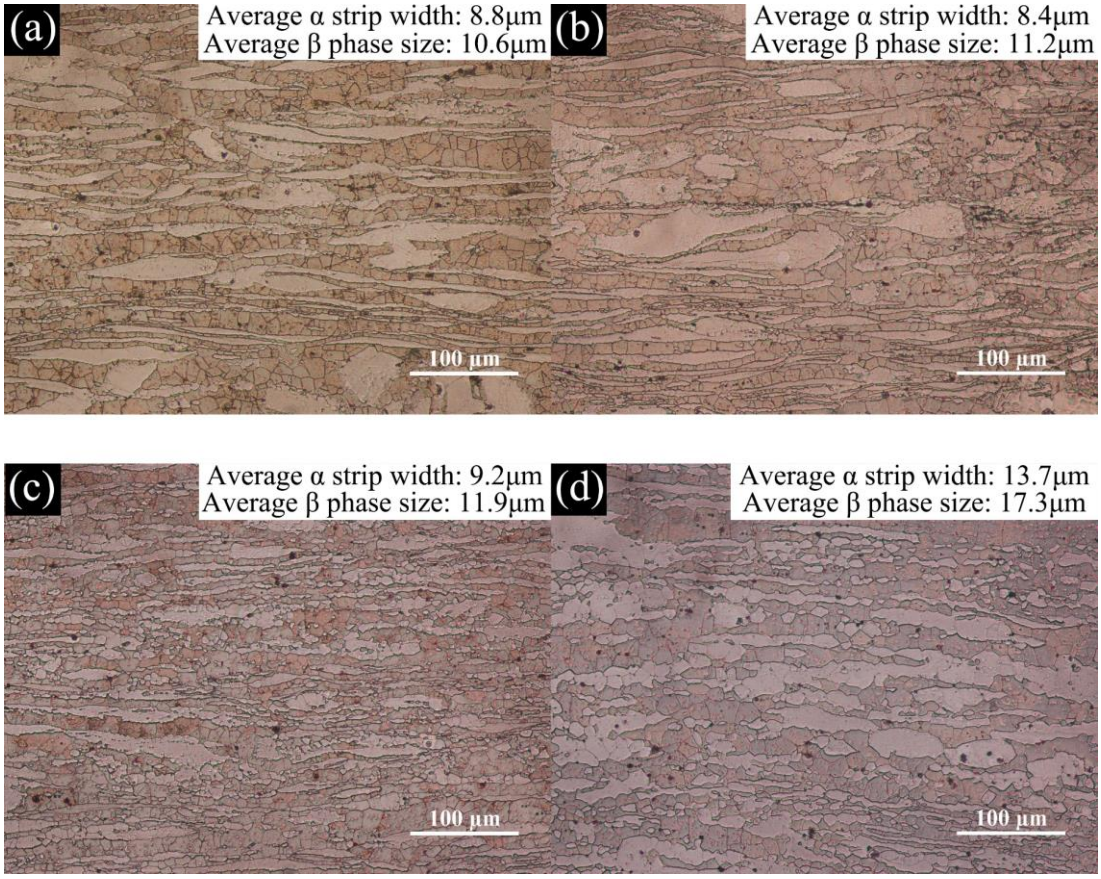

Fig. 5.1 Alloy microstructures in different heat treatment processes: (a) as-extruded, (b) annealed at 523 K for 1 h, (c) annealed at 573 K for 1 h, (d) annealed at 623 K for 1 h.

5.3.2 Single-step SPD experiments

The single-step SPD tensile tests were conducted by using Const*v*, CSR, and Max*m* SPD as the preliminary research to search for the optimal parameters. The parameter setting for the SPD methods is the same as Chapter 4. The velocities of 0.195, 0.39 and 0.78 mm/min and the strain rates of 0.00025, 0.0005 and 0.001 /s were used for Const*v* and CSR SPD, respectively, and the initial velocity v_0 = 0.07 mm/min, velocity increment Δv = 0.03 mm/min and time increment t = 6 s were adopted for Max*m* SPD.

The summary of elongation achieved by the single-step SPD tests with various parameters is shown in **Fig. 5.2**. The elongation in Const*v* and CSR SPD both shows a decreasing tendency with the increase of deformation speed or strain rate, which is similar to the results obtained by the alloys without the annealing treatment in Chapter 4. For the tests with high velocity or strain rate, due to the relatively short deformation time, enough DRX for the material cannot be guaranteed and large elongation cannot be achieved. For Const*v* SPD, the elongation induced by the lowest two velocities of 0.195 and 0.39 mm/s are similar, which is similar to the results in Chapter 4. However, for the annealed Mg-Li alloy deformed by CSR SPD, the elongation induced by strain rate of 0.0005 /s is far less than that by the strain rate of 0.00025 /s, while for the unannealed alloy used in Chapter 4, the results are similar. This difference could result from the recrystallization induced during the annealing process. The extrusion process had induced much strain energy in the alloy and provided a great number of sites of nucleation for the occurrence of recrystallization, but the strain energy was expended during the annealing process to transform the long strips of α phase into grains with the more equiaxed shape. Therefore, in order to induce more DRX to facilitate GBS during the SPD process, the deformation time should be long enough for the recrystallization to occur, which requires a relatively lower average deformation speed. Meanwhile, since the level of strain energy in the annealed alloy is less than that in the as-extruded material in Chapter 4, the influence of average speed on the final elongation should be greater especially for CSR SPD. Because the speed keeps increasing in CSR SPD but remains constant in Const*v* SPD, and the difference in

average speed in CSR SPD is larger than that in Const*v* SPD, which could be the reason why the elongation results of the annealed material in this chapter and the unannealed material in Chapter 4 for the single-step SPD are different by CSR SPD but similar by Const*v* SPD. Meanwhile, by comparing **Figs. 4.1 and 5.2**, it can be noticed that the ductility of Max*m* SPD with the annealed alloy is much worse than the material without annealing. This could also be caused by the reduction of strain energy in the alloy, which indicates that the annealed material is not favored by the single-step Max*m* SPD.

Since the elongation obtained by the lowest two velocities of 0.195 and 0.39 mm/s in Const*v* SPD are almost the same, the velocity of 0.39 mm/s was selected for further exploration. However, due to the much larger elongation induced by the strain rate of 0.00025 /s than 0.0005 /s, the strain rate of 0.00025 /s was chosen for CSR SPD in the two-step experiments.

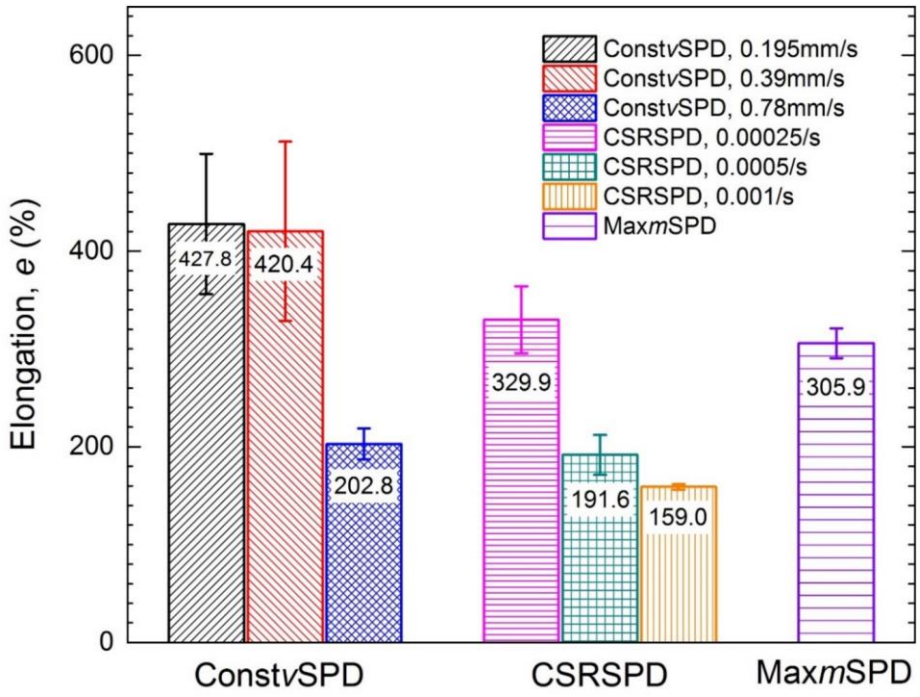

Fig. 5.2 Experimental results of single-step SPD tests by annealed specimens.

Fig. 5.3 shows the fractured specimens after the SPD tests, and the corresponding true stress-strain curves are presented in **Fig. 5.4**. Diffusional necking can be found throughout the gauge part of the specimen. Among the three specimens deformed by different methods, the elongation of the specimen by Const*v* SPD is the largest, followed by CSR and Max*m* SPD. For the annealed material, the superplasticity induced by Const*v* SPD is better than CSR SPD, because the speed in CSR SPD keeps increasing to maintain the strain rate and the average speed in CSR SPD is much higher than Const*v* SPD. For the annealed material, more deformation time is needed for the recrystallization due to the depletion of strain energy during the annealing process, therefore, for the same initial speed, the result of Const*v* SPD is better than CSR SPD. Meanwhile, Max*m* SPD induced the shortest elongation, which indicates that the Max*m* SPD is more sensitive to the decrease of strain energy. The stress-strain curves

of the single-step SPD are shown in **Fig. 5.4**, which is similar to the characteristics of the single-step deformation of the as-received material shown in **Fig. 4.3**. To avoid the redundant discussion on the same topic, the discussion of the deformation behavior and mechanisms in terms of the softening mechanism of DRX and hardening mechanisms of dislocation and grain coarsening can be referred to Chapter 4.

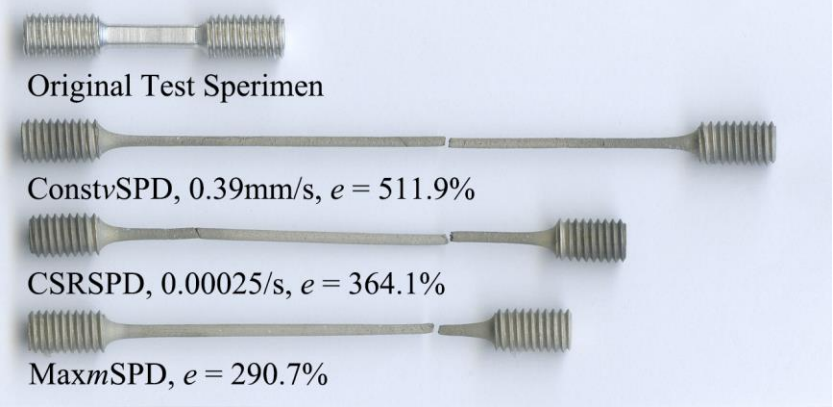

Fig. 5.3 Specimens after single-step tensile tests by various SPD methods.

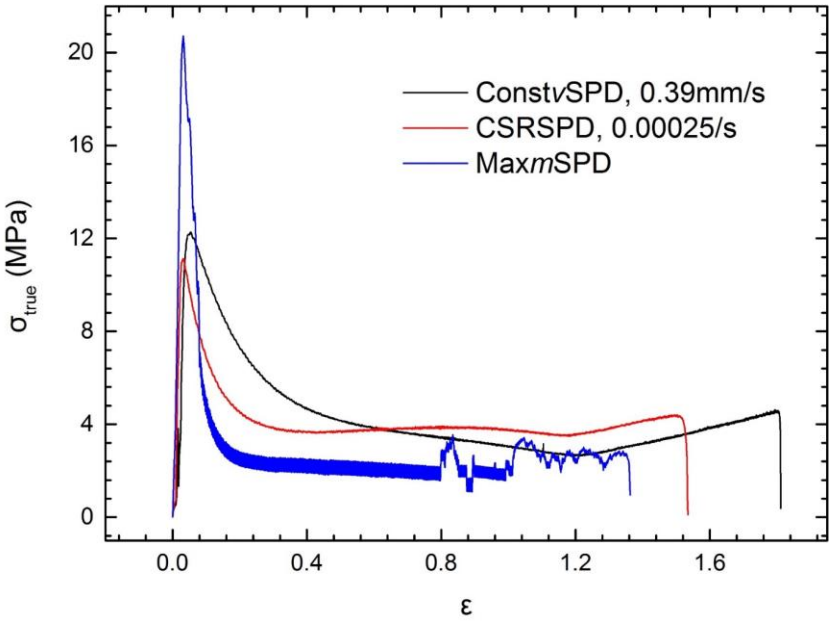

Fig. 5.4 True stress-strain curves of single-step SPD tests by using annealed specimens.

5.3.3 Two-step SPD experiments

The two-step SPD experiments of Const*v*-Max*m* and CSR-Max*m* SPD methods were conducted using the optimal parameters obtained in single-step SPD experiments, viz., the velocity of 0.39 mm/s for Const*v* SPD and the strain rate of 0.00025 /s for CSR SPD. The initial velocity v_0 = 0.07 mm/min, velocity increment Δv = 0.03 mm/min and time increment t = 6 s were applied for Max*m* SPD. The fractured specimens after the SPD tensile tests are shown in **Fig. 5.5**. The result is different from the experiments by using the unannealed materials. For the Const*v*-Max*m* SPD, the elongation shows a decreasing tendency with the increase of the amount of pre-elongation from 50 to 150 %; while for the CSR-Max*m* SPD process, the elongation remains almost the same when the pre-elongation is increased from 50 to 150 %. By comparing **Figs. 5.5 and 4.4**, it can be noticed that when the amount of pre-elongation is 50 %, the annealed material generally demonstrates larger elongation than the unannealed alloy, but when the pre-elongation is larger than 50 %, the final elongation of the as-received alloy become larger than the result of the anneal alloys. This indicates that the process of annealing is beneficial for the two-step processes with small pre-elongation but is detrimental to the deformation processes with larger pre-elongation.

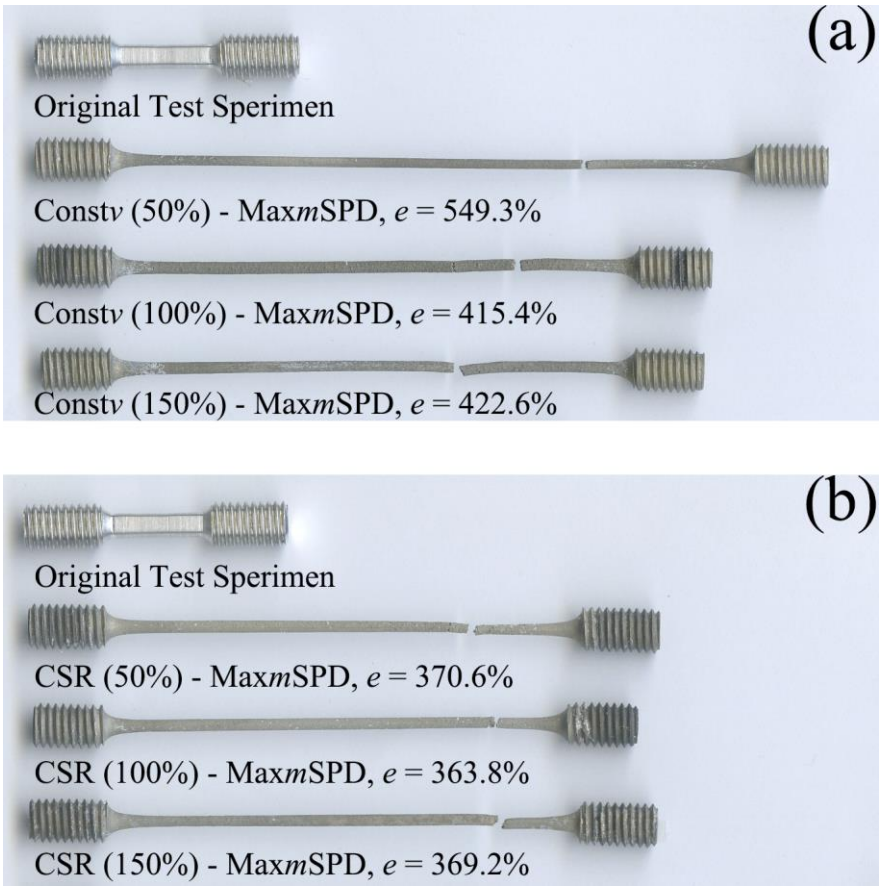

Fig. 5.5 Specimens after two-step tensile tests by various SPD methods.

The true stress-strain curves of the two-step SPD tests of annealed specimens are shown in **Fig. 5.6**. The curves are combined by the first step of Const*v* or CSR SPD and the second-step of Max*m* SPD. These stress-strain curves are very similar to the two-step curves in Chapter 4. However, except for the CSR-Max*m* SPD with 50 % elongation in the first step which exhibits a steadier stress fluctuation in the second step, for both the Const*v*-Max*m* and CSR-Max*m* SPD curves, the stress in the second deformation step exhibits a rising trend. However, for the specimens in Chapter 4, this increasing tendency in the second step is observed when the pre-elongation is larger than 150 %. It has been discussed in Chapter 4 that the increasing stress in the second

deformation step could be attributed to grain growth which hinders the GBS mechanism and causes the hardening effect. For the annealed materials, a portion of the strain energy generated during extrusion which is the driving force for recrystallization has already been consumed during annealing. Therefore, for the second deformation step, the effect of recrystallization is reduced, which makes the effect of grain growth become more obvious and lead to the increasing trend of stress in the second step with a smaller pre-elongation. For the CSR-Max*m* SPD process with 50 % pre-elongation, the forming time is shorter compared to other deformation processes, so the grain coarsening effect is not obvious, which leads to the steadier stress in the deformation second step.

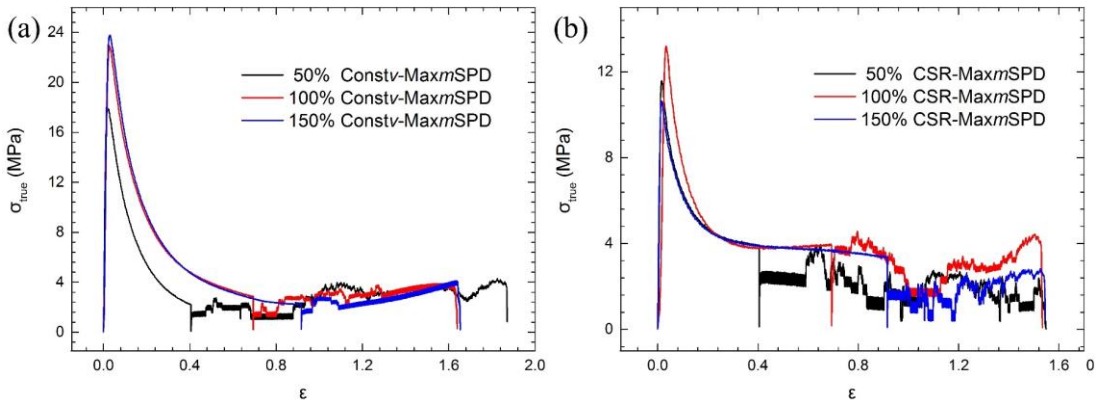

Fig. 5.6 True stress-strain curves of two-step SPD tests by using annealed specimens.

Some specimens were collected after the pre-elongation step to observe the microstructures during the deformation process. The microstructures after the first step are summarized in **Figs. 5.7 and 5.8**. As the difference between the β phase in different materials is not as obvious as the α phase, only the α phase is used for comparison and

discussion. Compared to the microstructure after the pre-elongation, the grains in the undeformed material which can be found in **Fig. 5.1 (c)** appears to be smaller and denser. For the specimens processed by Const*v*-Max*m* SPD as shown in **Fig. 5.7**, after the pre-elongation of 50 %, the α phase grains have grown. In **Fig. 5.7 (a)**, it can be noticed that the elongated grains have been broken down into a series of small grains after annealing, while in **Fig. 5.7 (b)**, these small grains have become larger and more separated. As the pre-elongation rises from 50 to 200 % as shown in **Figs. 5.7 (b) to (e)**, it can be observed that these α phase grains have become more separated and enlarged and the microstructure has become more equiaxed. However, newly-formed recrystallized grains can barely be found in these figures, while in **Figs. 4.6 and 4.7**, it can be found that the newly-emerged α phase grains are mainly generated by recrystallization because small new grains can still be found in the material when the pre-elongation becomes larger. For the CSR-Max*m* SPD process, although some small grains can be found in the material after a large amount of pre-elongation, the α phase grains have grown very large and even become connected to each other. Reduction of recrystallized grains and severer grain coarsening effect may lead to the incapability of Max*m* SPD in the second step to maximize the final elongation, and the final SPD results are compromised with the increase of pre-elongation. Therefore, the Const*v*-Max*m* SPD method is more feasible for the annealed alloys than the CSR-Max*m* SPD method.

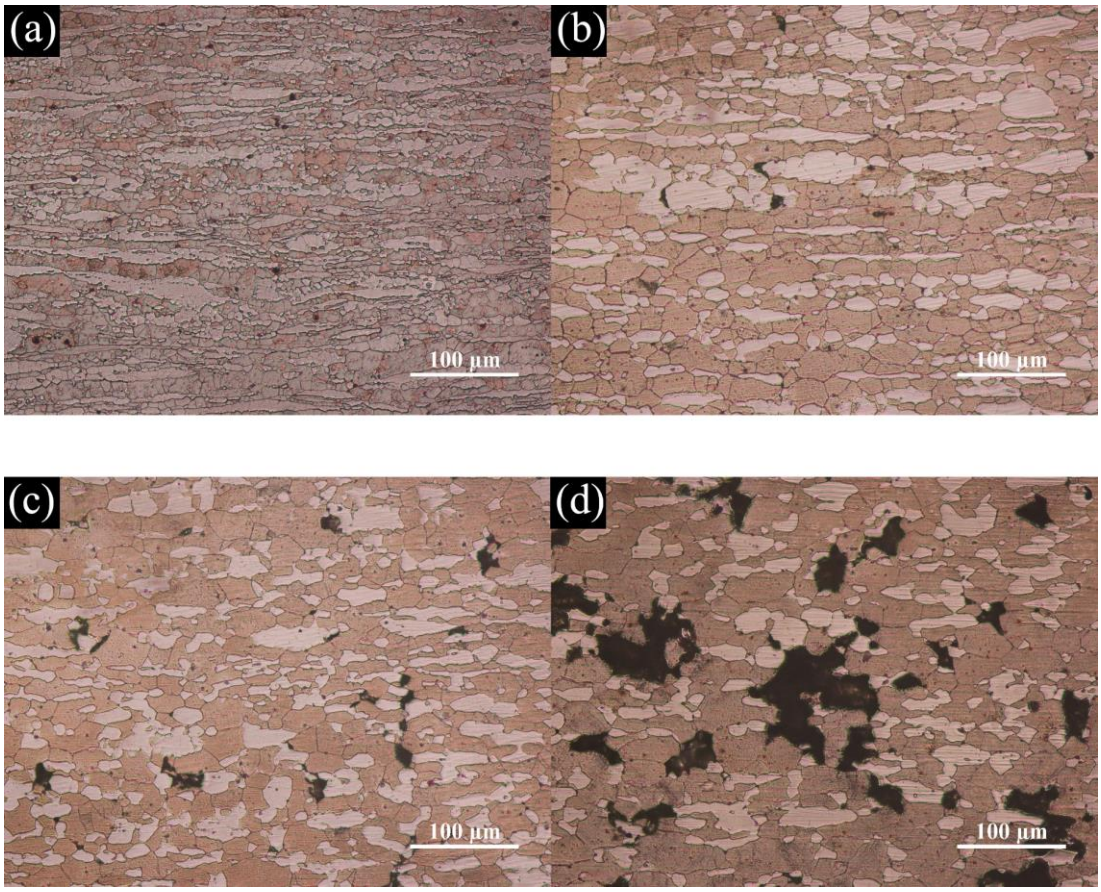

Fig. 5.7 Microstructures of annealed LA91 specimens with the material states of (a) as-extruded after annealing and deformed after the pre-elongation of (b) 50 %, (c) 100 %, (d) 150 % in Const*v*-Max*m* SPD.

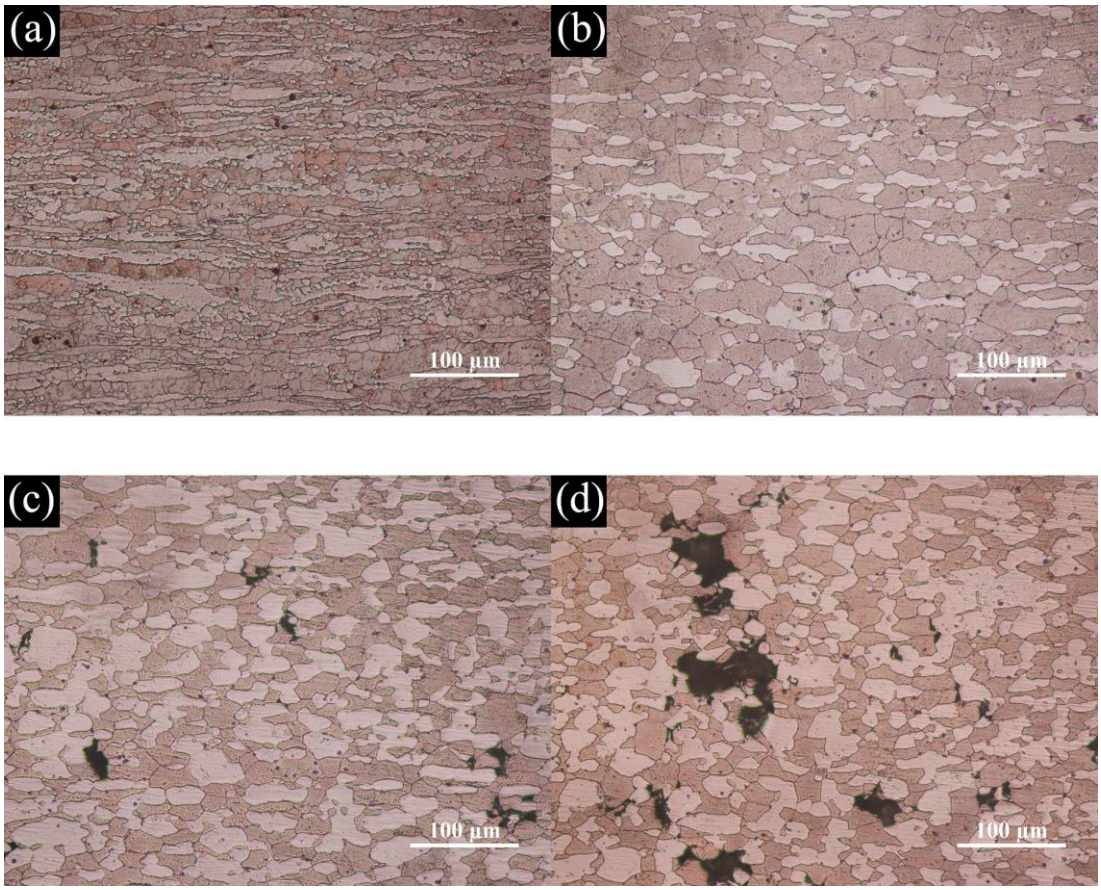

Fig. 5.8 Microstructures of annealed LA91 specimens with the material states of (a) as-extruded after annealing and deformed after the pre-elongation of (b) 50 %, (c) 100 %, (d) 150 % in CSR-Max*m* SPD.

In **Fig. 5.9**, the elongation in the second deformation step with different pre-elongation by using different deformation methods are summarized. It can be noticed in this figure that as the pre-elongation is increased from 50 to 150 %, the second-step elongation keeps decreasing. This finding is in accordance with the microstructure evolution with the increasing pre-elongation. Due to the depletion of strain energy during the annealing process, the newly-emerged recrystallized grains are harder to form than the unannealed material. The hardening mechanism of grain coarsening

becomes severe and the GBS mechanism is hindered, which is detrimental to Max*m* SPD in the second step. With the increase of pre-elongation, the grains grow larger and the grain structure becomes more unfavored by the Max*m* SPD, which could lead to the decrease of elongation in the second step. Meanwhile, it can be noticed that for the same pre-elongation, the elongation in the second step is larger for Const*v* SPD than CSR SPD. The first deformation step provides increased internal strain for the material which facilitates the recrystallization and homogenizes the microstructure. It has been discussed from **Figs. 5.7 and 5.8** that the method of Const*v* SPD has lower average velocity and longer deformation time compared to the CSR SPD, which is more favored by the recrystallization mechanism, especially for the annealed materials whose strain energy has been consumed during annealing. Therefore, the more preferred microstructure can lead to a larger elongation for the Const*v*-Max*m* SPD method.

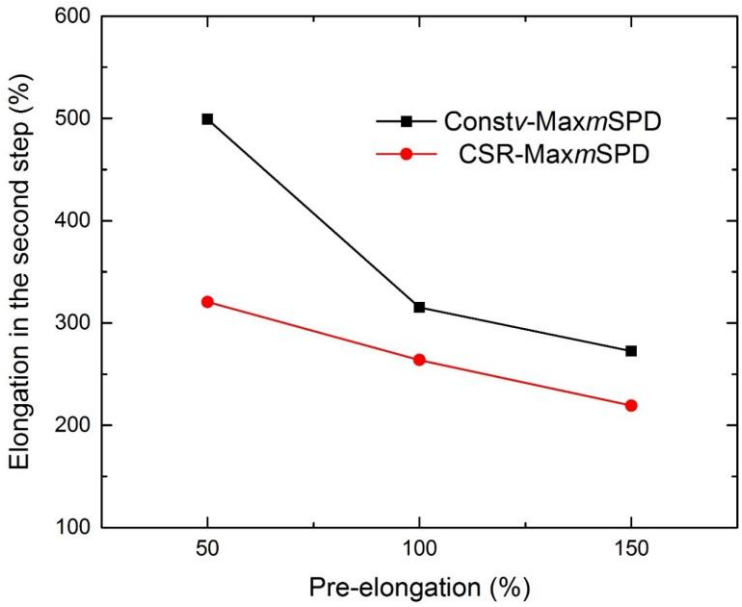

Fig. 5.9 Summary of elongation in the second step by using different deformation methods and annealed materials with various pre-elongation.

5.3.4 *m* value analysis

The strain rate sensitivity (*m* value) usually indicates the capability of the material to resist necking during the SPD process and is a critical indicator for the superplastic state. In general, a better SPD state always corresponds to a higher *m* value. In order to study the influence of the annealing process on the superplasticity of the Mg-Li alloy, the variation of *m* value in the Max*m* SPD step is summarized and studied. The *m* value variation in the second step is shown in **Fig. 5.10**, and the *m* value is calculated by the equations 2-8 and 2-9. The meaning of the parameters can be referred to **Fig. 2.8**. Meanwhile, since the *m* value keeps fluctuating due to the dynamic control of strain rate, an average of every 20 data points was calculated and used to plot the graph. Because the horizontal axis of the graph is true strain, the curves start after the pre-elongation step and the starting point of each curve is different.

From **Fig. 5.10**, it can be observed that for Const*v*-Max*m* SPD, the 50 % pre-elongation can induce a steadier variation trend by Max*m* SPD, but the pre-elongation which are larger than 50 % exhibit a decreasing trend of *m* value in the second deformation step. Meanwhile, for the CSR-Max*m* SPD, it shows a similar variation pattern as the Const*v*-Max*m* SPD, but the decreasing tendency of *m* value for 100 and 150 % pre-elongated samples is not obvious. It has been discussed in Chapter 4 that the steadiness or decrease of *m* value indicates the change of microstructure. For the steady tendency of the *m* value, the variation is very like the single-step Max*m* SPD,

and the elongation in the second step increases with the pre-elongation. However, for the decreasing *m* value, it indicates that the grain structure becomes unpreferable by the Max*m* SPD, so the second-step elongation begins to decrease. This finding is still valid for the annealed material. However, for the unannealed alloy, the final elongation keeps increasing with the pre-elongation, while for the annealed alloy, the final elongation becomes decreased with the increase of pre-elongation. This could also be related to the consumed strain energy in the annealing process. Due to the depletion of strain energy, the DRX is attenuated, and the superplastic state of the material becomes worse more quickly than the as-extruded material, which leads to the reduction in the overall elongation.

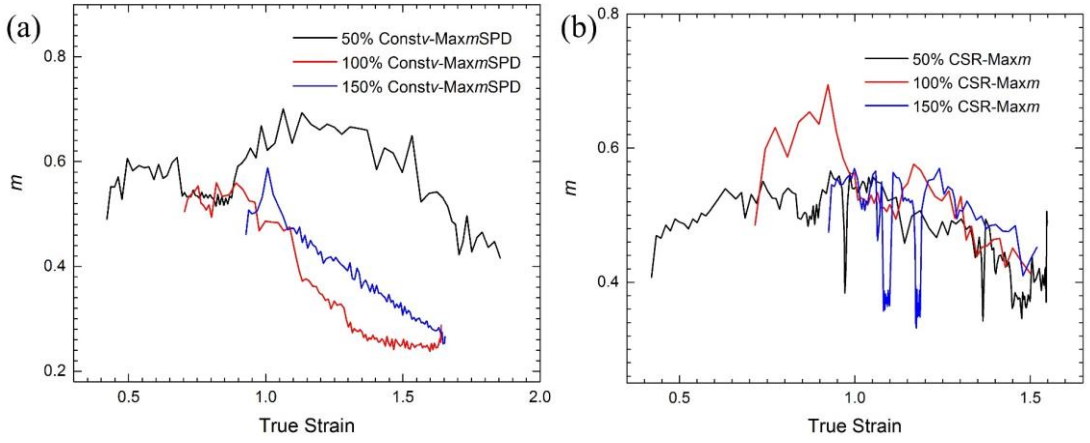

Fig. 5.10 *m* value variation in (a) the second step of Const*v*-Max*m* SPD, (b) the second step of CSR-Max*m* SPD by annealed specimens.

5.3.5 Microstructure evolution during the SPD process

Microstructures of different portions of the specimens by different pre-elongation and deformation methods are summarized in **Fig. 5.11**. Since the gripper part is undeformed during the SPD process, its microstructure evolution demonstrates the effect of annealing during the deformation process. Meanwhile, the microstructure obtained from the area which is 6 mm from the fracture region can represent the microstructure in the gauge part, because 6 mm is relatively far from the fracture region. Furthermore, the fracture region shows how fracture occurs and facilitate the analysis of the fracture mechanism. By the summary of microstructure evolution, the whole picture of the microstructure change during deformation can be exhibited and analyzed.

For the gripper part, it can be found that the grains have grown very large compared to the undeformed material as shown in **Fig. 5.7 (a)** and the material after the first deformation step as shown in **Figs. 5.7 and 5.8**. The connected small α phase grains are still linked, which is different from the microstructure after deformation, in which the α phase grains are separated and deformed. The microstructure in the gripper part is similar to the material which has gone through further annealing process at the temperature of 573 K. Therefore, if the annealing time of the LA91 alloy is longer than 1 h, the grains will be further enlarged, but the recrystallized grains will not continue to emerge, and the elongated grains cannot be further broken down into small grains.

The area which is 6 mm from the fracture region as well as the fractured area has similar microstructure to those in Chapters 3 and 4. In the microstructure in the gauge part, the α phase grains grow larger than those after the first step and become more connected. There are rarely new recrystallized grains in the microstructure, because of the long-time exposure of the material at the high temperature. There are some cavities formed in the microstructure, and the cavities tend to form inside the α phase or at the grain boundaries. In this research, it can be found that long-time annealing will lead to the early fracture of the material. In **Fig. 4.10**, it can be noticed that most of the cavities are formed inside the α phase, and the α phase portion appears to be higher. However, in **Fig. 5.11**, most of the fractures occur at the grain boundaries between α and β phase. It is known that in high-temperature deformation, the grain boundaries become weak and intergranular fracture tends to occur. However, for the unannealed Mg-Li alloy deformed by the two-step method, intragranular fracture inside the α phase tends to occur more. This means that the unannealed alloy can exhibit a better superplasticity state than the annealed alloy because the former material state can maintain the GBS mechanism without causing fracture and finally let the fracture occur inside the α phase.

The cavities are formed by the concentration of small vacancies. As the elongation gets longer, more and more cavities are formed and concentrated to become large cavities, which will cause the failure of the material. For the fracture region, the portion of the α phase is increased, which could be caused by the possible stress-

induced phase transformation, as discussed in the previous chapters. In the fracture region, intragranular fracture can be found. The final fracture is caused by the coalescence of cavities, which happens quickly, and the cavities formed at the grain boundaries may not be enough for the final fracture. Therefore, the stress-induced phase change could be caused, and the final fracture can occur inside the α phase grains.

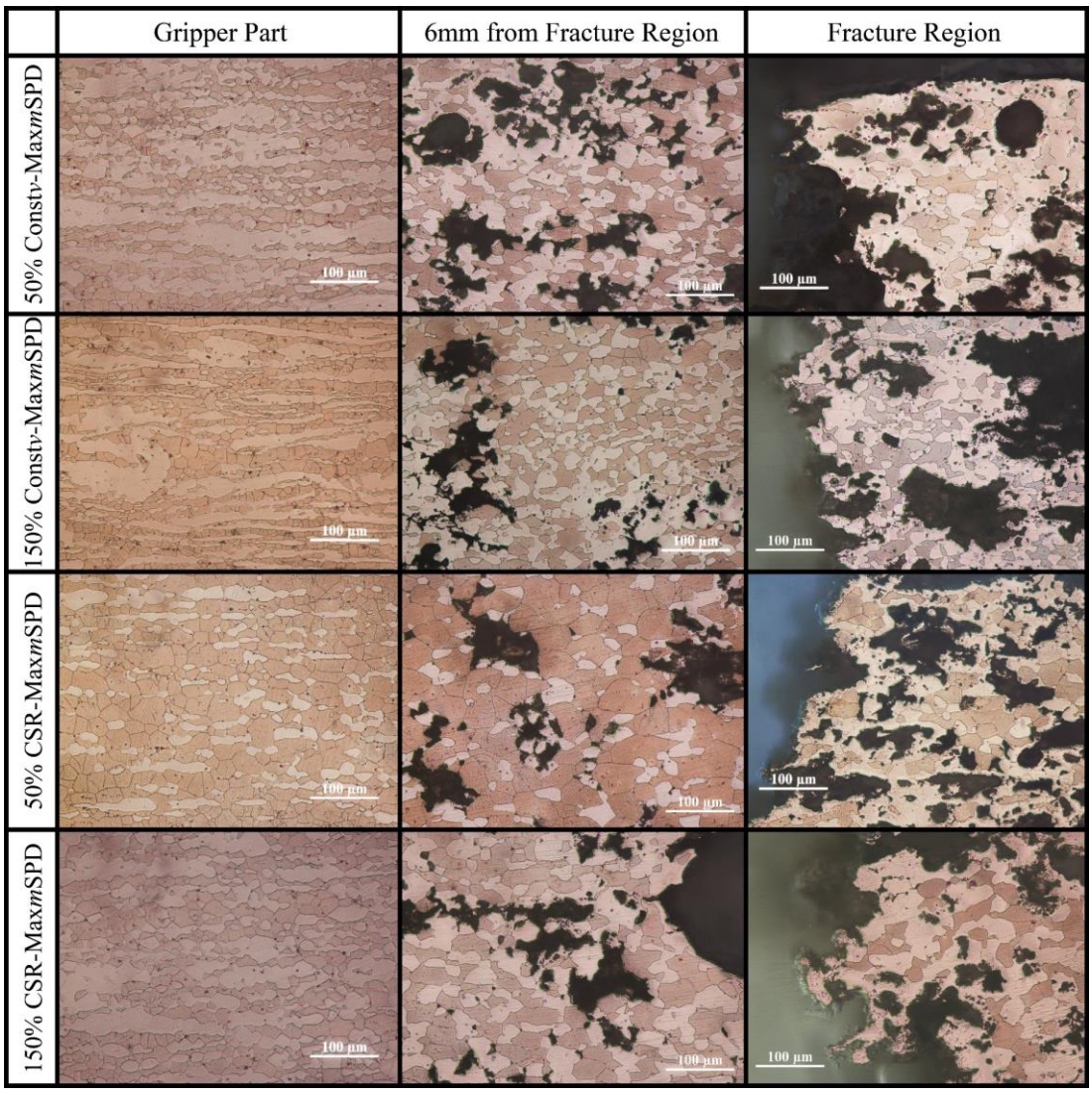

Fig. 5.11 Comparison of the microstructures in different portions of the specimens.

5.4 Conclusions

The stepped SPD method was applied to the annealed LA91 alloy to investigate the effect of annealing on the superplastic behavior of the alloy. The two-step method is the same as the method used in Chapter 4, in which the traditional methods of Const*v* and CSR SPD were adopted as the first deformation step, and the Max*m* SPD was used as the second step. A preliminary experiment was conducted to search for the optimum parameters for the SPD of the alloy by different SPD methods. The optimal parameters were then used for the two-step deformation. There are several conclusions drawn from this research, which are listed as follows.

(1) The annealing process was used to break down the strip-shaped grains produced by extrusion into smaller and more equiaxed grains by crystallization, which is more favored by Max*m* SPD. However, the annealing process can consume the strain energy induced by the extrusion process, which makes the recrystallization during the SPD process much harder and could be the reason of the early fracture of the material.

(2) The elongation by both the Const*v*-Max*m* and CSR-Max*m* SPD shows a decreasing tendency with the increase of pre-elongation. The largest elongation of 549.3 % was obtained by the Const*v*-Max*m* SPD method with 50 % pre-elongation. The decreasing trend is due to the fast decline in elongation in the second step, which may be caused by the insufficient recrystallization and overlarge grain sizes.

(3) For the annealed material, when the pre-elongation is larger than 50 %, the *m* value

in the second deformation process shows a decreasing tendency, while in Chapter 4, the unannealed alloy begins to show this tendency when the pre-elongation is larger than 150 %. This may also be caused by the depletion of strain energy and the effect of grain growth.

(4) By analysis of the microstructure, it can be found that intergranular fracture tends to occur for the annealed alloy while intragranular fracture tends to occur for the unannealed alloy. This indicates that the superplastic state of the annealed alloy is worse, and the annealed material cannot maintain the GBS without causing fracture.

Chapter 6 Conclusions and future work

6.1 Conclusions

An innovative method named maximum strain rate sensitivity superplastic deformation (Max*m* SPD) was proposed for efficiently enhancing the formability of Mg-Li alloys for forming complex structures in this thesis. This innovative method focuses on optimizing the route of the deformation process and can improve the material superplasticity through dynamically changing the deformation strain rate to maintain the maximum *m* value. This thesis is dedicated to investigating the applicability of Max*m* SPD to the deformation of Mg-9Li-1Al (LA91) alloy, as well as the deformation and fracture mechanisms of the alloy during the SPD process.

At the beginning of this research, the single-step Max*m* SPD was applied to deform the LA91 alloy whose grains had been refined by the equal channel angular extrusion (ECAE) process. The traditional deformation method of constant strain rate (CSR) SPD was also conducted for comparison. It was found that 573 K is the most suitable temperature for the SPD of the LA91 alloy. The greatest elongation of 563.7 % was obtained at the temperature of 573 K by using 8-pass ECAEed material deformed by Max*m* SPD. Meanwhile, under the same deformation conditions, the more passes of ECAE during material preparation usually corresponded to the larger *m* value and the better superplastic state throughout the deformation process. It was also discovered that Max*m* SPD is more applicable to the samples processed by the combination of

extrusion and ECAE than those only processed by extrusion, owing to the more isotropic grain structure produced by ECAE.

The two-step SPD approach was then explored for deformation of the as-extruded LA91 alloy to investigate its applicability. The intention of this method is to reduce the complex and time-consuming grain refinement procedures with the aid of the first deformation step to induce recrystallization. The largest elongation of 621.1 % was obtained by the as-extruded material deformed by CSR-Max*m* SPD with the pre-elongation of 250 %, which is even better than the best result of 563.7 % achieved in the single-step Max*m* SPD by the samples refined by ECAE. It was found that the pre-elongation step in the two-step method can gradually transform the long α phase grains into more equiaxed grains, and the optimized grain structure can lead to larger overall elongation. In terms of the first deformation step, CSR SPD generally induced greater overall elongation than constant velocity (Const*v*) SPD with the same amount of pre-elongation, possibly owing to the higher average velocity and the lower level of grain growth of CSR SPD during deformation. For the second deformation step in which Max*m* SPD was applied, when the pre-elongation was greater than 150 %, the partial elongation obtained by Max*m* SPD stopped increasing with the pre-elongation and the *m* value variation during deformation became a decreasing trend in the second step, which could be because the long α phase grains have already been fully transformed into equiaxed grains by dynamic recrystallization and the effect of grain growth becomes dominant with larger pre-elongation.

The stepped SPD method was also applied to the deformation of the annealed as-extruded LA91 alloy to invesigate the effect of annealing on the superplastic behavior of the material. The annealing process was used with the aim of breaking down the strip-shaped grains produced by extrusion into more equiaxed grains by static recrystallization, which could be favored by Max*m* SPD. However, it was found that the annealing process might consume the strain energy previously produced by the extrusion process, which could compromise dynamic recrystallization during the SPD process and cause early fracture of the material. The elongation obtained by both Constv-Max*m* and CSR-Max*m* SPD methods showed a decreasing tendency with the increase of pre-elongation. The largest overall elongation of 549.3 % was obtained by Const*v*-Max*m* SPD with 50 % pre-elongation. The decreasing trend in overall elongation with the increase of pre-elongation might be due to the fast-declining trend in the elongation of the second step, which could be caused by insufficient recrystallization and overlarge grain sizes. For the annealed alloy, when the pre-elongation was larger than 50 %, the *m* value variation in Max*m* SPD in the second step showed a decreasing tendency, while for the unannealed alloy in Chapter 4, the *m* value began to show this tendency when the pre-elongation was larger than 150 %. This phenomenon could also be caused by the depletion of strain energy and the effect of grain growth.

For the fracture mechanisms, it was found that there is an increased portion of α phase near the fracture region, which could possibly be due to stress-induced phase

transformation, and fractures mostly occurred inside the α phase or at the boundaries of the two phases. Meanwhile, for the largest overall elongation, the highest proportion of α phase and porosity level can be found in the material. In addition, for the as-received material, cavities were almost generated within the α phase, which could be caused by the easier fracture in the HCP structure of α phase. However, for the annealed alloys, intergranular fracture tended to occur, which indicates that the superplastic state of the annealed alloy might be worse, and the annealed material could not effectively maintain grain boundary sliding without generating cavities and causing fracture for a long deformation time.

6.2 Suggestions for future research

6.2.1 Further exploration of microstructure evolution

The analysis of evolution of microstructure during deformation is mainly based on the photographs taken by optical microscopy. The photos can intuitively illustrate different phases and the change in shapes and sizes of the grains in the microstructure. However, if a more detailed analysis of microstructure evolution in terms of change in textures, high-angle grain boundaries, and subgrains can be conducted, the deformation behavior and mechanisms can be better understood. Therefore, other techniques for characterizing the material microstructure should be considered and adopted.

EBSD is an ideal choice for characterizing the material microstructure, and its versatile capability can show much more information of the microstructure apart from those mentioned earlier. There have been some EBSD tests on the specimens which has shown that the CSR SPD can induce more HAGBs than the Const*v* SPD process, which is better for the dynamic recrystallization in the second process by Max*m* SPD. For further research in the future, more EBSD tests are needed to further reveal the deformation mechanism of the SPD processes.

6.2.2 Exploration of the possible stress-induced phase transformation near the fracture region

It has been noticed that in the area near fracture region of the specimens after SPD processes, the α phase appears to be connected and the α phase proportion has greatly increased, which indicates that the β phase might be transformed into α phase near the fracture region. However, it can be learnt from **Fig. 2.1** that there is no temperature-induced phase transformation at 573 K for the LA91 alloy. In addition, this phenomenon only occurs near the fracture region where cavitation becomes severe and small cavities grow quickly, which finally causes the coalescence of cavities and leads to the final fracture. In this region, the deformation strain rate is much higher than the other portion of the specimen and the deformation stress is also higher. In addition, the β phase in BCC structure which is easier to deform may be transformed into the α phase in HCP structure which is easier for fracture, and cavities and small cracks are formed inside the α phase or at the boundaries between α and β phases.

Therefore, there could be stress-induced phase transformation near the fracture region which transforms the β phase into the α phase.

In order to investigate the possible phase transformation, the EBSD technique could also be utilized to detect the change in microstructure. Meanwhile, a series of SPD experiments at different temperatures and strain rates can also be conducted to study their effect on the phase transformation.

6.2.3 Application of finite element method (FEM) in the research of Max*m* SPD process

Since the Max*m* SPD process is basically an experimental method based on the material deformation state at a certain time during the deformation process and this research is mainly focused on the applicability of the process to the Mg-Li alloy and the material deformation behavior during the process, the major work in this thesis comes from experimental endeavor. However, if the deformation process of Max*m* SPD is to be further studied, the FEM technique should be applied to simulate the deformation process, and the stress and strain distribution and potential superplastic fracture behavior can be thoroughly investigated. The data obtained from the experiments should be analyzed and processed, for the sake of construction of the constitutive models for the material deformation and fracture, and the model should be further verified and validated by conducting new experiments with other process parameters.

6.2.4 Study on how to use utilize Max*m* SPD for forming of biodegradable stent precursors

In this research, the Max*m* SPD has been applied in the superplastic tensile tests of Mg-Li alloys and it has been found that this technique can significantly enhance the formability of the alloy by maintaining the maximum *m* value and the best superplastic state throughout the deformation process. Owing to the biodegradability of Mg-Li alloys, they can be used for making biodegradable cardiovascular stents. After this research, it can be considered how to utilize the Max*m* superplasticity of Mg-Li alloys in the manufacturing process. However, the fabrication process for small hollow tubes is much different from the SPD tensile tests in terms of experimental apparatus and parameter setting, so proper experimental devices should be built, and a series of experiments need to be conducted to search for the optimal parameters for the realization of Max*m* SPD in small tube forming.

A possible way of forming the tube utilizing its superplasticity is the superplastic tube drawing by using the conventional tube drawing method, which is illustrated in **Fig. 6.1**. A hole is firstly drilled inside a cylinder specimen, which makes the cylinder into a tube with thick wall. Then, a fixed or moving mandrel is put inside the hole, and the tube as well as the mandrel is pushed through the tube drawing die. After that, the tube is clamped onto the drawing machine, and by continuous control of deformation speed, the tube wall is thinned, and the size of the tube can be reduced according to the dimensions of the tube drawing die. Hopefully, small or micro-sized stent precursors

can be fabricated by this method.

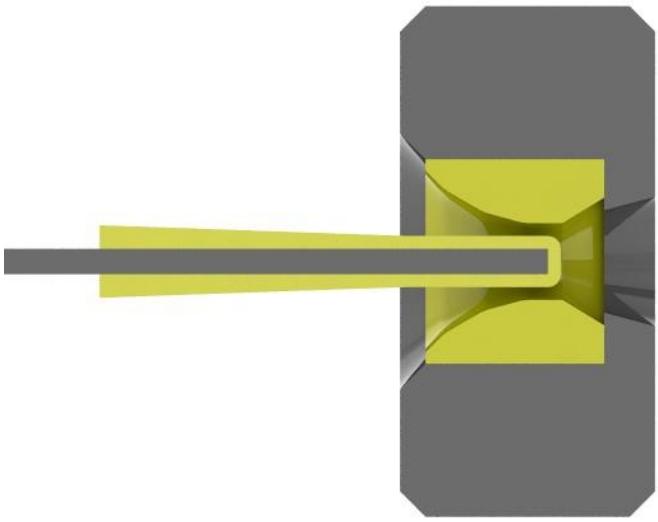

Fig. 6.1 Illustration of fabricating stent precursors by superplastic tube drawing.

Another proposed route is the superplastic dieless drawing. The core of this technique is to achieve local heating, such that a local portion of the raw material is softened and becomes able to deform, as shown in **Fig. 6.2**. There are two processing types in the dieless tube drawing: the discontinuous type and the continuous type. In the first type of deformation, one of the ends is fixed, so only a limited tube length can be produced. While in the continuous processing type, the production of the tube is by continuous feeding of raw materials, and long tube with arbitrary lengths could be produced. By using the conventional drawing process, the tools like dies, plugs and mandrels are difficult to be scaled down into microsize, and it is very hard to manufacture the microtools with high accuracy. Meanwhile, considering the hardness of installing and uninstalling the mandrel in the microtube and the friction between the mandrel and the

tool, the formability of the microtube can be limited. In this case, the technique of superplastic dieless tube drawing was initiated for the production of microtubes. The advantages and disadvantages of the die and dieless drawing are summarized in **Fig. 6.3**. This technique does not require conventional tools like mandrels and the forming efficiency can also be guaranteed [117].

In the dieless drawing system, the heating system is crucial to the forming quality of the product, and appropriate cooling systems are also required. The current heating methods are summarized in **Fig. 6.4**. For the heating sources, electric furnace heating, high frequency induction heating, direct resistance heating and laser heating are typically used [117]. Among the heating methods, induction heating is most commonly used, and local and rapid heating can be realized by the induction heating with high efficiency. In recent years, the laser heating method is also explored for the drawing process, and the small spot size of laser can be decreased easily by the design of optical systems [118-120]. From the comparison in **Fig. 6.4**, the induction heating and the laser heating methods can be the appropriate methods for manufacturing the cardiovascular stent precursors, owing to the easiness and efficiency during heating.

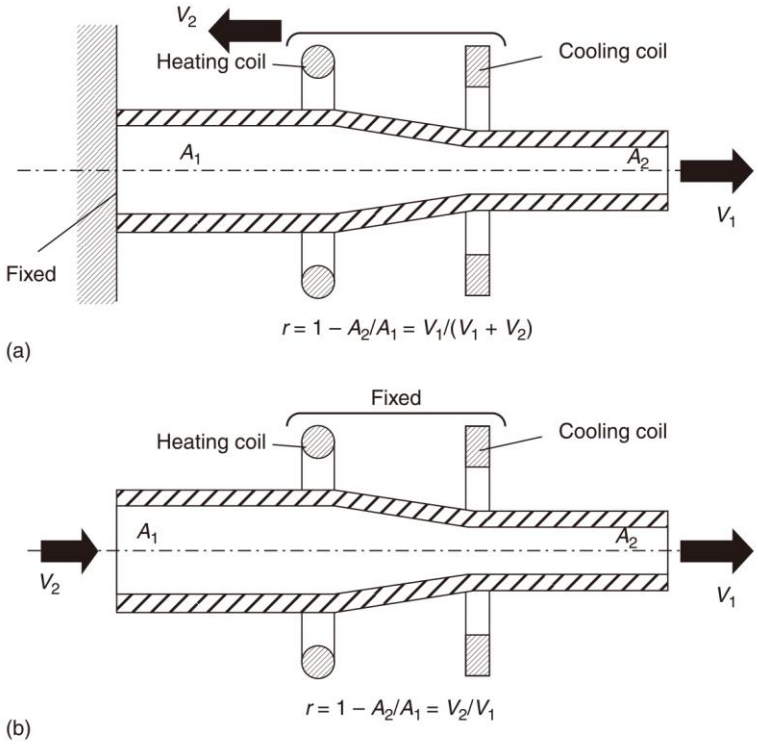

Fig. 6.2 Schematic illustration of dieless tube drawing: (a) non-continuous type and (b) continuous type [117].

	Dieless drawing	Die drawing
Outline	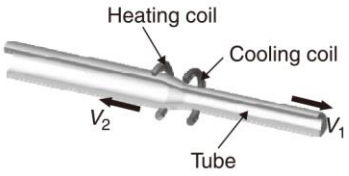	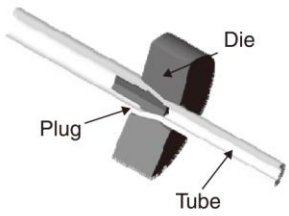
Advantage	Without tools High flexibility No friction Large reduction in area	High speed drawing High surface quality High accurate profile
Disadvantage	Free surface roughening Low drawing speed Low accurate profile Many control parameters	With tool Low flexibility With friction Low reduction in area

Fig. 6.3 Advantages and disadvantages of die and dieless drawing [117].

Heating method	Local heating	Rapid heating	Heating efficiency	Controllability
Electric furnace heating	Poor	Poor	Poor	Not good
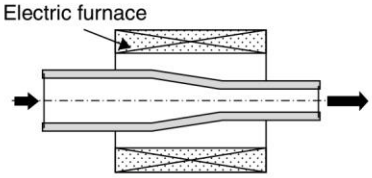				
Induction heating	Good	Good	Excellent	Good
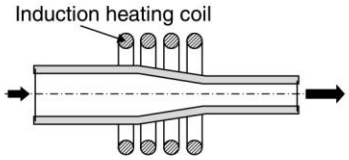				
Direct resistance heating	Bad	Excellent	Excellent	Good
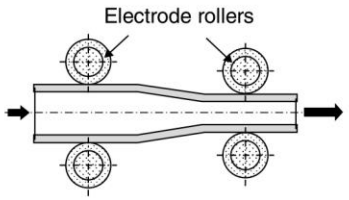				
Laser heating	Excellent	Not good	Good	Good
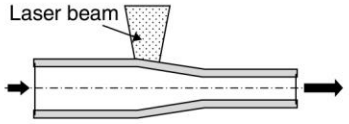				

Fig. 6.4 Different heating methods in dieless tube drawing [117].

References

[1] Y. Shao, H. Huang, T. Zhang, G. Meng, F. Wang, Corrosion protection of Mg–5Li alloy with epoxy coatings containing polyaniline, Corrosion Science 51(12) (2009) 2906-2915.

[2] T. Wang, M. Zhang, R. Wu, Microstructure and properties of Mg–8Li–1Al–1Ce alloy, Materials Letters 62(12–13) (2008) 1846-1848.

[3] J.F. Li, Z.Q. Zheng, S.C. Li, W.D. Ren, Z. Zhang, Preparation and galvanic anodizing of a Mg–Li alloy, Materials Science and Engineering: A 433(1–2) (2006) 233-240.

[4] J.R. Nebeker, R. Virmani, C.L. Bennett, J.M. Hoffman, M.H. Samore, J. Alvarez, C.J. Davidson, J.M. McKoy, D.W. Raisch, B.K. Whisenant, Hypersensitivity cases associated with drug-eluting coronary stents: a review of available cases from the Research on Adverse Drug Events and Reports (RADAR) project, Journal of the American College of Cardiology 47(1) (2006) 175-181.

[5] S.H. Hofma, W.J. van der Giessen, B.M. van Dalen, P.A. Lemos, E.P. McFadden, G. Sianos, J.M. Ligthart, D. van Essen, P.J. de Feyter, P.W. Serruys, Indication of long-term endothelial dysfunction after sirolimus-eluting stent implantation, European heart journal 27(2) (2005) 166-170.

[6] Z. Wen, C. Wu, C. Dai, F. Yang, Corrosion behaviors of Mg and its alloys with different Al contents in a modified simulated body fluid, Journal of Alloys and Compounds 488(1) (2009) 392-399.

[7] J.M. Seitz, K. Collier, E. Wulf, D. Bormann, F.W. Bach, Comparison of the corrosion behavior of coated and uncoated magnesium alloys in an in vitro corrosion environment, Advanced Engineering Materials 13(9) (2011) B313-B323.

[8] M. Kawaski, T.G. Langdon, Superplasticity in ultrafine-grained materials, Reviews on Advanced Materials Science 54 (2018) 46-55.

[9] M. Furui, C. Xu, T. Aida, M. Inoue, H. Anada, T.G. Langdon, Improving the superplastic properties of a two-phase Mg–8% Li alloy through processing by ECAP, Materials Science and Engineering: A 410–411 (2005) 439-442.

[10] Y. Yoshida, L. Cisar, S. Kamado, Y. Kojima, Low temperature superplasticity of ECAE processed Mg-10% Li-1% Zn alloy, Materials Transactions 43(10) (2002) 2419-2423.

[11] F.C. Liu, M.J. Tan, J. Liao, Z.Y. Ma, Q. Meng, K. Nakata, Microstructural evolution and superplastic behavior in friction stir processed Mg–Li–Al–Zn alloy, Journal of Materials Science 48(24) (2013) 8539-8546.

[12] S.L. Dong, T. Imai, S.W. Lim, N. Kanetake, N. Saito, I. Shigematsu, Superplasticity in Mg-Li-Zn alloys processed by high ratio extrusion, Materials and Manufacturing Processes 23(3-4) (2008) 336-341.

[13] G. Wang, M.W. Fu, Maximum m superplasticity deformation for Ti–6Al–4V titanium alloy, Journal of Materials Processing Technology 192–193 (2007) 555-560.

[14] X. Xu, G. Wang, C. Xia, Stepped superplasticity deformation-induced plastic enhancement of Ti–6Al–1.5Cr–2.5Mo–0.5Fe–0.3Si alloy, Materials & Design 36 (2012) 136-140.

[15] G.C. Wang, M.W. Fu, C.X. Cao, H.B. Dong, Study on the maximum m superplasticity deformation of Ti–6.5Al–3.5Mo–1.5Zr–0.3Si alloy, Materials Science and Engineering: A 513–514 (2009) 32-41.

[16] Q.J. Sun, G.C. Wang, M.Q. Li, Enhanced the superplasticity in Ti–6.5Al–2Zr–1Mo–1V alloy by a two-step deformation method, Materials & Design 35 (2012) 80-86.

[17] X.F. Xu, J.G. Zhang, C.F. Liu, G.C. Wang, Z.H. Yun, Superplastic behaviour and microstructural evolution in stepped tensile deformation of titanium alloy, Journal of Materials Engineering and Performance 23(1) (2014) 187-192.

[18] P.K. Bowen, E.R. Shearier, S. Zhao, R.J. Guillory, F. Zhao, J. Goldman, J.W. Drelich, Biodegradable metals for cardiovascular stents: from clinical concerns to recent zn-alloys, Advanced Healthcare Materials 5(10) (2016) 1121-1140.

[19] P.T. O'gara, F.G. Kushner, D.D. Ascheim, D.E. Casey, M.K. Chung, J.A. De Lemos, S.M. Ettinger, J.C. Fang, F.M. Fesmire, B.A. Franklin, 2013 ACCF/AHA guideline for the management of ST-elevation myocardial infarction: executive summary: a report of the American College of Cardiology Foundation/American Heart Association Task Force on Practice Guidelines, Journal of the American College of Cardiology 61(4) (2013) 485-510.

[20] W.D. Callister, D.G. Rethwisch, Materials science and engineering: an introduction, Wiley New York1991.

[21] H. Hermawan, D. Dubé, D. Mantovani, Developments in metallic biodegradable stents, Acta biomaterialia 6(5) (2010) 1693-1697.

[22] S. Saito, New horizon of bioabsorbable stent, Catheterization and Cardiovascular Interventions 66(4) (2005) 595-596.

[23] K. Hanada, K. Matsuzaki, X. Huang, Y. Chino, Fabrication of Mg alloy tubes for biodegradable stent application, Materials Science and Engineering: C 33(8) (2013) 4746-4750.

[24] R. Werkhoven, W. Sillekens, J. Van Lieshout, Processing aspects of magnesium alloy stent tube, Magnesium technology 2011, Springer 2011, pp. 419-424.

[25] K.D. Permana, A. Shuib, B. Ariwahjoedi, A review of magnesium alloys for use in biodegradable cardiovascular stents (2013).

[26] M. Peuster, P. Wohlsein, M. Brügmann, M. Ehlerding, K. Seidler, C. Fink, H. Brauer, A. Fischer, G. Hausdorf, A novel approach to temporary stenting: degradable cardiovascular stents produced from corrodible metal—results 6–18 months after implantation into New Zealand white rabbits, Heart 86(5) (2001) 563-569.

[27] A. Hartwig, Role of magnesium in genomic stability, Mutation Research/Fundamental and Molecular Mechanisms of Mutagenesis 475(1) (2001) 113-121.

[28] J. Vormann, Magnesium: nutrition and metabolism, Molecular aspects of medicine 24(1-3) (2003) 27-37.

[29] E.P. DeGarmo, J.T. Black, R.A. Kohser, B.E. Klamecki, Materials and process in manufacturing, 9th ed. ed., Prentice Hall 2003.

[30] G. Song, Recent progress in corrosion and protection of magnesium alloys, Advanced Engineering Materials 7(7) (2005) 563-586.

[31] V. Kaesel, P.T. Tai, F.W. Bach, H. Haferkamp, F. Witte, H. Windhagen, Approach to control the corrosion of magnesium by alloying, Magnesium: Proceedings of the 6th International Conference Magnesium Alloys and Their Applications, Wiley Online Library, 2003, pp. 534-539.

[32] G. Song, Control of biodegradation of biocompatable magnesium alloys, Corrosion science 49(4) (2007) 1696-1701.

[33] M. Leeflang, J. Dzwonczyk, J. Zhou, J. Duszczyk, Long-term biodegradation and associated hydrogen evolution of duplex-structured Mg–Li–Al–(RE) alloys and their mechanical properties, Materials Science and Engineering: B 176(20) (2011) 1741-1745.

[34] M. Levandowsky, L.T. Merkle, M. Cleave, Metal toxicity in mammals, JSTOR, 1979.

[35] F. Hauser, P. Landon, J. Dorn, Deformation and fracture of alpha solid solutions of lithium in magnesium. Technical Report No. 4, California. Univ., Berkeley. Minerals Research Lab., 1956.

[36] M. Zhang, F. Elkin, Magnesium–Lithium Superlight Alloys, Beijing: Science Press, 2010.

[37] W.R. Zhou, Y.F. Zheng, M.A. Leeflang, J. Zhou, Mechanical property, biocorrosion and in vitro biocompatibility evaluations of Mg–Li–(Al)–(RE) alloys for future cardiovascular stent application, Acta Biomaterialia 9(10) (2013) 8488-8498.

[38] F. Feyerabend, J. Fischer, J. Holtz, F. Witte, R. Willumeit, H. Drücker, C. Vogt, N. Hort, Evaluation of short-term effects of rare earth and other elements used in

magnesium alloys on primary cells and cell lines, Acta biomaterialia 6(5) (2010) 1834-1842.

[39] C. Yuen, W. Ip, Theoretical risk assessment of magnesium alloys as degradable biomedical implants, Acta biomaterialia 6(5) (2010) 1808-1812.

[40] N. Birbilis, M.A. Easton, A. Sudholz, S. Zhu, M. Gibson, On the corrosion of binary magnesium-rare earth alloys, Corrosion Science 51(3) (2009) 683-689.

[41] H. Baker, H. Okamoto, Alloy phase diagrams, ASM International, ASM Handbook. 3 (1992) 501.

[42] K.A. Padmanabhan, G.J. Davies, The Mechanics of superplastic deformation and the assessment of superplastic behaviour, Superplasticity, Springer1980, pp. 8-42.

[43] A. Sergueeva, A. Mukherjee, 18 - Superplastic deformation in nanocrystalline metals and alloys, in: S.H. Whang (Ed.), Nanostructured Metals and Alloys, Woodhead Publishing2011, pp. 542-593.

[44] K. Higashi, T. Ohnishi, Y. Nakatani, Superplastic behavior of commercial aluminum bronze, Scripta metallurgica 19(7) (1985) 821-823.

[45] T. Langdon, Private Communication, on the work of Y, Ma and TG Langdon, University of Southern California (1988).

[46] C.E. Pearson, The viscous properties of extruded eutectic alloys of lead-tin and bismuth-tin, J. Inst. Metals 54(1) (1934) 111-124.

[47] F.C. Liu, Z.Y. Ma, Contribution of grain boundary sliding in low-temperature superplasticity of ultrafine-grained aluminum alloys, Scripta Materialia 62(3) (2010) 125-128.

[48] Z.Y. Ma, F.C. Liu, R.S. Mishra, Superplastic deformation mechanism of an ultrafine-grained aluminum alloy produced by friction stir processing, Acta Materialia 58(14) (2010) 4693-4704.

[49] C. Xu, T.G. Langdon, Z. Horita, M. Furukawa, Using equal-channel angular pressing for the production of superplastic aluminum and magnesium alloys, Journal of materials engineering and performance 13(6) (2004) 683-690.

[50] F.C. Liu, Z.Y. Ma, Achieving exceptionally high superplasticity at high strain rates in a micrograined Al–Mg–Sc alloy produced by friction stir processing, Scripta Materialia 59(8) (2008) 882-885.

[51] F.C. Liu, Z.Y. Ma, Superplasticity governed by effective grain size and its distribution in fine-grained aluminum alloys, Materials Science and Engineering: A 530 (2011) 548-558.

[52] O.D. Sherby, J. Wadsworth, Superplasticity—Recent advances and future directions, Progress in Materials Science 33(3) (1989) 169-221.

[53] M.E. Kassner, Fundamentals of creep in metals and alloys, Butterworth-Heinemann2015.

[54] T.-G. Nieh, J. Wadsworth, O.D. Sherby, Superplasticity in metals and ceramics, Cambridge university press2005.

[55] H. Cline, Rate sensitive deformation in tin-lead alloys, Trans, AIME 239 (1967) 710-714.

[56] T. Alden, Dislocation climb theories of creep and superplasticity, Acta Metallurgica 17(12) (1969) 1435-1440.

[57] D.L. Holt, W.A. Backofen, Superplasticity in the Al-Cu eutectic alloy, ASM Trans Quart 59(4) (1966) 755-768.

[58] T. Langdon, A unified approach to grain boundary sliding in creep and superplasticity, Acta Metallurgica et Materialia 42(7) (1994) 2437-2443.

[59] R. Raj, M. Ashby, On grain boundary sliding and diffusional creep, Metallurgical transactions 2(4) (1971) 1113-1127.

[60] J. Wadsworth, A. Pelton, Superplastic behavior of a powder-source aluminum-lithium based alloy, Scripta metallurgica 18(4) (1984) 387-392.

[61] J. Wadsworth, J. Lin, O. Sherby, Superplasticity in a tool steel, Metals Technology 8(1) (1981) 190-193.

[62] M.Y. Wu, O.D. Sherby, Superplasticity in a silicon carbide whisker reinforced aluminum alloy, Scripta metallurgica 18(8) (1984) 773-776.

[63] M. Wu, J. Wadsworth, O. Sherby, Elimanation of the threshold stress for creep by thermal cycling in oxide-dispersion-strengthened materials, Scripta metallurgica 21(8) (1987) 1159-1164.

[64] M.Y. Wu, J. Wadsworth, O.D. Sherby, Internal stress superplasticity in anisotropic polycrystalline zinc and uranium, Metallurgical Transactions A 18(3) (1987) 451-462.

[65] A. Sauveur, What is steel, Trans Am Insl Min (Metall) Eng 70(3) (1924).

[66] F. Clinard, O. Sherby, Strength of iron during allotropic transformation, Acta Metallurgica 12(8) (1964) 911-919.

[67] O.A. Ruano, J. Wadsworth, O.D. Sherby, Enhanced densification of white cast iron powders by cyclic phase transformations under stress, Metallurgical Transactions

A 13(3) (1982) 355-361.

[68] A. Chokshi, T. Bieler, T. Nieh, J. Wadsworth, A. Mukherjee, Superplastieity in Aerospace (edited by HC Heikkennen and TR McNelly), AIME, Warrendale, Pa (1988) 229.

[69] Y. Maehara, T.G. Langdon, Superplasticity in ceramics, Journal of Materials Science 25(5) (1990) 2275-2286.

[70] O.D. Sherby, P.M. Burke, Mechanical behavior of crystalline solids at elevated temperature, Progress in Materials Science 13 (1968) 323-390.

[71] W.R. Cannon, O.D. Sherby, High temperature creep behavior of class I and class II solid solution alloys, Metallurgical Transactions 1(4) (1970) 1030-1032.

[72] F.A. Mohamed, T.G. Langdon, The transition from dislocation climb to viscous glide in creep of solid solution alloys, Acta Metallurgica 22(6) (1974) 779-788.

[73] D. Woodford, Strain-rate sensitivity as a measure of ductility, General Electric Co., Schenectady, NY, 1969.

[74] A. Tavassoli, S. Razavi, N. Fallah, Superplastic forming of a commercial aluminum alloy, Metallurgical Transactions A 6(3) (1975) 591.

[75] M. Garfinkle, W. Klopp, W. Witzke, Superplasticity in tungsten-rhenium alloys ,1968.

[76] M. Mabuchi, K. Higashi, The processing, properties, and applications of high-strain-rate superplastic materials, Jom 50(6) (1998) 34-39.

[77] T. Nieh, C. Henshall, J. Wadsworth, Superplasticity at high strain rates in a SiC Whisker reinforced A1 alloy, Scripta metallurgica 18(12) (1984) 1405-1408.

[78] T.G. Langdon, M. Furukawa, Z. Horita, M. Nemoto, Using intense plastic straining for high-strain-rate superplasticity, Jom 50(6) (1998) 41-45.

[79] R.S. Mishra, Processing commercial aluminum alloys for high strain rate superplasticity, JOM 53(3) (2001) 23-26.

[80] T. Nieh, J. Wadsworth, High-strain-rate superplasticity in aluminum matrix composites, Materials Science and Engineering: A 147(2) (1991) 129-142.

[81] R.D. Doherty, D.A. Hughes, F.J. Humphreys, J.J. Jonas, D.J. Jensen, M.E. Kassner, W.E. King, T.R. McNelley, H.J. McQueen, A.D. Rollett, Current issues in recrystallization: a review, Materials Science and Engineering: A 238(2) (1997) 219-274.

[82] D. Hughes, W. Nix, The absence of steady-state flow during large strain plastic deformation of some FCC metals at low and intermediate temperatures, Metallurgical Transactions A 19(12) (1988) 3013-3024.

[83] T. Sakai, J.J. Jonas, Overview no. 35 dynamic recrystallization: mechanical and microstructural considerations, Acta Metallurgica 32(2) (1984) 189-209.

[84] D. Poerschke, The Effects of forging on the microstructure and tensile properties of magnesium alloys AZ31 and ZK60, Case Western Reserve University, Cleveland, OH, USA (2009).

[85] Z. Yang, J. Li, J. Zhang, G. Lorimer, J. Robson, Review on research and development of magnesium alloys, Acta Metallurgica Sinica 5(21) (2008) 313-328.

[86] J. Koike, R. Ohyama, T. Kobayashi, M. Suzuki, K. Maruyama, Grain-boundary sliding in AZ31 magnesium alloys at room temperature to 523 K, Materials

Transactions 44(4) (2003) 445-451.

[87] J. Koike, T. Kobayashi, T. Mukai, H. Watanabe, M. Suzuki, K. Maruyama, K. Higashi, The activity of non-basal slip systems and dynamic recovery at room temperature in fine-grained AZ31B magnesium alloys, Acta materialia 51(7) (2003) 2055-2065.

[88] J. Koike, Dislocation plasticity and complementary deformation mechanisms in polycrystalline Mg alloys, Materials Science Forum, Trans Tech Publ, 2004, pp. 665-668.

[89] C.Y. Wang, K. Wu, M.Y. Zheng, Compressive deformation of ZK60 magnesium alloy at elevated temperature, Key Engineering Materials, Trans Tech Publ, 2007, pp. 631-634.

[90] F.A. Mohamed, Micrograin superplasticity: characteristics and utilization, Materials 4(7) (2011) 1194-1223.

[91] X. Liu, G. Du, R. Wu, Z. Niu, M. Zhang, Deformation and microstructure evolution of a high strain rate superplastic Mg–Li–Zn alloy, Journal of Alloys and Compounds 509(39) (2011) 9558-9561.

[92] K. Lin, Z. Kang, Q. Fang, J. Zhang, Superplasticity at Elevated Temperature of a Coarse-Grained Mg–Li Alloy, Advanced Engineering Materials 16(4) (2014) 381-388.

[93] M. Mabuchi, K. Ameyama, H. Iwasaki, K. Higashi, Low temperature superplasticity of AZ91 magnesium alloy with non-equilibrium grain boundaries, Acta Materialia 47(7) (1999) 2047-2057.

[94] R. Valiev, I. Alexandrov, Y. Zhu, T. Lowe, Paradox of strength and ductility in

metals processed by severe plastic deformation, Journal of Materials Research 17(1) (2002) 5-8.

[95] O. Sivakesavam, Y. Prasad, Characteristics of superplasticity domain in the processing map for hot working of as-cast Mg–11.5 Li–1.5 Al alloy, Materials Science and Engineering: A 323(1-2) (2002) 270-277.

[96] F. Cao, H. Ding, Y. Li, G. Zhou, Superplasticity, microstructural evolution and deformation mechanism of super-light two-phase Mg–Li alloys, Chin. J. Nonferrous Met 19 (2009) 1908-1916.

[97] W. Backofen, Superplasticity in an Al-Zn alloy, Trans. ASM 57 (1964) 980-990.

[98] S. Dahlgren, Superplasticity of unalloyed beta plutonium, Battelle Memorial Inst., Richland, Wash., 1968.

[99] D. Lee, W. Backofen, Superplasticity in some titanium and zirconium alloys, Massachusetts Inst. of Tech., Cambridge, 1967.

[100] W. Morrison, Superplasticity of low-alloy steels, ASM Trans Quart 61(3) (1968) 423-434.

[101] W.F. Hosford, Mechanical behavior of materials, Cambridge University Press2010.

[102] P. Feltham, Stress relaxation in copper and alpha-brasses at low temperatures, J Inst Met 89 (1960) 210-214.

[103] F. Guiu, P. Pratt, Stress relaxation and the plastic deformation of solids, physica status solidi (b) 6(1) (1964) 111-120.

[104] J.W. Edington, K. Melton, C. Cutler, Superplasticity, Progress in materials

science 21(1-2) (1976) 61-170.

[105] J. Hedworth, M. Stowell, The measurement of strain-rate sensitivity in superplastic alloys, Journal of Materials Science 6(8) (1971) 1061-1069.

[106] M.W. Fu, Y.W. Tham, H.H. Hng, K.B. Lim, The grain refinement of Al-6061 via ECAE processing: deformation behavior, microstructure and property, Materials Science and Engineering: A 526(1–2) (2009) 84-92.

[107] Y.W. Tham, M.W. Fu, H.H. Hng, M.S. Yong, K.B. Lim, Study of deformation homogeneity in the multi-pass equal channel angular extrusion process, Journal of Materials Processing Technology 192–193 (2007) 121-127.

[108] Y.W. Tham, M.W. Fu, H.H. Hng, M.S. Yong, K.B. Lim, Bulk nanostructured processing of aluminum alloy, Journal of Materials Processing Technology 192–193 (2007) 575-581.

[109] M. Furukawa, Y. Iwahashi, Z. Horita, M. Nemoto, T.G. Langdon, The shearing characteristics associated with equal-channel angular pressing, Materials Science and Engineering: A 257(2) (1998) 328-332.

[110] Y.W. Tham, M.W. Fu, H.H. Hng, Q.X. Pei, K.B. Lim, Microstructure and properties of Al-6061 alloy by equal channel angular extrusion for 16 passes, Materials & Manufacturing Processes 22(7/8) (2007) 819-824.

[111] K. Matsubara, Y. Miyahara, Z. Horita, T.G. Langdon, Developing superplasticity in a magnesium alloy through a combination of extrusion and ECAP, Acta Materialia 51(11) (2003) 3073-3084.

[112] X. Liu, R. Wu, Z. Niu, J. Zhang, M. Zhang, Superplasticity at elevated

temperature of an Mg–8%Li–2%Zn alloy, Journal of Alloys and Compounds 541 (2012) 372-375.

[113] R.D. Doherty, Primary Recrystallization, R.W. Cahn, M.C. Flemings, B. Ilschner, E.J. Kramer, S. Mahajan, P. Veyssière (Eds.), Encyclopedia of materials: science and technology (Second edition), Elsevier, Oxford, 2001, pp. 7847-7850.

[114] DeGarmo, E. Paul, J. Temple Black, R. A Kohser, Materiales and processes in manufacturing, 2018.

[115] F.C. Liu, M.J. Tan, J. Liao, Z.Y. Ma, Q. Meng, K. Nakata, Microstructural evolution and superplastic behavior in friction stir processed Mg-Li-Al-Zn alloy, Journal of Materials Science 48(24) (2013) 8539-8546.

[116] R.C. Gifkins, Grain-boundary sliding and its accommodation during creep and superplasticity, Metallurgical Transactions A 7(8) (1976) 1225-1232.

[117] G. Giuliano, Superplastic forming of advanced metallic materials: methods and applications, Elsevier 2011.

[118] Y. Li, N.R. Quick, A. Kar, Dieless laser drawing of fine metal wires, Journal of materials processing technology 123(3) (2002) 451-458.

[119] Y. Li, N.R. Quick, A. Kar, Thermomechanical effects in laser microprocessing for dieless metal wire drawing, Journal of Laser Applications 14(2) (2002) 91-99.

[120] Y. Li, N.R. Quick, A. Kar, Structural evolution and drawability in laser dieless drawing of fine nickel wires, Materials Science and Engineering: A 358(1-2) (2003) 59-70.